

Dissertation
submitted to the
Combined Faculty of Natural Sciences and Mathematics
of the Ruperto Carola University Heidelberg, Germany
for the degree of
Doctor of Natural Sciences

Presented by

Annica Flemming, M.Sc.
born in Düsseldorf, Germany

Oral examination: March 15th, 2019

Investigating Dynamics of HIV-1 Protease Activity during the Viral Assembly Process

Referees: Prof. Dr. Hans-Georg Kräusslich

PD Dr. Jacomine Krijnse Locker

Eidesstattliche Erklärung

Hiermit erkläre ich, Annica Flemming, Maaßstr. 21, 69123 Heidelberg, geboren am 03.11.1988 in Düsseldorf, dass ich die vorliegende Dissertation am Lehrstuhl für Virologie an der Ruprecht-Karls-Universität Heidelberg unter Anleitung von Prof. Dr. Barbara Müller selbständig verfasst habe und nur mit den angegebenen Hilfsmitteln angefertigt habe und das alle Stellen, die dem Wortlaut oder dem Sinne nach anderen Werken entnommen sind, durch Angabe der Quellen als Entlehnung kenntlich gemacht worden sind. Ich habe an keiner anderen Stelle ein Prüfungsverfahren beantragt bzw. die Dissertation in dieser oder anderer Form bereits anderweitig als Prüfungsarbeit verwendet oder einer anderen Fakultät als Dissertation vorgelegt. Ich erkläre hiermit, dass die Dissertation unter Verwendung elektronischer Datenverarbeitungsprogramme auf die Einhaltung allgemein geltender wissenschaftlicher Standards überprüft werden darf.

Heidelberg, den 16.01.2019

1 Summary

Human immunodeficiency virus (HIV-1) particles assemble and bud at the host cell plasma membrane and are released as immature, noninfectious particles. Concomitant with release, the viral protease (PR) cleaves Gag and GagProPol polyproteins into single proteins, leading to a major structural rearrangement of the virion. Temporal control of proteolytic cleavage with respect to particle assembly appears crucial for the maturation of infectious particles. The order of Gag processing is tightly regulated by utilization of different proteolytic cleavage sites with specific binding affinities to HIV-1 PR. However, the precise mechanism and kinetics of PR activation, as well as the time course of proteolytic maturation are currently unclear.

Since many virus particles are formed in an infected cell and the time course of formation is asynchronous – not only between individual cells but also on the surface of a single cell - bulk biochemical analyses are not suitable for analysis of PR activation. Therefore, the aim of my thesis was to monitor and quantitate the HIV-1 PR activity during virus particle assembly by live-cell microscopy. Live-cell analysis of HIV-1 assembly site formation using fluorescence microscopy was already established in the lab. Previous studies from our and other groups, imaging fluorescently labeled virus assembly by total internal fluorescence microscopy (TIRF), showed that formation of viral assembly sites proceeds over 1-2 h, and Gag assembly for an individual bud is completed within 10-20 min. Here, I designed and explored various approaches for single virus tracking of PR activity in parallel to Gag assembly. For this purpose, I developed and tested different sensors to detect (i) PR enzymatic activity at the nascent assembly site, (ii) Gag polyprotein processing mediated by PR, or (iii) the generation of mature HIV-1 PR by autoprocessing from the GagProPol precursor.

To measure PR activity at the assembly site, I designed Förster resonance energy transfer (FRET) reporter molecules which were targeted to nascent assemblies. For this, a FRET pair of autofluorescent proteins was linked via a Gag-derived PR cleavage site and fused to the viral protein r (Vpr) to mediate incorporation into particles. We could show the incorporation, and proteolytic processing of the FRET-based sensor was observed. The PR-dependent changes in FRET signal were analyzed in purified virus-like particles (VLPs) and viral assembly sites at the plasma membrane of HeLa Kyoto cells. While sensor co-expression with wild-type HIV-1 PR caused a decrease of the FRET values by two-fold upon proteolytic processing, during time-lapse measurements of the assembly process we could not detect a change in FRET signal over time.

In order to detect Gag cleavage as readout for HIV-1 PR activity, I attempted different approaches. Initially, I applied a previously established system for distinguishing immature and mature particles by STED nanoscopy to the analysis of particles formed at the cell surface in live-cell experiments. While STED nanoscopy is unsuitable for following assembly and maturation by live cell imaging, I could show that Gag processing and particle arrangement did occur under conditions and in the time frame of intended measurements.

I then tested two approaches for live-cell measurements of Gag processing. A first attempt to utilize a split fluorescent protein-based method was not successful, since fluorescence was found to be independent of the Gag processing state. This approach was therefore abandoned.

In an alternative approach, I explored the use of changes in eCFP fluorescence lifetime depending on fluorophore concentration via homo FRET. For this, eCFP molecules were inserted within the Gag polyprotein. Local Gag concentrations increase during the assembly process and should thus lead to a decrease of fluorescence lifetime. Proteolytic processing should release the fluorophore for free diffusion within the virus particle and thereby cause an increase in fluorescence lifetime. Indeed, Gag.eCFP cleavage by HIV-1 PR resulted in changes in fluorescence lifetime measured in purified VLPs and at the plasma membrane of HeLa Kyoto cells. Time-lapse experiments visualized differences in fluorescent lifetime during viral assembly. So far, only few events that may correspond to proteolytic processing were detected. Further adaptation of the system to live cell measurements is under way.

Finally, I studied the formation of active HIV-1 PR during assembly using an innovative approach based on the binding of a fluorogenic inhibitor. Various sensors, designed to fluoresce upon binding to the PR active site, were provided by our collaboration partners who coupled the fluorogenic dye silicone-rhodamine (SiR) to the PR inhibitor Ritonavir (RTV). Specific signal increase upon binding to active PR was shown *in vitro* and on assembly sites at the plasma membrane of HeLa Kyoto cells. The sensor SiR-C6-RTV was identified to feature the highest signal-to-noise ratio and best allowed the detection of active HIV-1 PR during viral assembly.

Using this compound, I successfully established conditions for time-resolved detection of mature PR at nascent assembly sites. Different SiR recruitment patterns with respect to progression of Gag assembly were observed. Early signal increase was detected after 10-20 min, suggesting PR activation at late stages of assembly. Later events were observed after ~ 40 min, suggesting formation of active PR after viral release. Further improvement of signal-to-noise ratio would be beneficial and is currently under way. An extensive analysis of the frequency of the different phenotypes, also in conjunction with recruitment of the cellular protein Vps4 recruited shortly before HIV-1 release, will yield insight into the sequence of events at nascent assembly sites in following studies.

2 Zusammenfassung

An der Plasmamembran der Wirtszelle gebildete Partikel des menschlichen Immunschwäche-Virus (HIV-1) schnüren sich von der dieser ab und werden als unreife, nicht infektiöse Partikel freigesetzt. Gleichzeitig spaltet die virale Protease (PR) Gag und GagProPol-Polyproteine in einzelne Proteine, was zu einer größeren strukturellen Neuordnung des Virion führt. Die zeitliche Kontrolle der proteolytischen Spaltung in Bezug auf die Partikelbildung ist entscheidend für die Reifung infektiöser Partikel. Die Reihenfolge der Gag Prozessierung wird durch die Nutzung verschiedener proteolytischer Schnittstellen mit spezifischen Bindungsaffinitäten zu HIV-1 PR präzise geordnet. Allerdings sind der genaue Mechanismus und die Kinetik der PR-Aktivierung sowie der zeitliche Verlauf der proteolytischen Reifung derzeit unklar.

Da viele Viruspartikel in einer infizierten Zelle gebildet werden und der zeitliche Verlauf der Bildung – nicht nur zwischen mehreren Zellen, sondern auch auf der Oberfläche einer einzelnen Zelle – asynchron ist, sind biochemische Analysen nicht für die Untersuchung der PR-Aktivierung geeignet. Daher war das Ziel meiner Arbeit, die HIV-1 PR-Aktivität während der Viruspartikelentstehung mittels Lebendzellmikroskopie zu überwachen und zu quantifizieren. Die Lebendzellanalyse der HIV-1 Partikel-Assemblierung mittels Fluoreszenzmikroskopie wurde zuvor bereits im Labor etabliert. Frühere Studien aus unseren und anderen Gruppen, die fluoreszenzmarkierte Virusentstehung mittels Total Internal Fluorescence Microscopy (TIRF) anschauten, haben gezeigt, dass die Bildung von Viruspartikeln an einer Zelle über 1-2 Stunden andauert und die Gag Assemblierung für ein einzelnes Partikel innerhalb von 10-20 Minuten abgeschlossen ist. Hier habe ich verschiedene Ansätze zur Verfolgung von PR-Aktivitäten in einzelnen Viruspartikeln parallel zu deren Gag-Assembly entworfen und evaluiert. Zu diesem Zweck habe ich verschiedene Sensoren entwickelt und getestet, um alternativ (i) PR-enzymatische Aktivität an der Virusbildungsstelle, (ii) Gag-Polyproteinprozessierung, die durch PR vermittelt wird, oder (iii) die Erzeugung von reifer HIV-1 PR durch Autoprocessing aus dem GagProPol-Polyprotein nachzuweisen.

Um die PR-Aktivität an der Bildungsstelle zu messen, entwarf ich Förster Resonanz Elektronen Transfer (FRET) Reportermoleküle, die zur Assemblierungsstelle rekrutiert werden. Dazu wurde ein FRET-Paar autofluoreszierender Proteine über eine von Gag abgeleitete PR-Spaltstelle verknüpft und mit dem viralen Protein r (Vpr) fusioniert, um die Aufnahme in Partikel zu vermitteln. Ich konnte die Aufnahme in Viruspartikel zeigen und die proteolytische Prozessierung des FRET-basierten Sensors beobachten. Die PR-abhängigen Veränderungen im FRET-Signal wurden in aufgereinigten virusähnlichen Partikeln (VLPs) und viralen Assemblierungsstellen an der Plasmamembran von HeLa Kyoto-Zellen analysiert. Während die Sensor Koexpression mit Wildtyp-HIV-1 PR bei der proteolytischen Spaltung zu einer Halbierung der FRET-Werte führte, konnten wir während der Zeitraffer-Messungen des Assemblierungsprozesses keine Veränderung des FRET-Signals über die Zeit feststellen.

Um die Gag Prozessierung als Anzeige für die HIV-1 PR-Aktivität zu erkennen, habe ich verschiedene Ansätze untersucht. Zunächst habe ich ein zuvor etabliertes System zur Unterscheidung von unreifen und reifen Partikeln mittels STED-Nanoskopie auf die Analyse von Partikeln angewendet, die an der Zelloberfläche in Lebendzell-Experimenten gebildet wurden. Während die STED-Nanoskopie derzeit für die Verfolgung von Partikelbildung und Reifung durch Lebendzell-Mikroskopie ungeeignet ist, konnte ich zeigen, dass die Gag

Prozessierung und Partikelumstrukturierung unter Bedingungen und im Zeitrahmen der geplanten Messungen erfolgte.

Im Anschluss habe ich zwei Ansätze für Lebendzell-Messungen der Gag Prozessierung getestet. Ein erster Versuch, eine auf Split-Fluoreszenzprotein basierende Methode zu verwenden, war nicht erfolgreich, da sich die Fluoreszenz als unabhängig vom Gag Prozessierungszustand erwies. Dieser Ansatz wurde daher verworfen.

In einem alternativen Ansatz untersuchte ich die Verwendung von Änderungen der eCFP-Fluoreszenzlebensdauer in Abhängigkeit von der Fluorophor-Konzentration über homo FRET. Dazu wurden eCFP-Moleküle in das Gag-Polyprotein eingebracht. Die lokalen Gag-Konzentrationen steigen während des Partikelbildungsprozesses und sollten daher zu einer Verkürzung der Fluoreszenzlebensdauer führen. Bei der proteolytischen Prozessierung sollte der Fluorophor zur freien Diffusion innerhalb des Viruspartikel freigesetzt werden, was zu einer Erhöhung der Fluoreszenzlebensdauer führen würde. Tatsächlich führte die Gag.eCFP-Spaltung durch HIV-1 PR zu Veränderungen in der Fluoreszenzlebensdauer, die in gereinigten VLPs und an der Plasmamembran von HeLa Kyoto-Zellen gemessen wurden. In Zeitraffer-Experimenten wurden Unterschiede in der Fluoreszenzlebensdauer während der Virusbildung visualisiert. Bisher wurden nur wenige Ereignisse erkannt, die der proteolytischen Prozessierung entsprechen können. Eine weitere Anpassung des Systems an die Messungen in lebenden Zellen ist in Arbeit.

Schließlich untersuchte ich die Bildung von aktiver HIV-1 PR während der Partikelbildung mit einem innovativen Ansatz, der auf der Bindung eines fluorogenen Inhibitors basiert. Verschiedene Sensoren, die bei der Bindung an die PR-aktive Stelle fluoreszieren, wurden von unseren Kooperationspartnern zur Verfügung gestellt, die den fluorogenen Farbstoff Silikon-Rhodamin (SiR) mit dem PR-Inhibitor Ritonavir (RTV) gekoppelt haben. Spezifische Signalzunahme bei Bindung an aktive PR wurde *in vitro* und an Assemblierungsstellen an der Plasmamembran von HeLa Kyoto Zellen gezeigt. Der Sensor SiR-C6-RTV wurde mit dem höchsten Signal-Rausch-Verhältnis identifiziert und ermöglichte den Nachweis von aktiver HIV-1 PR während der Virusbildung.

Mit dieser Verbindung habe ich erfolgreich Bedingungen für den zeitaufgelösten Nachweis von reifer PR an im Entstehen begriffenen Assemblierungsstellen geschaffen. Unterschiedliche SiR-Rekrutierungsmuster in Bezug auf das Fortschreiten der Partikelbildung wurden beobachtet. Ein früher Signalanstieg wurde nach 10-20 min erkannt, was auf eine PR-Aktivierung in den späten Phasen der Assemblierung hindeutet. Spätere Ereignisse wurden nach ~ 40 min beobachtet, was auf die Bildung einer aktiven PR nach der Virusfreisetzung hindeutet. Eine weitere Verbesserung des Signal-Rausch-Verhältnisses wäre von Vorteil und wird derzeit durchgeführt. Eine umfangreiche Analyse der Häufigkeit der verschiedenen Phänotypen, auch in Verbindung mit der Rekrutierung des kurz vor der HIV-1-Freisetzung rekrutierten zellulären Proteins Vps4, wird in künftigen Studien einen Einblick in die Abfolge der Ereignisse an entstehenden Partikelbildungsstellen geben.

3 Table of contents

1	Summary	1
2	Zusammenfassung	3
3	Table of contents	5
4	Introduction	9
4.1	Human Immunodeficiency Virus Type 1 (HIV-1).....	9
4.1.1	Classification, genome and morphology	10
4.1.2	Replication-cycle of HIV-1	12
4.1.2.1	Assembly, budding and maturation	13
4.1.3	HIV-1 protease – Key factor of maturation.....	15
4.1.3.1	PR structure and function	15
4.1.3.2	Mechanism of PR function	17
4.1.3.3	PR inhibitors.....	20
4.2	Fluorescence labeling of virus-like particles.....	22
4.2.1	Fluorescence tags inserted in Gag	22
4.2.2	Fluorescence tags inserted by coupling to Vpr	22
4.3	Fluorescence-based methods applied in this study	23
4.3.1	Bimolecular fluorescence complementation assays detect Gag processing	23
4.3.2	Förster resonance energy transfer to detect proteolytic activity	23
4.3.3	Fluorescence lifetime-resolved imaging to detect Gag processing	24
4.3.4	Fluorogenic probes to stain active PR	24
4.3.5	Single virus tracking at assembly sites	25
4.4	Aim of the work	26
5	Materials and Methods	27
5.1	Materials	27
5.1.1	Laboratory Equipment.....	27
5.1.2	Reagents.....	29
5.1.2.1	Chemicals and consumables.....	29
5.1.2.2	Protease Inhibitors	31
5.1.2.3	Reagent Systems (Kits).....	34
5.1.2.4	Buffers and Solutions	34
5.1.2.5	Growth Media.....	35
5.1.2.6	Nucleic acids.....	36
5.1.2.7	Plasmid DNA.....	36
5.1.2.8	Enzymes	37

5.1.2.9	Antibodies and dyes.....	38
5.1.3	Software.....	38
5.2	Methods.....	39
5.2.1	Biochemical methods.....	39
5.2.1.1	SDS-Polyacrylamide Gel Electrophoresis (SDS-PAGE) and Western Blotting.....	39
5.2.1.2	Spectrofluorometry.....	40
5.2.2	Cell biological methods.....	40
5.2.2.1	Cell culture.....	40
5.2.2.2	SNAP and Clip stain.....	41
5.2.2.3	Staining of cells with fluorogenic PR inhibitor.....	41
5.2.2.4	Flow cytometry.....	41
5.2.3	Molecular biological methods.....	42
5.2.3.1	Bacterial transformation and plasmid amplification.....	42
5.2.3.2	Preparation of plasmid DNA from bacterial mini cultures.....	42
5.2.3.3	Gene amplification by polymerase chain reaction (PCR).....	43
5.2.3.4	Agarose gelelectrophoresis.....	43
5.2.3.5	DNA digest and ligation.....	43
5.2.4	Cloning procedures.....	44
5.2.4.1	Cloning by PCR.....	44
5.2.4.2	Subcloning.....	44
5.2.5	Virological methods.....	46
5.2.5.1	Preparation of virus-like particles (VLPs).....	46
5.2.5.2	SNAP labeling of VLPs.....	46
5.2.6	Imaging methods.....	46
5.2.6.1	Total internal reflective fluorescence microscopy (TIRF).....	46
5.2.6.2	Laser scanning confocal microscopy.....	47
5.2.6.3	Stimulated emission depletion (STED).....	47
5.2.6.4	Fluorescence lifetime imaging microscopy (FLIM).....	47
5.2.7	Image analysis.....	48
5.2.7.1	Image processing.....	48
5.2.7.2	FRET analysis.....	48
5.2.7.3	Acceptor bleaching.....	48
5.2.7.4	FRAP analysis.....	48
5.2.7.5	Co-localization analysis.....	48
5.2.7.6	Single assembly sites kinetics (Tracking via Imaris).....	49
5.2.8	Statistical analysis.....	49

6	Results	50
6.1	Fluorescence-tagged virus-like particles can be visualized in fluorescence microscopy	50
6.2	Live-cell imaging of the viral assembly process	52
6.3	Design of sensors to detect HIV-1 PR activity during viral assembly	56
6.3.1	An external FRET-based sensor was specifically cleaved by HIV-1 PR	56
6.3.2	Internal labeling of Gag for detection of Gag processing as a marker for PR activity	69
6.3.2.1	Split fluorescent proteins and insertion in Gag does not enable distinction of mature and immature VLPs	69
6.3.2.2	Changes in localization of fluorescence tags in Gag can be visualized by STED microscopy	71
6.3.2.3	Changes in fluorescence lifetime of eCFP in Gag can be visualized by FLIM microscopy	75
6.3.3	Design of fluorogenic HIV-1 PR inhibitors to specifically visualize the active PR	82
6.3.3.1	Specific fluorogenicity of the probes was validated by spectrophotometry	84
6.3.3.2	Specific fluorogenicity of the probes detected at HIV-1 assembly sites in HeLa Kyoto cells	89
7	Discussion	95
7.1	Visualization of the assembly process by fluorescence microscopy	95
7.2	Design of sensors to visualize HIV-1 PR activity during viral assembly by fluorescence microscopy	96
7.2.1	An external FRET-based sensor was specifically cleaved by HIV-1 PR	96
7.2.2	Internal labeling of Gag for detection of Gag processing as a marker for PR activity	98
7.2.2.1	Split fluorescent proteins and insertion in Gag does not enable distinction of mature and immature VLPs	98
7.2.2.2	Changes in localization of fluorescence tags in Gag can be visualized by STED microscopy	99
7.2.2.3	Changes in fluorescence lifetime of eCFP in Gag can be visualized by FLIM microscopy	100
7.2.3	Formation of active HIV-1 PR was detected during the viral assembly process	101
7.3	Future implications of the project	103
8	Abbreviations	104
9	Index	107
10	Publications and contributions	109
10.1	Publications	109
10.2	Conference contributions	109

10.3 Contributions to this project.....	109
11 Acknowledgements.....	111
12 Plasmid Maps	113
13 References.....	116

4 Introduction

4.1 Human Immunodeficiency Virus Type 1 (HIV-1)

The human immunodeficiency virus (HIV) is the main causative agent for the immune disease acquired immune deficiency syndrome (AIDS). In 2017, globally 36.9 million people were infected with HIV and about 1 million people died of AIDS (UNAIDS Global AIDS, 2018). The disease was already described in 1981, but HIV-1 was first isolated in 1983 (Gottlieb et al. 1981; Barré-Sinoussi et al. 1983; Popovic et al. 1984).

The course of an HIV infection can be divided in 3 phases: Acute phase, asymptomatic phase and symptomatic phase (Pantaleo et al. 1993; Pantaleo und Fauci 1995). The acute phase is characterized by high viral titers, reported symptoms in this time are described as flu-like and summarized as mononucleosis-like symptoms. A few days after infection, activated lymphocytes produce virus in high quantities (Flint 2015). The high viremia is suppressed within a few weeks after infection due to the depletion of the susceptible T cell population and to the establishment of a cell-mediated immune response that is observed prior to antibody production. The inflammatory response during acute infection stimulates CD4⁺ T cell maturation, therefore the CD4⁺ T cell population partly recovers.

After 3 to 4 months viremia declines, in some cases even under the detection level, while viral replication continues. Due to the continuous infection, immune activation and cytotoxicity of the virus, the CD4⁺ T cell population decreases over time. The term “clinical latency” describes a lack of symptoms, while there is still viral production and therefore no complete state of latency (Pantaleo und Fauci 1995).

There is a steady but slow disease progression until the CD4⁺ T cell count drops and the deterioration of the immune system results in the inability to fight opportunistic infections e.g. atypical pneumonia. This state is called acquired immunodeficiency syndrome (AIDS) (Flint 2015).

The first drug to treat HIV infection was approved in 1987. AZT was found to impair viral replication by inhibiting reverse transcription (Nakashima et al. 1986). Quickly, the virus developed resistance to the drug and the necessity to target multiple viral processes simultaneously was revealed.

The virus encoded HIV-1 protease (PR) is known to be crucial for formation of infectious viral particles. Design of specific inhibitors of this enzyme enabled combination antiretroviral therapy for the first time in 1996, which decreased the potential of drug resistance significantly (James 1995).

In 2017, 1.8 million people became infected with HIV-1 and 21.7 million people accessed antiretroviral therapy (UNAIDS Global, 2018). The numbers of new infections are decreasing over the years, while the fractions of infected patients treated with combined antiretroviral therapy (cART) increases. cART involves at least three drugs, targeting multiple steps of the viral replication cycle, that reduces the viral load below the detection limit and enables a relatively normal life today (DAH, n=n, 2018).

4.1.1 Classification, genome and morphology

HIV-1 and HIV-2 are members of the genus *Lentiviridae* and belong to the family *Retroviridae*. HIV-2 was isolated from patients in West Africa, but due to its higher clinical relevance, this study only focuses on HIV-1 (Sharp und Hahn 2011).

HIV-1 is divided in three groups that vary in their prevalence. Each arose from independent zoonotic transmission from non-human primates infected with simian immunodeficiency virus (SIV) to humans in Central and West Africa (Gao und Karin 2005; Plantier et al. 2009). Group M (“major”) is responsible for 98% of HIV-1 infections and geographically most spread (Sharp und Hahn 2010). Groups O (“outliers”) and N (“non-O, non-M”) are relatively rare and restricted to the area of Cameroon and surrounding countries in central Africa (Sharp et al. 1999).

HIV-1 is a membrane enveloped virus that integrates its genome in the host cell. The spherical virus particle has a diameter of ~145 nm (Briggs et al. 2009) and carries two copies of the ss(+)RNA genome with a size of 9.7 kilobases (Flint 2015; Coffin 1997; Briggs et al. 2003). While HIV-1 displays a high sequence variability, the genomic organization is strongly conserved. The coding regions are flanked by long terminal repeats (LTRs) at both the 5’ and 3’ end of the genome. Nine open reading frames (ORFs) are divided in three different classes of encoded proteins: structural proteins Gag (group specific antigen), Pol (polymerase) and Env (envelope protein), regulatory proteins Tat (transactivator of transcription) and Rev (regulator of virion), and accessory proteins Vif (virion infectivity factor), Vpr (viral protein R), Vpu (viral protein U) and Nef (negative factor) (Fig. 1) (Coffin 1997; Flint 2015; Kirchhoff 2009).

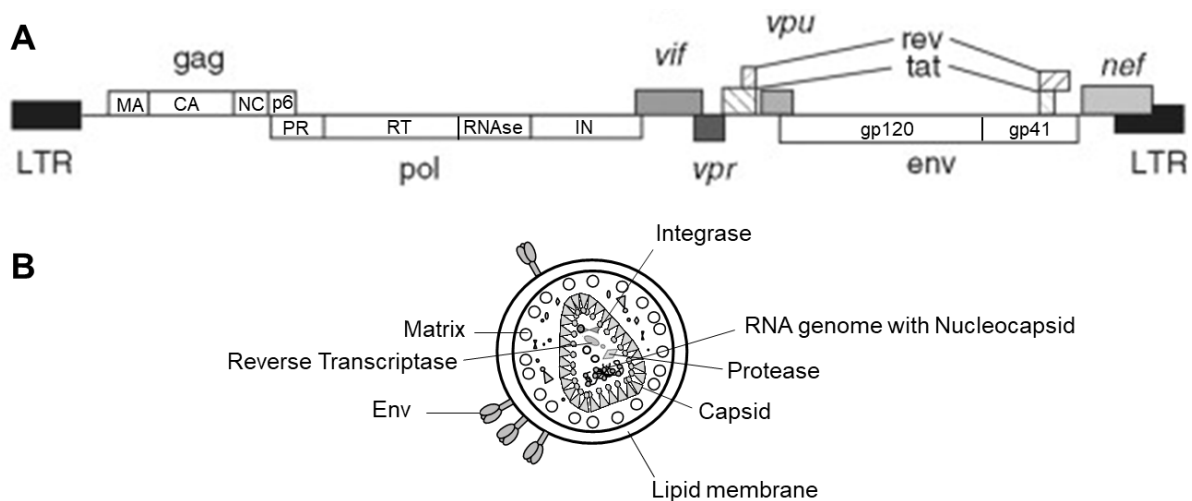


Fig. 1: HIV-1 genome and particle structure. A: HIV-1 genomic organization. The coding region is flanked by long terminal repeats (LTRs). Nine open reading frames (ORFs) are shown as boxes. Black lines depict proteolytic cleavage sites. Three major genes: *gag* (group specific antigen), *pol* (polymerase) and *env* (envelope). Gag protein in processed into MA, CA, SP1, NC, SP2 and p6. *pol* contains PR, RT, RNase H and IN. Additional genes encode for regulatory proteins Tat (transactivator of transcription) and Rev (regulator of virion), and accessory proteins Vif (virion infectivity factor), Vpr (viral protein R), Vpu (viral protein U) and Nef (negative factor). Adapted from Kirchhoff, 2009. **B:** Schematic illustration of a mature HIV-1 particle. Accessory proteins are omitted in the representation.

Gag encodes capsid proteins that are transcribed and translated as 55 kDa precursor protein (Fig. 2A). During maturation of the virion, the precursor protein is processed by the viral

protease (PR) into the 17 kDa matrix protein (MA), 24 kDa capsid protein (CA), 9 kDa nucleocapsid protein (NC), p6 and spacer peptide (SP) 1 and 2 (Fig. 1B, 2B) (Göttlinger 2002; Freed 2015; Sundquist und Kräusslich 2012).

Pol is expressed as a GagProPol fusion protein with a size of 160 kDa (p160) due to a frame shift at the 3' end of *gag*, (Fig. 2A). This frameshift occurs in 5% of translation events, causing a Gag:GagProPol ratio of 20:1 (Jacks et al. 1988; Garcia-Miranda et al. 2016). In the maturation process, the fusion protein is cleaved and Pol is further digested into the functional subdomains protease (PR, p10), reverse transcriptase (RT, p66 and p51), RNase H (p15), and integrase (IN, p32) (Fig. 1B, 2B, C) (Prescott et al., 1999). The RT p66/p51 dimer provides RNA- and DNA- dependent DNA polymerase activity and degrades RNA in RNA-DNA hybrids (RNase H activity). IN drives the integration of the viral genome into the host cell genome (provirus) (Farnet et al. 1996).

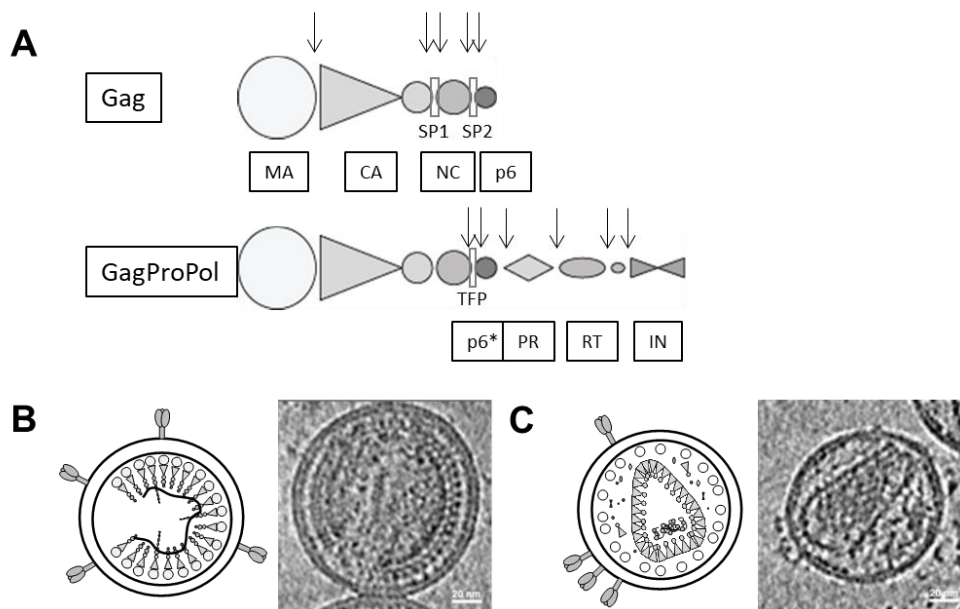


Fig. 2: Gag and GagProPol processing and formation of a mature viral particle. **A:** Schematic illustration of Gag and GagProPol polyproteins and their subunits. Arrows depict protease cleavage sites. Gag is processed into MA, CA, SP1, NC, SP2 and p6. GagProPol cleavage into PR, RT and IN. **B, C:** Schematic illustration and electron cryotomograms of **(B)** immature and **(C)** mature HIV-1. Spherical virion diameter is about 145 nm. Electron cryotomograms from (Mattei et al. 2016). Scale bar: 20nm.

Env encodes a 160 kDa protein that is transported through the secretory pathway to the plasma membrane and glycosylated during this process (gp160) (Fig. 1). It is cleaved by cellular proteases in two glycoproteins of 120 kDa (gp120) and 41 kDa (gp41). Gp41 is a transmembrane protein, while gp120 is located on the membrane surface. The mature domains are non-covalently bound (Wyatt und Sodroski 1998). Env forms heterodimeric trimers on the viral membrane, that interact with cellular receptors to enter the host cell (see 4.1.2) (Center et al. 2002). There are about 7-14 trimers per viral particle (Chertova et al. 2002; Zhu et al. 2003).

Regulatory proteins are Tat (transactivator of transcription) and Rev (regulator of virion), *vif* (virion infectivity factor), *vpr* (viral protein R), *vpu* (viral protein U) and *nef* (negative factor) encode accessory proteins (Fig. 1).

4.1.2 Replication-cycle of HIV-1

To enter the target cell, the HIV-1 envelope protein gp120 binds to the CD4 receptor on the cell surface of memory T-cells and macrophages (Fig. 3). This triggers a structural change in Env, which allows the interaction of gp41 with the cellular co-receptor (most importantly the β -chemokine receptor CCR5 or α -chemokine receptor CXCR4 (Sattentau und Moore 1991; Wu et al. 1996). The exposure of a hydrophobic fusion peptide due to Env and (co)receptor interaction induces the fusion of viral and cellular membranes. The viral contents enter the cytoplasm through the formed fusion pore (Rivière et al. 2010; Haffar et al. 2000) (Fig. 3 Entry). The viral capsid, the conical cone consisting of CA, that contains the viral genome, NC and Vpr, is delivered, but the exact fate of the core in different cell types is still under investigation. The RNA genome is reversely transcribed by the reverse transcriptase into double stranded DNA with duplicates of long terminal repeats (LTRs) (Chung et al. 2013). The viral dsDNA is part of a so-called pre-integration complex containing at least the viral dsDNA genome, IN and Vpr (Fig. 3 Reverse Transcription), which is transported to and through the intact nuclear pore, allowing infection of non-dividing cells (Fig. 3 Nuclear import). The role of the capsid in this process and the mechanism of nuclear entry is currently unclear.

Reverse transcription yields circular and linear double stranded viral DNA, but only linear DNA flanked with duplicates of LTRs can function as a precursor for the integration in the host genome. Viral DNA is mostly integrated in active euchromatin where the 5' LTR is applied as a eukaryotic promoter and the 3' LTR functions as the polyadenylation and termination site (Bushman et al. 1990) (Fig. 3 Integration). To increase genomic transcription, the cell is activated by Tat, that additionally leads to a higher efficiency of transcription elongation by recruitment of cellular factors such as RNA polymerase II (Kao et al. 1987; Karn und Stoltzfus 2012). Unspliced genomic RNAs are transported into the cytoplasm by Rev (Fig. 3 Transcription and mRNA Export). Viral proteins are translated in the cytoplasm and regulatory proteins are shuttled back into the nucleus (Fig. 3 Translation). Structural proteins and newly transcribed RNA genomes then assemble into progeny virions. Assembly and release are the main focus of this work and therefore described in more detail in the following chapter 4.1.2.1.

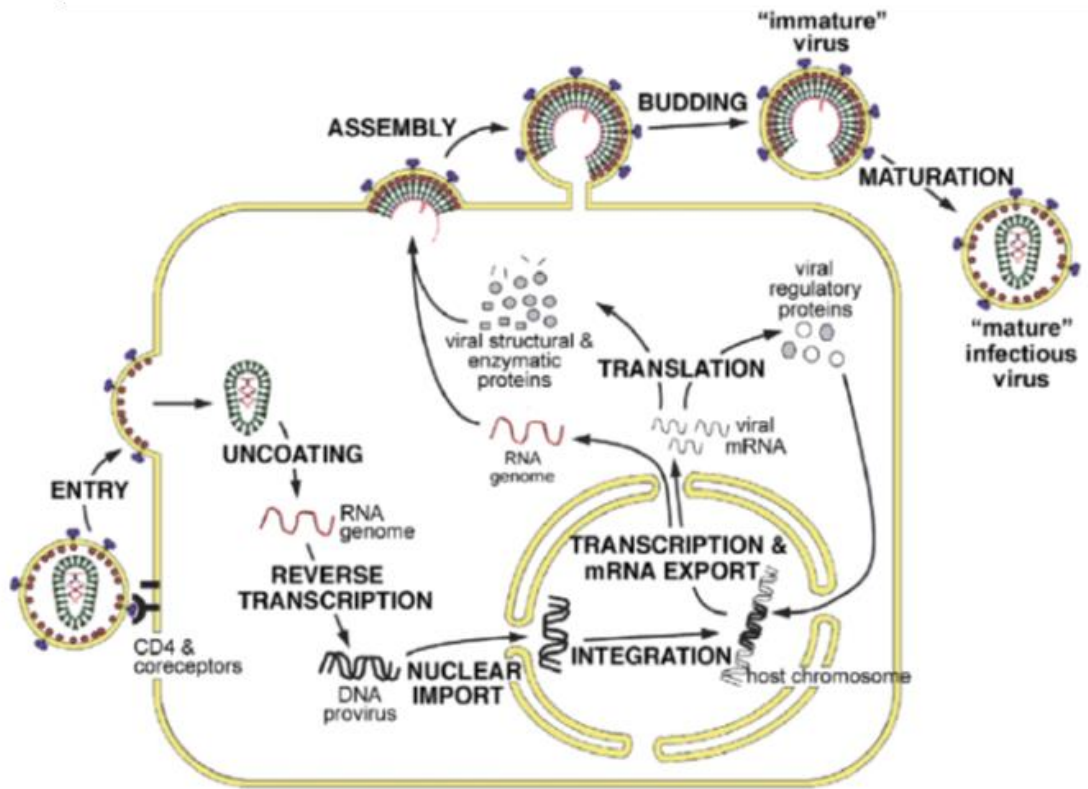


Fig. 3: Schematic replication cycle of HIV-1. HIV-1 binds to cellular CD4 and co-receptors on the plasma membrane. Viral entry occurs via membrane fusion (Entry). Contents are released in the cytoplasm and the viral genome is reverse transcribed from ssRNA to dsDNA (Reverse Transcription). The viral genome is transported into the nucleus and integrated in the host chromosomal DNA (Nuclear import and Integration). DNA is transcribed and mRNA is exported into the cytoplasm (Transcription and mRNA Export). Spliced mRNA is translated in viral proteins, unspliced genome incorporated in the viral particle (Translation). Gag assembles at the plasma membrane and recruits viral and cellular proteins (Assembly). The viral bud is pinched off by the cellular ESCRT machinery (budding). Gag and GagProPol are cleaved by the viral protease and structural rearrangement leads to formation of mature, infectious viral particles (Maturation). From (Ganser-Pornillos et al. 2008).

4.1.2.1 Assembly, budding and maturation

The Gag polyprotein drives viral assembly and is known to be sufficient for formation of non-infectious virus-like particles (Gheysen et al. 1989). Gag proteins traffic to the cytoplasm as monomers and dimers (Bieniasz 2009), while small amounts of Gag protein bind and thereby recruit the viral genome to the plasma membrane (Jouvenet et al. 2009). Gag contains an N-terminal myristoylation site in MA, that triggers the protein localization to the plasma membrane (Ghanam et al. 2012; Göttlinger et al. 1989). Basic residues in MA interact with acidic phospholipids at the inner leaflet of the plasma membrane and support membrane binding (Fig. 3 Assembly, 4) (Hermida-Matsumoto und Resh 1999; Zhou et al. 1994).

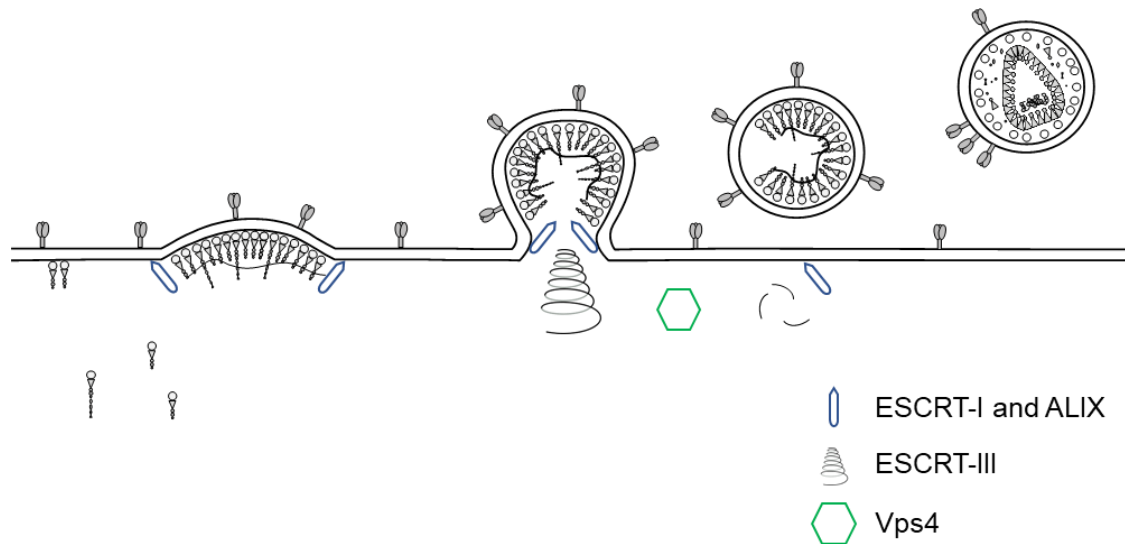


Fig. 4: Schematic representation of assembly, budding and maturation of HIV-1. Viral particles assemble at the plasma membrane. Gag forms the viral bud and recruits viral and cellular proteins, as well as the viral genome to the assembly site. Viral particles are released from the plasma membrane by the ESCRT machinery. Proteolytic processing of the structural proteins enables structural rearrangement and formation of mature, infectious viral particles.

MA drives the Gag membrane targeting and Env incorporation in the viral particle (Dorfman et al. 1994). Binding to the acidic phospholipid phosphatidylinositol 4,5- biphosphate triggers structural changes in MA that expose the myristoyl group (myristoyl switch) and anchor Gag to the plasma membrane (Ono et al. 2004). CA-SP1 harbors intermolecular interaction sites that drive Gag multimerization to form an immature lattice (Guo et al. 2005; Pak et al. 2017). GagProPol is incorporated by the same mechanism as Gag, while viral proteins like Vpr, Vif and Nef interact with the C-terminal p6 domain of Gag. The viral Env protein, is integrated in the viral membrane by interaction with MA to enable binding and infection of the host cell (Wyatt und Sodroski 1998). Released viral particles have a radius of ~63 nm and the immature Gag lattice contains ~2400 Gag and ~120 GagProPol molecules (Briggs et al. 2003; Carlson et al. 2008). Genesis of the full Gag lattice takes ~5-15 min, as determined by live-cell imaging of fluorescently labeled virus derivatives (Jouvenet et al. 2008; Ivanchenko et al. 2009).

Budding of virus particles from the membrane is mediated by the p6 domain of Gag, which recruits the cellular endosomal complex required for transport (ESCRT) machinery and drives Vpr incorporation in the viral particle (Accola et al. 2000; Martin-Serrano und Bieniasz 2003). The C-terminal domain of Gag, p6, was found to be crucial for virus release from the plasma membrane (Malim und Emerman 2008; Peterlin und Trono 2003). Virus variants lacking p6 stay attached to the plasma membrane by stalk-like structures (Göttlinger et al. 1991). A so-called 'late-domain' motif in p6 recruits Tsg101 and ALIX, components of the ESCRT complex, that further recruit the ESCRT-III complex (Huang et al. 1995). ESCRT-III forms a spiral-like structure in the viral bud, supposedly closing off the virus to the plasma membrane. It then recruits the AAA ATPase vacuolar protein sorting 4 (Vps4), which enables membrane scission and recycles ESCRT components after budding has been completed (Freed 2015). Super-resolution microscopy reveals co-localization of the ESCRT complex with the Gag assembly site (Baumgärtel et al. 2011; Bendjennat und Saffarian 2016; Bleck et al. 2014). Vps4 ATPase is recruited shortly before scission off the plasma membrane and the viral particle is released

20-25 min after assembly initiation (Ivanchenko et al. 2009; Jouvenet et al. 2011b; Johnson et al. 2018).

Gag and GagProPol are composed of folded domains separated by flexible linkers that mark PR cleavage sites. After the budding process, the immature virion matures by proteolytic cleavage of Gag and GagProPol precursor proteins (Fig. 2,3,4) (Sundquist und Kräusslich 2012). This process is described in more detail in 4.1.3. Shortly, PR dimerizes within GagProPol and autoprocesses in a precise order (Pettit et al. 1991; Pettit et al. 2005; Pettit et al. 1994; Tessmer und Kräusslich 1998). GagProPol cleavage releases functional PR, RT and IN (Louis et al. 1991; Louis et al. 1999; Louis et al. 1994; Wondrak et al. 1996). While the sequence of GagProPol processing is still under debate, Gag cleavage order is highly conserved (Tözsér 2010; Tözsér et al. 1997; Tözsér et al. 1991). Specific cleavage sites with varying susceptibility allow regulations of the scission process. This allows functional formation of condensed RNA genome in the assembled conical capsid. NC binds the viral genome and forms the condensed ribonucleoprotein particle (RNP). CA forms the conical core that encapsidates the RNP (Gorelick et al. 1990). Structural rearrangement of the proteins leads to formation of mature, infectious viral particles (Fig. 2B, 2C) (Ganser-Pornillos et al. 2008; Pettit et al. 1994; Swanstrom und Wills 1997; Vogt 1997).

4.1.3 HIV-1 protease – Key factor of maturation

Proteolytic processing of Gag and GagProPol polyproteins was found to be required for formation of infectious HIV-1. Viral particles lacking PR rendered the virus non-infectious. This indicates the significant role of proteolytic processing activity for viral infectivity (Henderson et al. 2012; Kohl et al. 1988; Peng et al. 1989). This crucial step in the HIV-1 life cycle is the target of important drugs used in HIV therapy. The mechanism of PR is described further in this chapter.

4.1.3.1 PR structure and function

The HIV-1 protease (PR) is an aspartyl protease that forms a symmetric homodimer of subunits comprising 99 amino acid residues (Fig. 5). Due to the homology to the cellular protease pepsin, the retroviral proteases are also called retropepsins (Barrett et al. 2012). The active site consists of three amino acids (Asp-Thr-Gly) and is stabilized by non-covalent interactions at the interface of the dimer (Pettit et al. 2003; Tessmer und Kräusslich 1998). For the proteolytic cleavage, two catalytic aspartic acid residues (D25), one from each subunit, activate a water molecule (Louis et al. 1999; Oroszlan und Luftig 1990; Wlodawer und Erickson 1993; Konvalinka et al. 2015). Two glycine-rich flexible loops at the top are called flaps, because they regulate substrate accessibility by conformational changes that allow substrate entering and exiting.

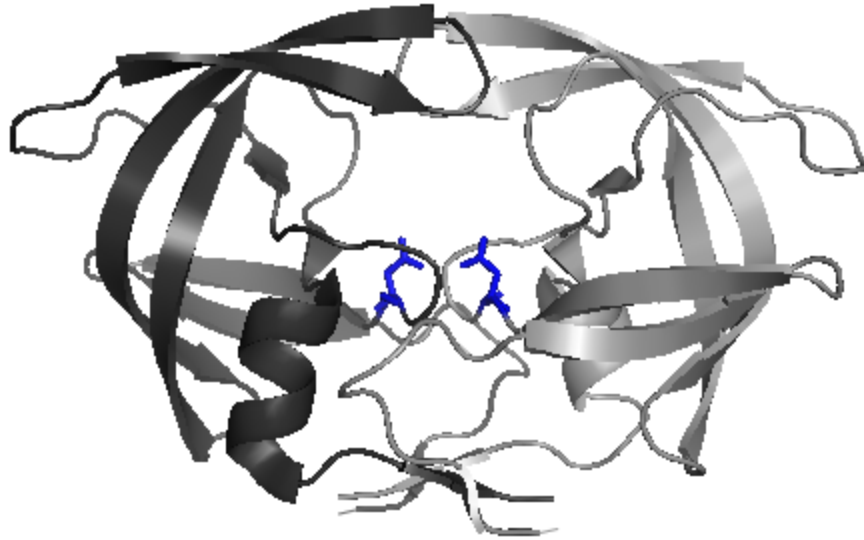


Fig. 5: Structure of HIV-1 PR. Subunits are identical but colored in black and grey for better identification. Blue residues mark the catalytically active Asp 25 and Asp 25' residues. Figure was generated using PyMol (www.pymol.org). PR structure adapted from from PDB ID: 3el1.

Substrates of PR are bound asymmetrically in an anti-parallel β -sheet conformation, so that the scissile bond is located in the center (Fig. 6). Mutation analysis of substrate showed the importance of amino acids up- and downstream of the scissile bond (Partin et al. 1990b; Partin et al. 1990a). Specificity studies revealed the necessary characteristics of the substrate. P_1 and P_1' were shown to exhibit large hydrophobic residues, while P_2 and P_2' contain hydrophobic or small polar side chains (Pettit et al. 2002). P_3 and P_3' sites were found to tolerate variable amino acids (Loeb et al. 1989; Pettit et al. 1991; Tözsér et al. 1997).

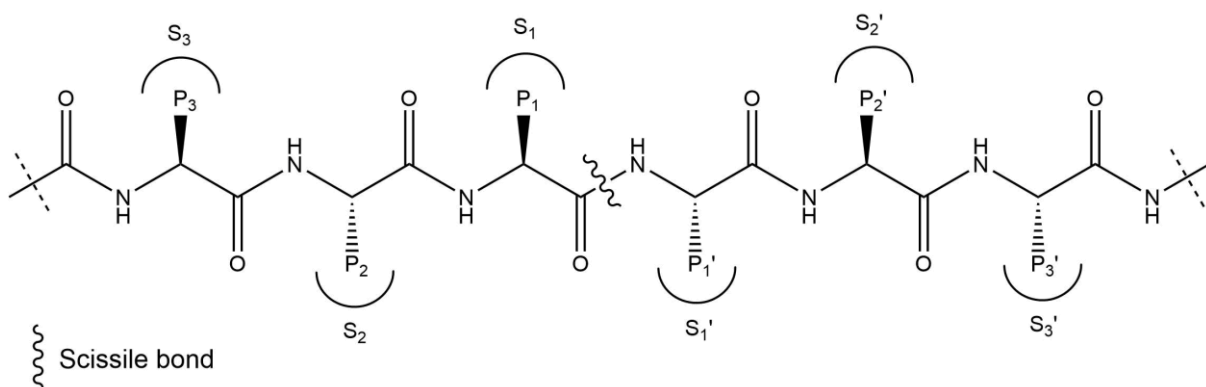


Fig. 6: Substrate interaction with the catalytic residues. Substrate is bound asymmetrically so that the scissile bond is located in the center. Amino acids on either side of the scissile bond bind to substrate cavity. P enumerates amino acid side-chains, S labels subsites of the enzyme cavities. Scissile bond between P_1 and P_1' . Figure was generated with ChemDraw.

4.1.3.2 Mechanism of PR function

HIV-1 PR uses an activated water molecule to attack the amide bond carbonyl of the substrate's scissile bond (Fig. 7). The activation of the water molecule is achieved by the two aspartyl β -carboxy groups at the active site. The water molecule acts as a nucleophile and attacks the carbonyl carbon of the scissile bond (James und Sielecki 1985).

The Asp side chain closer to the nucleophilic water molecule is assigned the negative charge (Fig. 7). The negative aspartate side chain activates the water by rendering it nucleophilic to attack the carbonyl group in the substrate scissile bond and to generate an oxyanion tetrahedral intermediate ("oxyanion hole"). The scissile amide N atom is protonated and molecular rearrangement results in the decomposition of the tetrahedral intermediate to the hydrolyzed products (Suguna et al. 1987; Berg et al. 2014).

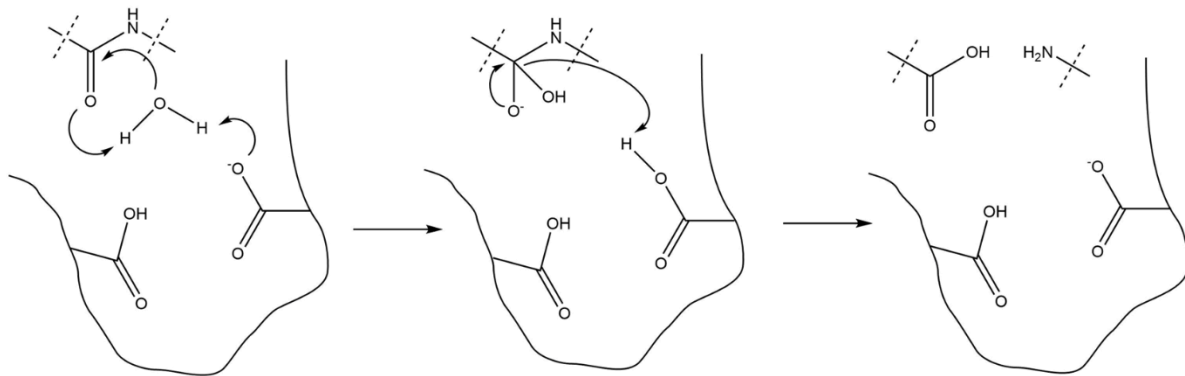


Fig. 7: Schematic representation of the mechanism of proteolytic cleavage. Activation of a water molecule by two aspartic acid residues to cleave the peptide bond. Figure was generated with ChemDraw.

4.1.3.2.1 PR auto-processing

Monomeric PR is expressed as subunit of the GagProPol polyprotein. It needs to dimerize in order to enable proteolytical activity (Pettit et al. 1994; Tessmer und Kräusslich 1998). The active sites of both subunits interact only weakly and show low dimer stability but is crucial for correct spacial approximation. Then, the N- and C-terminal amino acids of both domains can interact strongly and establish a stable dimer (Louis et al. 1991; Hayashi et al. 2014). Auto-processing of HIV-1 protease was shown to be tightly coupled to protein folding (Louis et al. 1999). The first cleavage is reported to occur at the SP1-NC cleavage site, followed by processing of the transframe region at TFP-p6* and p6*-PR respectively (Pettit et al. 1994; Phylip et al. 1992). A mutation in p6* was shown to influence PR activity (Chiu et al. 2006). TFP cleavage increases PR activity and is needed to allow proper folding of PR (Chatterjee et al. 2005; Huang und Chen 2010; Louis et al. 1991; Wan et al. 1996). PR-RT scission is the last step of self-processing and renders a catalytically active dimerized PR that subsequently cleaves Gag and GagProPol (Wondrak et al. 1996).

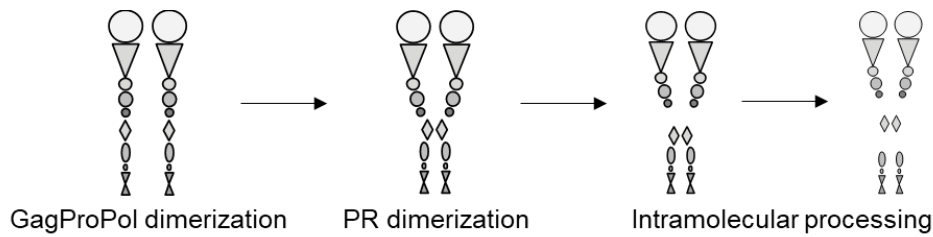


Fig. 8: Autocatalysis of HIV-1 PR from GagProPol. PR monomers need to dimerize as part of GagProPol to form the active site. PR auto-catalyses by cleaving off the N-terminal TFP and p6* first, PR-RT cleavage is last step of self-processing.

4.1.3.2.2 Cleavage of Gag and GagProPol

PR cleavage sites in Gag and GagProPol display different amino acid sequences but are all recognized by the viral PR. Sequence variations are thought to regulate cleavage sequence and rate by different binding affinities to the PR active site (Fig. 9) (Kräusslich et al. 1989; Pettit et al. 1994; Pettit et al. 2005; Wiegers et al. 1998). Most studies were performed by *in vitro* processing of peptides representing different cleavage sites or Gag-derived proteins with purified HIV-1 PR. Alternatively, viral particles lacking PR were concentrated and processed with purified PR (Konvalinka et al. 1995). Accumulation of cleavage products over time were detected by fluorography or immunoblot (Erickson-Viitanen et al. 1989; Konvalinka et al. 1995). These studies revealed uncleaved Gag polyprotein (p55) before PR addition. The order of cleavage was found to be highly conserved (Tözsér et al. 1997). Cleavage sites were classified based on their processing rate (Pettit et al., 1994). Upon proteolytic processing, p40 (MA-CA-SP1) and p15 (NC-SP2-p6) were detected rapidly (Fig. 9). SP1-NC was shown to be the first processing event and therefore determines the Gag cleavage rate (Fig. 9) (Oliveira et al. 2003). Intermediate processing was observed for SP2-p6 (9x slower than SP1-NC) and MA-CA (14x slower than SP1-NC). Slow, and therefore late cleavage was measured for NC-SP2 (350x slower than SP1-NC) and CA-SP1 (400x slower than SP1-NC) (Pettit et al. 1994). Blockage of any individual cleavage site except NC-SP2 impaired viral infectivity (Coren et al. 2007; Marco et al. 2010; Lee et al. 2012; Müller et al. 2009; Wiegers et al. 1998).

Free NC binding to the viral genome leads to condensation of the RNP. Free CA assembles as the conical capsid and encloses the genome. Regulation of the processing order is therefore crucial for formation of functional and formation of infectious viral particles. This is supported by studies that observe impaired viral infectivity upon weak protease inhibition and by its premature activation (Figueiredo et al. 2006; Kaplan et al. 1994; Müller et al. 2009). An obligatory dimeric protease expressed as GagProPol component does not form viral particles due to premature Gag and GagProPol cleavage (Kräusslich 1991). A delay of virus release from the plasma membrane was found to cause viral particles to lack RT and PR (Bendjennat und Saffarian 2016).

While the processing order of Gag was studied in detail, the proteolytic cleavage in respect to virus assembly is not well understood. Due to asynchronous virus assembly between cells and differences for individual budding sites, bulk analysis by biochemical approaches is not applicable here. The timeframe of Gag processing was studied by induced HIV-1 PR activity in purified viral particles (Hanne et al. 2016; Mattei et al. 2014; Schimer et al. 2015). In these studies, immature viral particles were produced in the presence of PR inhibitors. In the first

study, the inhibitors were washed out and the cleavage products were analyzed over time. While Gag processing products were observed by immunoblot, viral infectivity was not recovered (Mattei et al. 2014). Delayed processing by slow dissociation of the inhibitor dissociation from the HIV-1 active site was discussed to cause the hampered infectivity. Therefore, the next studies applied a photodegradable inhibitor, that was rapidly inactivated. Here, 30% of mature CA was produced within 15 min, but full Gag cleavage was not achieved (Schimer et al. 2015). Visualization of conformational changes by super-resolution microscopy and quantification of mature and immature VLPs over time resulted in $t_{1/2}$ of ~30 min for virus maturation (Hanne et al. 2016).

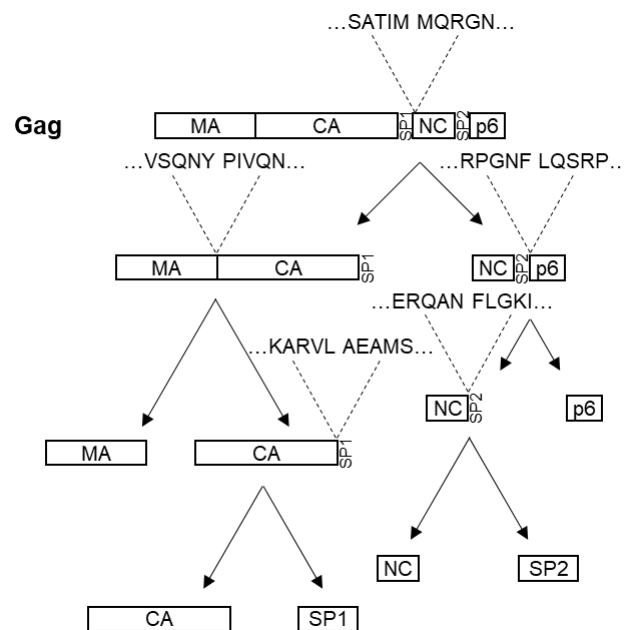


Fig. 9: Gag cleavage sites and order of proteolytical processing events. Rapid cleavage of SP1-NC, intermediate processing of SP2-p6 and MA-CA and slow scission of NC-SP2 and CA-SP1. Different cleavage sequences are believed to influence binding affinity of the PR active site and therefore regulate proteolytical processing.

While the order of cleavage events that are involved in autocatalysis of PR are known, the sequence of processing in Pol is not fully elucidated. (Tözsér et al. 1991) support the cleavage of RT-IN, followed by PR-RT and RT-RNaseH (Könnyű et al. 2013). Alternatively, a simultaneous release of PR, RT, RNase H and IN was discussed (Craven et al. 1991).

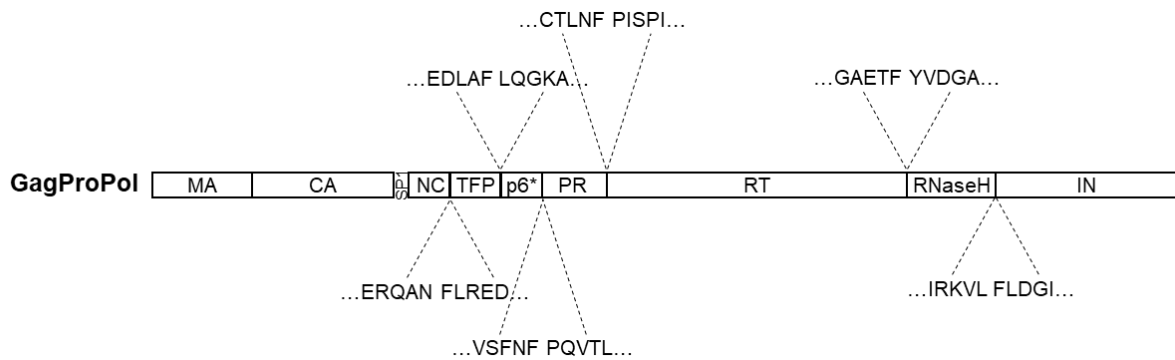


Fig. 10: Specific PR cleavage sites in GagProPol. TFP-p6* and p6*-PR cleavage increases proteolytic activity. RT-IN may be cleaved prior to PR-RT, which is followed by RT-RNaseH processing. Alternatively, Pol is cleaved simultaneously.

4.1.3.3 PR inhibitors

The first PR inhibitor approved by the FDA was saquinavir in 1995 (James 1995). Combination of different drugs in antiretroviral therapy (ART) decreased the mortality of AIDS-related deaths in the USA from 50000 to 18000 people a year (La Porte 2009). Today, there are nine protease inhibitors approved for HIV-1 therapy: saquinavir (SQV), ritonavir (RTV), indinavir (IDV), nelfinavir (NFV), amprenavir (APV), lopinavir (LPV), atazanavir (ATV), tipranavir (TPV) and darunavir (DRV). Structural and biochemical analyses of the HIV-1 active site were conducted for the rational design of the drugs. All protease inhibitors with the exception of DRV are competitive inhibitors: they represent non-cleavable peptide analogs, that bind to the active site of PR with high affinity and compete with Gag binding but do not prevent auto-processing (Fig. 11). DRV was found to additionally prevent PR dimerization (Humpolíčková et al. 2018). All together, they bind to the active site of the dimer and prevent cleavage of Gag, and thereby maturation, which leads to a release of immature, non-infectious viral particles (Patick und Potts 1998). Protease inhibitors are designed to mimic the tetrahedral intermediate formed during the cleavage mechanism, but scission of the bond by viral protease does not occur (Konvalinka et al. 2015). Drug resistance of the virus is observed upon treatment; it arises through mutations in PR, but also in Gag (Côté et al. 2001; Dam et al. 2009; Fun et al. 2012). Mutations in HIV-1 proteins are caused by the lack of proof-reading of the viral RT and are further selected for reduced inhibitor susceptibility. Initial resistance mutations are also referred to as primary mutations because they are the first mutations selected. They usually change the structure of the active site cavity, so that the binding of the drug to the viral PR is hampered, which results in resistance to PIs (Gulnik et al. 1995). While primary mutations additionally reduce HIV-1 PR activity, secondary and tertiary mutations are observed in patients over time, that do not reduce binding of the inhibitor to PR but increase proteolytic activity (Nijhuis et al. 1999). Structural similarities of the inhibitors may lead to cross-resistance. Therefore, new drugs need to be designed that address different mechanisms of inhibition.

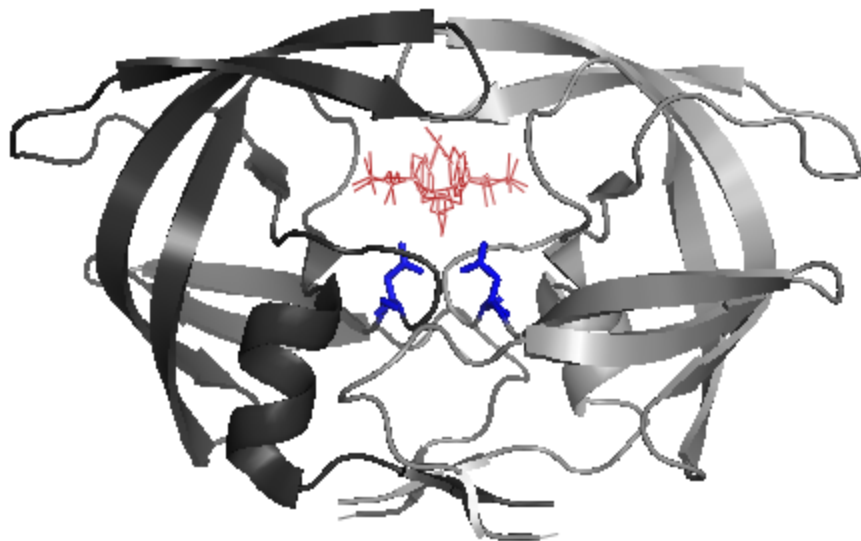


Fig. 11: PR inhibitor bound to the active site of HIV-1 PR. Subunits are identical but colored in black and grey for better identification. Blue residues mark the catalytically active Asp 25 and Asp 25' residues. Red structure illustrates inhibitor Atazanavir bound to the active site. Figure was generated using PyMol (www.pymol.org). PR structure adapted from from PDB ID: 3el1.

PR inhibitors bind to the active site with varying rate constants. While the association with the active site is described by k_{on} ($M^{-1}s^{-1}$), the dissociation rate with k_{off} (s^{-1}) and $t_{1/2}$ (s) the halftime for the molecule to bind. PR inhibitors in general bind strongly to the active site. Dissociation rate are more variable (Dierynck et al. 2007). While DRV does not dissociate form the active site, RTV features a short $t_{1/2}$.

	RTV	LPV	DRV
$k_{on}(M^{-1}s^{-1}) \pm SEM$	$5.8 \pm 1.1 \cdot 10^5$	$8.6 \pm 0.8 \cdot 10^5$	$2.2 \pm 0.8 \cdot 10^6$
$k_{off}(s^{-1}) \pm SEM$	$8.1 \pm 1.1 \cdot 10^{-4}$	$1.6 \pm 0.1 \cdot 10^{-4}$	$7.8 \pm 0.5 \cdot 10^{-7}$
$t_{1/2}(s)$	860	4300	890000

Fig. 12: Selected PR inhibitor structures and respective kinetic parameters for binding to the active site of HIV-1 PR. Ritonavir (RTV), Lopinavir (LPV) and Darunavir (DRV) structures generated with ChemDraw. Rate constants and $t_{1/2}$ from (Dierynck et al. 2007).

4.2 Fluorescence labeling of virus-like particles

In this project, we want to observe the HIV-1 PR activity during the viral assembly. Therefore, we need to visualize the formation of new viral particles at the plasma membrane in combination with utilization of sensors to detect proteolytic activity or active HIV-1 PR over time.

Fluorescence labeling of viral particles allows detection of dynamic events during the viral life cycle. It is crucial that labeling of HIV-1 does not alter functions and infectivity of the virus (Campbell und Hope 2008). For visualization of viral assembly, application of fully infectious virus is unnecessary. A subviral derivative lacking LTRs and Nef, where reverse transcription is disabled to render the virus non-infectious (pCHIV) was generated previously and shown to be suitable for studying viral assembly (Lampe et al. 2007) and therefore has been applied in this work.

4.2.1 Fluorescence tags inserted in Gag

Insertion of fluorescent proteins in Gag, between MA and CA, was found to be tolerated in viral particles (Fig. 13B). eGFP was inserted and designed to stay attached to MA upon proteolytic processing (Müller et al. 2004). While the tagged virus formed viral particles with reduced infectivity, it was observed that mixing of labeled and unlabeled Gag in an equimolar ratio reconstitutes full infectivity of the virus (Müller et al. 2004). Gag labeling with eGFP was shown to allow detection of assembly sites at the plasma membrane by fluorescence microscopy (Baumgärtel et al. 2012; Ivanchenko et al. 2009; Jouvenet et al. 2011a). These sites were tracked, and the signal intensity increase was analyzed over time. The assembly kinetics of labeled Gag were observed to exhibit saturating exponential curves (Ivanchenko et al. 2009; Jouvenet et al. 2008; Mücksch et al. 2017; Rahman et al. 2014).

4.2.2 Fluorescence tags inserted by coupling to Vpr

Vpr is an accessory protein of HIV-1. It interacts with the p6 domain of Gag and gets incorporated in the viral particle by Gag recruitment (see 4.1.1 and 4.1.2.1). A molar ratio of Vpr to Gag of 1:7 was determined based on radioactively labeled highly purified virions (Müller et al. 2000). Vpr was discovered as tool to introduce foreign proteins in the viral particle by fusion to Vpr (Wu et al. 1996). Linkage of a fluorescent protein to Vpr was described in 2002 to allow visualization of the viral entry (Fig. 13A) (McDonald et al. 2002). Expression of Vpr in *trans* also enables double-labeling of viral particles (Fig. 14) (Lampe et al. 2007). For exogenous Vpr incorporation, higher molar ratios of Vpr to Gag of up to 1:2 were described, resulting in up to ~1000 Vpr molecules in the viral particle. Incorporation of exogenous Vpr was observed to hamper Gag processing; therefore, it needs to be regulated carefully (Lampe et al. 2007; Sood et al. 2017).

4.3 Fluorescence-based methods applied in this study

In this study, HIV-1 proteolytic activity and formation of active PR was measured during the viral assembly process. Light microscopy enables detection of events in living cells. But the resolution is limited due to its dependence of the wavelength (λ) and the numerical aperture (NA) of the microscope lense:

$$Resolution (r) = \frac{\lambda}{2 \cdot NA}$$

Applying a laser with 488 nm wavelength allows for a resolution of ~240 nm. HIV-1 is known to have a diameter of 120 nm, so it cannot be resolved. Therefore, fluorescence characteristics like FRET are applied to measure changes in the viral particle (see 4.3). Super-resolution STED microscopy increases the resolution of fluorescence microscopy to ~20 nm and therefore can be applied to resolve viral structures as well (Hell und Wichmann 1994; Hanne et al. 2016).

Either, external sensors were cleaved by the viral PR, Gag processing was observed, or active PR was labeled.

4.3.1 Bimolecular fluorescence complementation assays detect Gag processing

BiFC assays are applied for visualization of protein interactions in living cells (Kerppola 2006, 2008). In this assay, fluorescent proteins are split in two subunits that are non-fluorescent individually. GFP-based proteins are β -barrels consisting of eleven β -strands that are all necessary for the formation of the fluorophore. They may be split in N- and C-terminal domains, or β 1-10 and β 11 (Cabantous et al. 2005; Cabantous und Waldo 2006), which are both non-fluorescent; fluorescence is reconstituted by association of both parts upon co-expression in the same cell. This has been exploited to monitor protein-protein interactions. β 1-10 and β 11 are linked to different target proteins and interaction of the target proteins is detected upon generation of fluorescence signal. We have explored a different application in this study, incorporating split subunits of the yellow fluorescent protein Venus (Hernandez und Sandri-Goldin 2011) and sfGFP in Gag between the MA and CA domain. Constraint of the subunits within the unprocessed polyproteins was presumed to impair reconstitution of the fluorophore, while release by PR mediated processing should allow association (Fig. 26).

4.3.2 Förster resonance energy transfer to detect proteolytic activity

HIV-1 PR activity was measured by fluorescence-based studies since the 1990s. It was described, that PR cleaves HIV-1 Gag processing sites independent of the flanking proteins. This allowed the design of peptide probes that gain a fluorescent signal upon proteolytic processing due to e.g. clipping of a quencher (Baum et al. 1990; Richards et al. 1990). Mostly, the measurements were conducted *in vitro*, e.g. spectrofluorometry. Here, either purified proteins of viral particles were subject to proteolytic cleavage by purified HIV-1 PR (Baum et al. 1990; Gaber et al. 2013; Müller et al. 2014; Richards et al. 1990).

The FRET-based assay utilizes the Förster resonance energy transfer (FRET) technique which was initially described by Theodor Förster in 1946 (Förster 1948). FRET relies on the energy transfer between a donor and an acceptor fluorophore providing that the emission peak of the donor molecule overlaps the excitation peak of the acceptor molecule and that both fluorophores are in close proximity of their Förster radius (approximately 10Å) (Lam et al. 2012; Gaber et al. 2013). Following excitation of the donor fluorophore, energy is directly transferred to the adjacent acceptor fluorophore by dipole-dipole interactions leading to the excitation of the latter. Since FRET efficiency directly correlates with the distance of the fluorophores, it is an established technique to analyze protein interactions between two fluorescently labeled proteins. Different FRET-pairs like mCerulean and mCitrine or GFP and mCherry had been applied to observe HIV-1 PR activity in cells (Gaber et al. 2013; Yang et al. 2012). Here, FRET was analyzed by fluorescence microscopy, or as FACS-based FRET assay by flow cytometry (Banning et al. 2010).

For a FRET-based analysis of PR activity, the fluorescent proteins Clover and mScarlet were coupled via a HIV-1 PR cleavage site (as found in Gag between MA and CA) and linked to Vpr to enable its incorporation in viral particles (Lam et al. 2012; Bindels et al. 2017).

4.3.3 Fluorescence lifetime-resolved imaging to detect Gag processing

Fluorescence lifetime measurements (FLIM) are based on monitoring of fluorescence decay over time. After excitation, fluorescent proteins require a specific time for transformation from the excited to the ground state (Clegg et al. 2003). Different lifetime components of the same molecule may form due to variations on molecular species or conformation (Digman et al. 2008). This lifetime is independent on the signal intensity but changes due to molecular interactions, e.g. decreases upon energy transfer of the protein as FRET-donor. eCFP was found to form homo-FRET pairs by interacting with surrounding eCFP proteins, and dimerization of eCFP led to a decrease of its fluorescence lifetime.

Here, eCFP was utilized for FLIM measurements, because it performs homo-FRET, which reduces the influence of protein incorporation (Poëa-Guyon et al. 2013). Molecular crowding induced homo-FRET of eCFP, resulting in a decrease of fluorescence lifetime (Kremers et al. 2006).

In this work, eCFP was inserted in Gag between MA and CA, either flanked with PR cleavage sites or one cleavage site between the fluorescent protein and CA. Gag multimerization should lead to a decrease of fluorescence lifetime due to molecular crowding, while proteolytic processing should be detected via increase of fluorescence lifetime.

4.3.4 Fluorogenic probes to stain active PR

The spectrum of fluorescence tags was expanded with the design of self-labeling enzymes that covalently bind substrates. SNAP (O⁶-alkylguanine-DNA-alkyltransferase) and Clip (O⁶-alkyl-cytosine-DNA-alkyltransferase) form a covalent bond with tags coupled to silicone-rhodamine (SiR) (Correa et al. 2013; Gautier et al. 2008; Lukinavičius et al. 2018). The resulting fluorescence signal of SiR is in the far-red (excitation maximum: 645 nm, emission

maximum: 661 nm) range, enabling multiple labeling of viral particles (GFP excitation maximum: 488 nm, emission maximum: 525 nm).

As a fluorogenic dye, SiR fluoresces upon binding to a target protein. The equilibrium between a non-fluorescent lactonic and fluorescent zwitterion structure is sensitive to hydrophobic effects (Lukinavičius et al. 2013). The SNAP-tag was inserted in Gag previously and enabled staining of Gag.SNAP in viral particles with SNAP-Cell 647-SiR (Eckhardt et al. 2011). Intracellular proteins were previously labeled by transient binding of SiR-coupled inhibitor derivatives for cytoskeletal filaments F-actin and microtubule (Lukinavičius et al. 2014).

In this study, SiR was coupled to the PR inhibitor RTV, which specifically binds to the active site of HIV-1 PR, as described before. SiR-RTV was shown to fluoresce upon binding to the PR active site due to conformational changes in SiR depending on the environment. Different linkers were tested concerning their influence on fluorogenicity of the probe upon binding to active HIV-1 PR, as well as unspecific background signal.

4.3.5 Single virus tracking at assembly sites

In this study, laser scanning confocal and TIRF microscopy were applied to image fluorescently labeled purified virus-like particles (VLPs) and assembly sites at the plasma membrane of HeLa Kyoto cells.

Confocal imaging scans the probe point-by-point with a xy-resolution of about 200 nm and a z-resolution of 500 nm (sample penetration). This reduces the time-resolution and increases cellular background (Balagopalan et al. 2011). TIRF microscopy is a widefield imaging-based technique, where light is directed towards the sample in a critical angle and therefore reflected at the glass surface. The evanescent wave of the reflected light can penetrate the sample for about 200 nm (Mattheyses et al. 2010). EMCCD-camera-based detection allows sensitive, high time resolution imaging with a z-resolution of 200 nm. Therefore, TIRF microscopy was applied for live-cell imaging of the assembly process to detect increasing numbers of punctae over time.

4.4 Aim of the work

Regulation of Gag proteolysis with respect to virus assembly is critical, but time and site of maturation initiation are currently unclear. The duration of the process and its structural intermediates are also unknown. Most analyses of PR activity were performed in vitro and therefore studied independent of viral assembly (Konvalinka et al. 2015).

The aim of this project was the time-resolved detection of proteolytic activity, Gag processing and formation of active PR during the viral assembly process by live-cell fluorescence microscopy.

With the aim to monitor HIV-1 PR activity in parallel to virion assembly by live-cell microscopy, I designed a Förster resonance energy transfer (FRET)-based PR sensor. For this, a FRET pair of autofluorescent proteins Clover and mScarlet was linked via a PR cleavage site and fused to the viral protein r (Vpr) to mediate recruitment to viral assembly sites and particle incorporation.

Different tags were inserted in Gag that indicate processing and conformational changes in the viral protein. Specifically, a bimolecular fluorescence complementation assay was designed to generate a fluorescent signal upon proteolytic cleavage of Gag. Next, a fluorogenic dye applicable for super-resolution microscopy was utilized to resolve changes in spatial distribution of Gag to discriminate mature and immature viral particles. Lastly, changes in fluorescence lifetime of the fluorescent protein eCFP depending on localization in the Gag lattice or free diffusion in the viral particle were measured.

Furthermore, specific labeling of active HIV-1 PR by a fluorogenic inhibitor was explored. This innovative approach combines the fluorogenic properties of SiR with the specificity of RTV to active HIV-1 PR.

Together, these sensors were applied to shed light in the dynamic coordination of viral assembly and HIV-1 PR activity.

5 Materials and Methods

5.1 Materials

5.1.1 Laboratory Equipment

Name	Company
Bacterial Shaker Multitron Pro	Infors HT, Bottmingen, Switzerland
C1000 Touch Thermal Cycler	BioRad, Hercules, USA
Centrifuge Avanti J-26 XP	Beckman Coulter, Brea, USA
CFX 96 Real Time PCR detector (for SG- PERT)	BioRad, Hercules, USA
Flow cytometer FACS AriaTM	BD Biosciences, Heidelberg, Germany
Flow cytometer FACS Canto HTS	BD Biosciences, Franklin Lakes, USA
Gel iX Imager (Agarose gel UV-imager)	INTAS Science Imaging, Göttingen
Hamilton® TLC syringe: 10 µl, 26s ga, needle, fixed	Hamilton, Reno, USA
Heraeus Megafuge 40R Centrifuge	Thermo Scientific, Waltham, USA
H-TIRF inverted Eclipse Ti2 microscope	Nikon Instruments Inc., Melville, USA
Ice Maker AF 103	Scotsman, Sprockhövel
Incubator C200	Labotect Labor-Technik-Göttingen, Rosdorf
L8-70M Ultracentrifuge with SW28 and SW32 rotor	Beckman Coulter, Brea, USA
Leica DMIL Led Fluorescent Microscope	Leica Microsystems, Wetzlar
Leica TCS SP2 laser scanning confocal microscope	Leica Microsystems, Wetzlar
Leica TCS SP8 laser scanning confocal microscope	Leica Microsystems, Wetzlar
LiCor Odyssey Imager CLx	LiCor Bioscience, Lincoln, USA
Light Microscope ELWD 0.3 T1-SNCP	Nikon Instruments Inc., Melville, USA

Microbiological Cabinet	Envair, Emmendingen
Microwave for Agarose gels	Sharp, Cologne
NanoPhotometer	Implen, Munich
PCR FlexCycler ²	Analytik Jena, Jena
Plate Reader Infinite M200 Pro	Tecan, Männedorf, Switzerland
Roller Mixer SRT6	Stuart, Staffordshire, UK
SDS-PAGE electrophoresis chamber Mighty small	Hoefer, Almstetten
Semi-Dry Blotter Fastblot B32	Whatman Biometra, Göttingen
Spectrofluorometer FP-8500	Jasco, Pfungstadt
Speed Vac	H. Saur, Reutlingen
STED system 775nm	Abberior Instruments GmbH, Göttingen
Thermomixer, Eppendorf, Thermomixer® comfort	Eppendorf, Hamburg
TL-100 Ultracentrifuge with TLA 45 rotor (Tabletop)	Beckman Coulter, Brea, USA
TLC Glass chamber	Desaga, Wiesloch
Vortex Genie 2	Scientific Industries, Bohemia, USA
Warming Cabinet	Memmert, Schwabach
Water Filtering System	Stakpure, Niederahr
Waterbath MP	Julabo, Seelbach
XS40025 Deltarange Weight Scale	Mettler Toledo, Gießen

5.1.2 Reagents

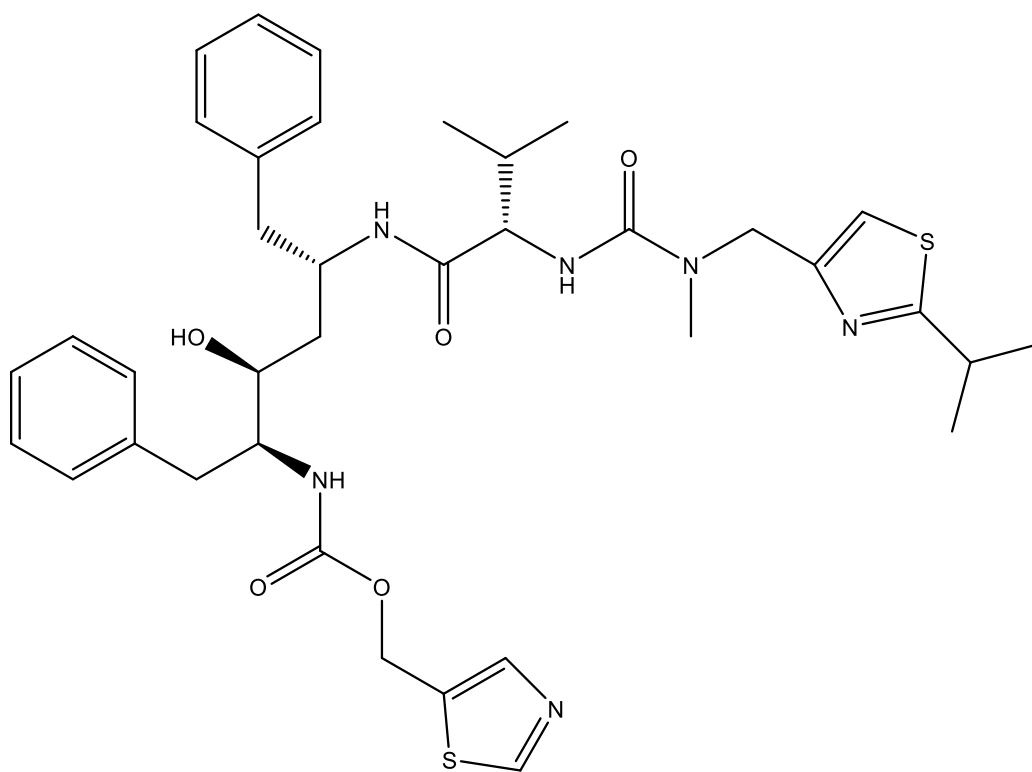
5.1.2.1 Chemicals and consumables

Name	Company
Agarose NEE0	Carl Roth, Karlsruhe
Ammonium persulfate (APS)	Sigma Aldrich, St. Louis, USA
Acrylamide 30 %	Applichem, Karlsruhe
β -Mercaptoethanol	Sigma-Aldrich, St. Louis, USA
Blasticidin	Thermo Scientific, Waltham, USA
Bromophenol blue	Chroma, Fürstfeldbruck
BSA 100x	NEB, Ipswich, USA
Blotting paper	3 MM Chr, Whatman, Dassel, Germany
DMSO	Merck, Darmstadt
DNA ladder 1 kb Plus	Thermo Scientific, Waltham, USA
dNTP Set	Thermo Scientific, Waltham, USA
Dulbecco's Modified Eagle Medium (DMEM)	Invitrogen, Karlsruhe
Ethanol (99 %) (EtOH)	Zentralbereich INF, Heidelberg
Fetal Calf Serum (FCS)	Biochrom, Berlin
FluoroBrite DMEM	Thermo Scientific, Waltham, USA
Fugene HD	Roche, Basel, Switzerland
Gel Loading Dye, Purple (6x) for DNA	New England Biolabs, Ipswich, USA
GlutaMAX Supplement	Thermo Scientific, Waltham, USA
Isopropanol	Sigma-Aldrich, St. Louis, USA
LI-COR Blocking Buffer	LI-COR Bioscience, Lincoln, USA
Methanol (MeOH)	Sigma-Aldrich, St. Louis, USA
Nitrocellulose membrane	Protran, Schleicher & Schull/Whatman, Dassel, Germany

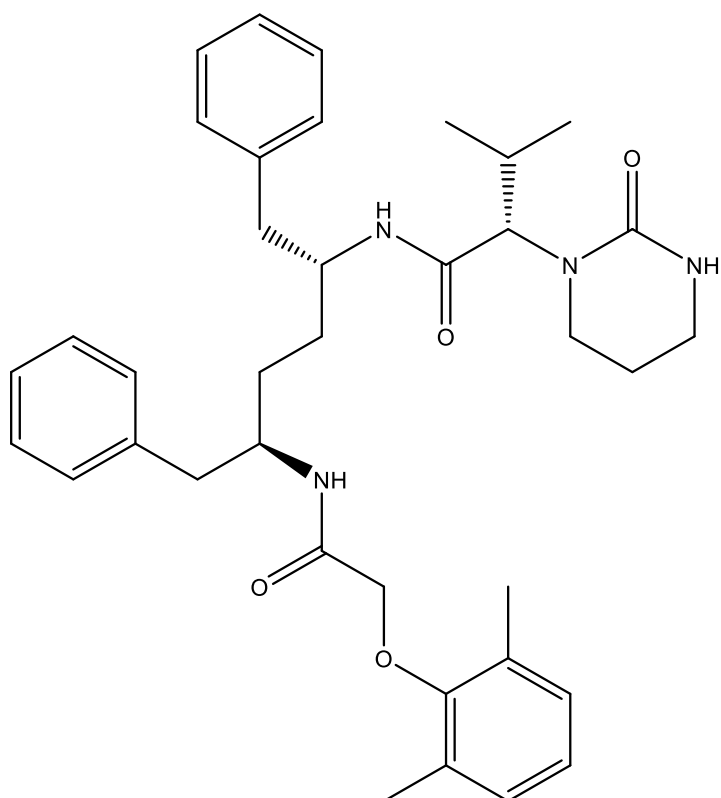
PageRuler prestained	Thermo Scientific, Waltham, USA
Penicillin Streptomycin (PenStrep)	Thermo Scientific, Waltham, USA
Reaction tubes (0.5-2ml)	Sarstedt, Nümbrecht
RNase Inhibitor, Ribolock	Thermo Scientific, Waltham, USA
Serological pipettes	Sarstedt, Nümbrecht
Single Channel Pipettes, PIPETMAN classic™ (10-1000 µl)	Gilson, Middleton, USA
Sodium Acetate	Sigma-Aldrich, St. Louis, USA
Sodium Chloride	Sigma-Aldrich, St. Louis, USA
Sodium dodecyl sulfate (SDS)	Applichem, Karlsruhe
Sodium Pyruvate (100 mM)	Thermo Scientific, Waltham, USA
Sulfuric acid	Fluka, Steinheim
Tetramethylethylenediamine (TEMED)	Sigma Aldrich (St. Louis, USA)
Tris[(1-benzyl-1H-1,2,3-triazol-4yl)methyl]amine	Sigma-Aldrich, St. Louis, USA
Triton X-100	Sigma-Aldrich, St. Louis, USA

5.1.2.2 Protease Inhibitors

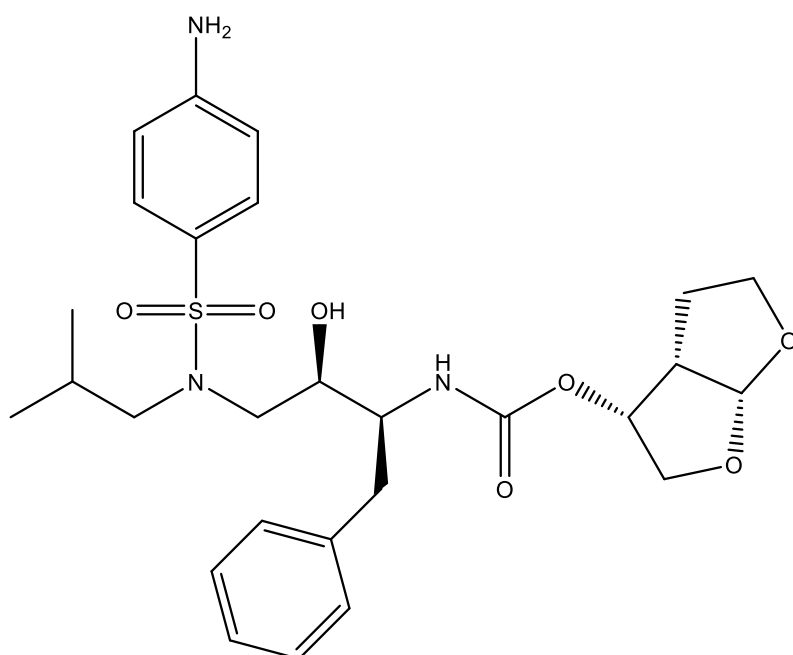
Ritonavir



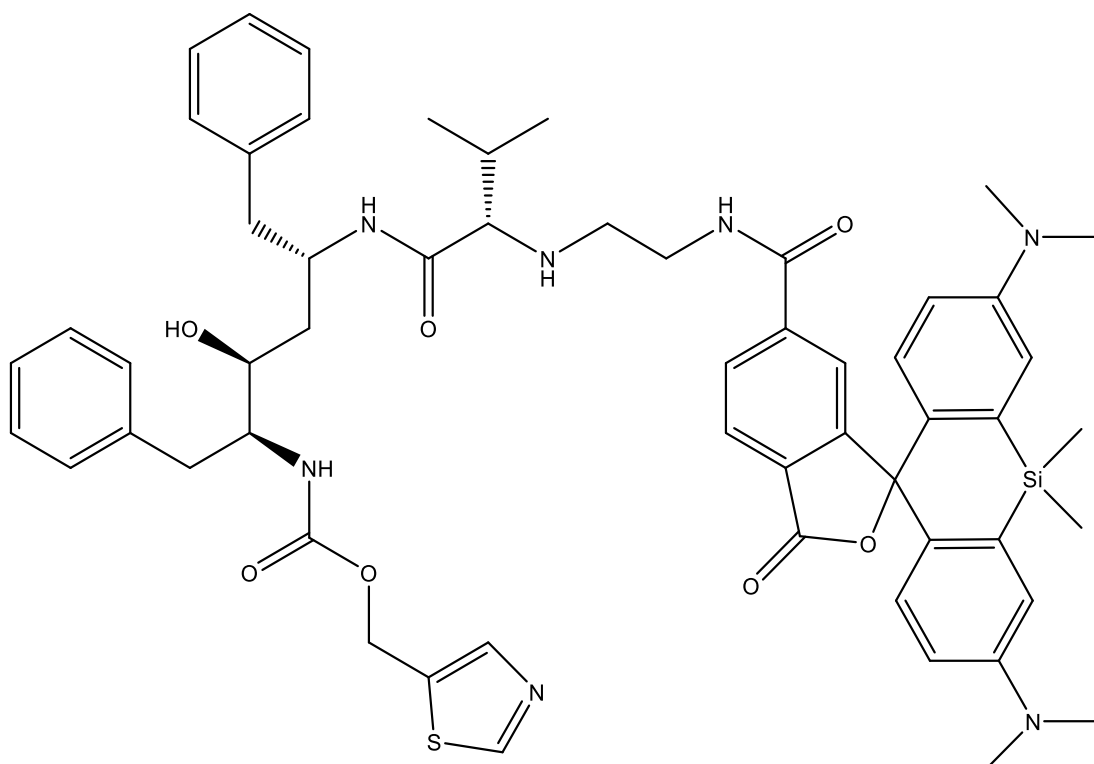
Lopinavir



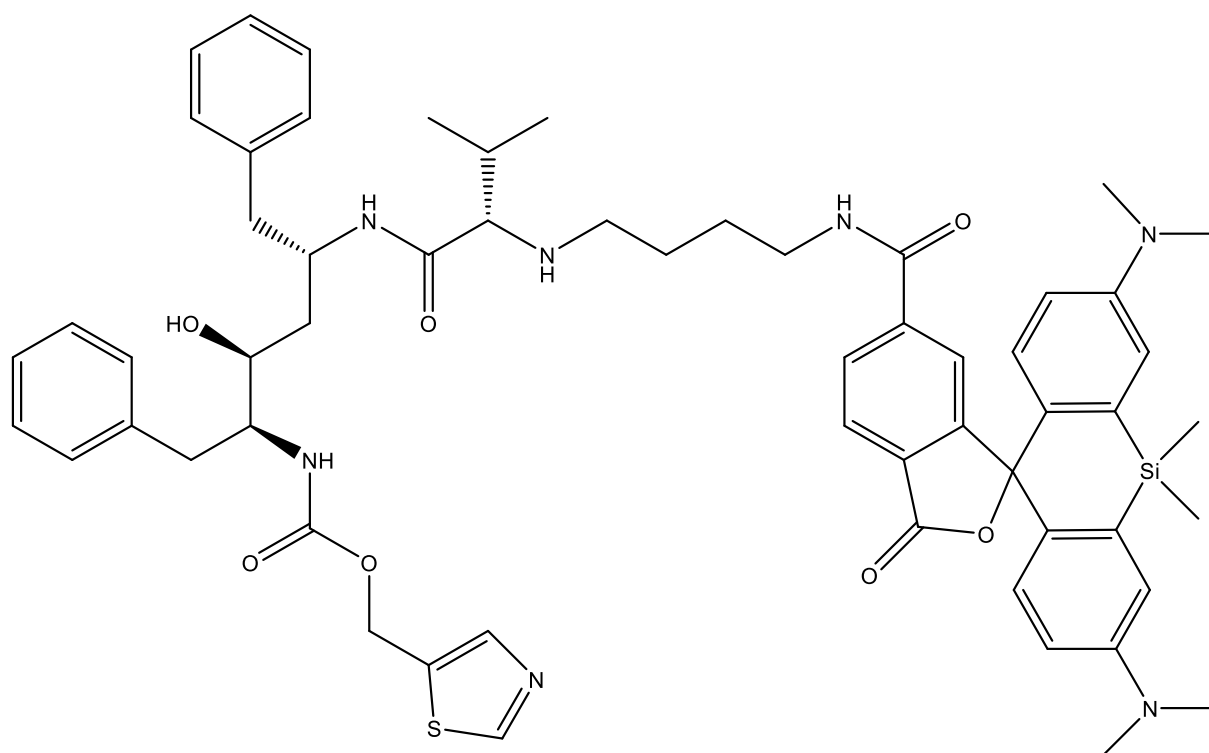
Darunavir



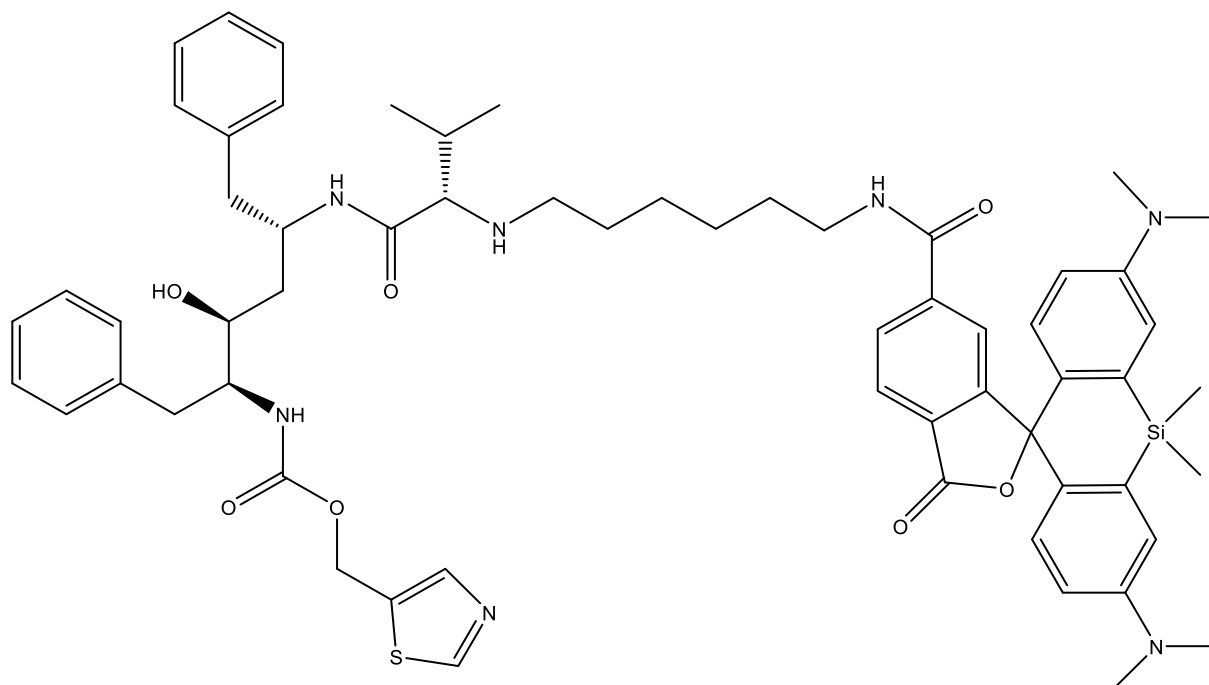
SiR-C2-RTV



SiR-C4-RTV



SiR-C6-RTV



5.1.2.3 Reagent Systems (Kits)

Plasmid Plus Midi Kit	Qiagen, Hilden
NucleoBond MaxiPrep Kit	Macherey-Nagel, Düren
NucleoSpin Gel and PCR purification Kit	Macherey-Nagel, Düren

5.1.2.4 Buffers and Solutions

Acrylamide Stock:	30 % Acrylamide 0.15 % Bisacrylamide
PBS (10x):	142.4 g Na ₂ HPO ₄ · 2H ₂ O 27.6 g NaH ₂ PO ₄ · H ₂ O 819 g NaCl
ddH ₂ O to 10000 ml	
4x Resolving Buffer:	1.5 M Tris (pH 8.8) 0.4 % SDS
4x Stacking Buffer:	0.5 M Tris (pH 6.8) 0.4 % SDS
Running Buffer:	1 g SDS 3.03 g Tris 14.4 g Glycine ddH ₂ O to 1000 ml
Resolving Gel:	17.5 ml Acrylamide Stock 7.5 ml 4x Resolving Buffer 5 ml H ₂ O
3x Sample Buffer:	150 mM Tris HCl, pH 6.8 6 % w/v SDS 30 % Glycerin 0.06 % Bromophenol Blue 10 % β-Mercaptoethanol
Stacking Gel:	15 ml Acrylamide Stock 30:0.8% 25 ml 4x Stacking Buffer 60 ml H ₂ O
Sucrose solution (20 %): dd PBS to 50 ml	10 g Sucrose

TAE Buffer (50x) pH 8.3:	0.1 M EDTA 1 M NaAc 2 M Tris
TBS-T (10x) pH 7.5:	175.32 g NaCl 121.14 g Tris 10 ml Tween dd H ₂ O 2000 ml
Western Blot blocking buffer:	30 % LI-COR buffer (v/v) dd TBS-T
Western Blot Transfer Buffer 1:	0.3 M Tris 20 % Methanol dd H ₂ O 1000 ml
Western Blot Transfer Buffer 2:	0.025 M Tris 20 % Methanol dd H ₂ O 1000 ml

5.1.2.5 Growth Media

5.1.2.5.1 Cell culture media

Adherent cells: Dulbecco's modified Eagle's medium (DMEM) supplemented with 10 % heat-inactivated FCS, and 1 % penicillin/streptomycin.

Suspension cells: Roswell Park Memorial Institute medium (RPMI 1640) supplemented with 10% heat-inactivated FCS, and 1% penicillin/streptomycin.

Imaging medium: Fluoro-Brite supplemented with 10 % FCS (v/v), 4 mM GlutaMAX, 2 mM sodium pyruvate, 20 mM HEPES pH 7.4, 100 U/ml penicillin, 100 µg/ml streptomycin

5.1.2.5.2 Bacterial growth media

LB:
5 g/l NaCl
10 g/l Tryptone
5 g/l Yeast extract

add H₂O and adjust to pH 7.2, autoclave

LB agar plates:
12.5 g/l agar
LB

For selection, Ampicillin (0.1 mg/ml) or Kanamycin (0.1 mg/ml for liquid culture and 0.06 mg/ml for plates) was added to the medium.

5.1.2.6 Nucleic acids

5.1.2.6.1 Oligonucleotides for site-directed mutagenesis

Construct	Inserted Protein	Restriction Enzyme	Direction	5'-3' Sequence
mScarlet.Vpr	mScarlet	AgeI	for	CGCT <u>ACCGGT</u> ATGGTGAGCAAGGGC
		BsrGI	rev	GACTT <u>GTACAG</u> CTCGTCCATGCCG
Clover-mScarlet.Vpr		NaeI	for	AGAG <u>CCGGC</u> GTGAGCAAGGGCGAGGCAG
Clover-mScarlet.Vpr		XhoI	rev	GCCGG <u>CTCTAG</u> TTTGGAG
Clover.Vpr	Clover	AgeI	for	CGCT <u>ACCGGT</u> ATGGTGAGCAAGGGCGAGG
		BsrGI	rev	C <u>GA</u> CTTGTACAGCTCGTCCATGCC
Clover-mScarlet.Vpr		XbaI	for	GCTT <u>CTAGA</u> ATGGTGAGCAAGGGCGAG
MA-eCFP	MA-eCFP	NheI	for	GATATAG <u>CTAGCA</u> TGGGTGCGAGAGCGTCGG
		XhoI	rev	GGTG <u>CTCGAG</u> TCACTTGTACAGCTCGTCCATGCCG

5.1.2.7 Plasmid DNA

Name	Description	Source
mScarlet.Vpr	mScarlet coupled to viral protein r	This work
Clover.Vpr	Clover coupled to viral protein r	This work
Clover-mScarlet.Vpr	Clover linked to mScarlet via PR cleavage site and coupled to viral protein r	This work
sfGFP1-10.Vpr	Clover coupled to viral protein r	This work
pCHIV	pcDNA3.1 derived, non-infectious HIV-1 proviral construct, lacking LTRs and parts of Nef	Lampe et al. (2007)
pCHIV ^{SNAP}	pCHIV derived; SNAP tag inserted in Gag at MA C-terminus with cleavage site between CA	Eckhardt et al. (2011)
pCHIV ^{eGFP}	pCHIV derived; eGFP tag inserted in Gag at MA C-terminus with cleavage site between CA	Lampe et al. (2007)

pCHIV ^{iClip}	pCHIV derived; Clip tag inserted in Gag at MA C-terminus with cleavage site between MA and CA	Hanne et al. (2016)
pCHIV ^{isfGFP11}	pCHIV derived; sfGFP11 tag inserted in Gag at MA C-terminus with cleavage site between MA and CA	This work
pCHIV ^{N-Venus}	pCHIV derived; N-terminal domain of Venus tag inserted in Gag at MA C-terminus with cleavage site between CA	AG Müller
pCHIV ^{C-Venus}	pCHIV derived; C-terminal domain of Venus tag inserted in Gag at MA C-terminus with cleavage site between CA	AG Müller
pCHIV PR D25N	pCHIV derived; D25N active site mutation in PR	Hanne et al. (2016)
pCHIV PR D25N ^{eGFP}	pCHIV derived; eGFP tag inserted in Gag at MA C-terminus with cleavage site between CA and D25N active site mutation in PR	AG Müller
pCHIV Gag only Gag eGFP	pCHIV derived; stop in transframe region Rev-independent full-length gag gene clone fused to EGFP in pEGFP-N	AG Müller Hermida-Matsumoto and Resh (2000)
pCHIV Pol ^{SNAP}	pCHIV derived; SNAP tag inserted in Pol at IN C-terminus	Resh (2000)
pCHIV NC-RT	pCHIV derived; PR cleavage site mutations between NC and RT	This work
pCHIV NC-RT ^{eGFP}	pCHIV derived; PR cleavage site mutations between NC and RT, eGFP tag inserted in Gag at MA C-terminus with cleavage site between CA	This work
pCHIV ^{eCFP}	pCHIV derived; eCFP tag inserted in Gag at MA C-terminus with cleavage site between CA	AG Kräusslich
pCHIV ^{ieCFP}	pCHIV derived; eCFP tag inserted in Gag at MA C-terminus with cleavage site between MA and CA	This work
MA-eCFP	MA coupled to eCFP in pcDNA 3.1 vector	This work
eCFP	eCFP in pcDNA 3.1 mammalian expression vector	Invitrogen

5.1.2.8 Enzymes

GoTaq Hot Start DNA Polymerase	Promega, Madison, USA
Pfu Polymerase	Promega, Madison, USA
Phusion High Fidelity DNA Polymerase	New England Biolabs, Ipswich, USA
Restriction Endonucleases	New England Biolabs, Ipswich, USA
T4 DNA Ligase	New England Biolabs, Ipswich, USA
HIV-1 protease wt	

HIV-1 protease D25N AG Jan Konvalinka, Prague, Czech Republic

AG Jan Konvalinka, Prague, Czech Republic

5.1.2.9 Antibodies and dyes

5.1.2.9.1 Antibodies

Name	Source	Application	Dilution
Sheep anti HIV-1 CA	H.-G. Kräusslich, Heidelberg	WB	1:5000
Rabbit anti HIV-1 MA	H.-G. Kräusslich, Heidelberg	WB	1:3000
Rabbit anti GFP	H.-G. Kräusslich, Heidelberg	WB	1:1000
Rabbit anti Vpr	H.-G. Kräusslich, Heidelberg	WB	1:1000
Secondary antibodies conjugated with IRDye700/800	Rockland, Limerick, USA	WB	1:10000

5.1.2.9.2 Dyes

Name	Source	Application	Dilution
SNAP-Cell® SiR	New England Biolabs, Ipswich, USA	Live-cell imaging	1:1000
SiR-Clip	K. Johnsson, Heidelberg	Live-cell imaging	1:1000

5.1.3 Software

ChemDraw PerkinElmer, Waltham, USA

FACS Diva Software B&D, Becton Dickinson, San José, USA

Fiji Laboratory for Optical and Computational Instrumentation (LOCI), University of Wisconsin-Madison, Madison, USA

i-control™ Software Tecan, Männedorf, Switzerland

Image Lab™ Software	Bio-Rad Laboratories, Hertfordshire, UK
Image Studio™ Lite	LI-COR Bioscience, Lincoln, USA
Imaris 9	Bitplane AG, Zurich, Switzerland
Microsoft Office	Microsoft, Redmond, USA
NIS Elements	Nikon Instruments, Melville, USA
Serial Cloner Software	Serial Basics, France
Snap Gene Viewer	GSL Biotech LLC, Chicago, USA
Pymol	Schrödinger, Japan

5.2 Methods

5.2.1 Biochemical methods

5.2.1.1 SDS-Polyacrylamide Gel Electrophoresis (SDS-PAGE) and Western Blotting

Samples for SDS-PAGE were boiled in protein sample buffer at 95°C for 10min for cell lysates and 5min for particle lysates.

Resolving Gel Preparation: 2.9 ml Acrylamide Stock
1.25 ml Resolving Buffer
0.825 ml H₂O
41 µl APS (10 % w/v)
8.5 µl TEMED

Stacking Gel Preparation: 2 ml Stacking gel mix
50 µl APS (10 % w/v)
5 µl TEMED
20 µl Bromophenol blue

10 µl samples were loaded on a 17.5 % crosslinked polyacrylamide gel and electrophoresis was performed at 25 mA/60cm² gel for 60 min. Subsequently, the proteins were blotted onto nitrocellulose membranes using a semidry blotter with 43 mA/60cm² membrane for 60 min. Membranes were blocked in 30 % LI-COR blocking buffer/TBS-T for a 30 min and were incubated with primary antibodies overnight at 4 °C (dilutions are indicated in 5.1.2.9.1). Subsequently, membranes were washed three times with TBS-T for 15 min and incubated with secondary antibodies conjugated to IRDye700/800 (1:10.000; Rockland, Limerick, USA) in 30 % LI-COR blocking buffer/TBS-T at RT for 1 h. Membranes were washed three times with TBS-T for 15 min and fluorescent signals were detected using a digital infrared scanner (LI-COR, Lincoln, USA). For quantitative signal detection, the Odyssey Image Studio software was used (LI-COR, Lincoln, USA).

5.2.1.2 Spectrofluorometry

Due to the fluorogenic properties of SiR, the characterization of SiR-C6-RTV fluorescence was performed with the Spectrofluorometer FP-8500 (Jasco, Pfungstadt). The following buffers were prepared: 1 mg/ml BSA in PBS, 0.1 % SDS in PBS, PBS and absolute Ethanol; they were filtered with a sterile Rotilabo® filter (0.22 µm pore size) prior to use. For spectrofluorometric analysis, inhibitors were prediluted to 40 µM in DMSO. 200 nM SiR- C2/C4/C6-RTV were analyzed in 150 µl buffer. For the titration, HIV-1 PR or HIV-1 PR D25N were added in 50 nM and 100 nM steps. 1 µM DRV was added for inhibitor displacement. Excitation spectra were recorded at emission 675 nm and excitation ranging from 250-660 nm. Emission spectra were set to excitation at 635 nm and emission to 645-749 nm. Emission and excitation bandwidth were 5 nm, response time 0.5 s and sensitivity was set to high. Data interval was 2 nm with a scan speed of 500 nm/min without auto gain. Light source was a Xenon lamp. For time lapse measurements, excitation was set to 650 nm and emission to 675 nm with a data interval of 1 s for 1 h.

5.2.2 Cell biological methods

5.2.2.1 Cell culture

HEK293T cells are human embryonic kidneys cells transduced with the large T antigen (ATCC). HeLa Kyoto cells were derived from Human papillomavirus-related endocervical adenocarcinoma passaged in a laboratory in Kyoto, Japan.

Adherent cells were cultivated in Dulbecco's Modified Eagle Medium (DMEM) high glucose, supplemented with 10 % FCS and 100 U/ml penicillin and 100 µg/ml streptomycin. Cells were maintained at 37 °C with 5 % CO₂ and 95 % humidity.

Passaging of the cells was performed every 3-4 days. For this, cells were washed with PBS and detached from the glass surface by 0.05% Trypsin/EDTA in PBS. Cells were resuspended in medium and diluted 1:20.

5.2.2.1.1 Transfections

HEK293T cells were transfected with 1 mg/ml polyethylenimine (PEI) 24 h after seeding. Cells were transfected with 3:1 PEI:DNA. Plasmid DNA was added to Roswell Park Memorial Institute Medium (RPMI) 1640 without supplements. PEI was added, the mixture was vortexed and incubated for 30 min, before dripping it gently on the cells. In a 6 well format, 2µg DNA were transfected per well with a 1:1 molar ratio of labeled and unlabeled viral constructs. Vpr constructs were transfected in a 1:10 molar ratio with the viral constructs.

HeLa Kyoto cells were transfected with Fugene HD 24 h after seeding. Transfection agent was added to serum-free RPMI 1640 and incubated for 5 min at RT. The solution was gently mixed with DNA and incubated for another 15 min, before being carefully dropped on cells. In an 8 well labtek format, 50 ng DNA were transfected per well with a 1:1 molar ratio of labeled and

unlabeled viral constructs. Vpr constructs were transfected in a 1:10 molar ratio with the viral constructs.

5.2.2.2 SNAP and Clip stain

600 nM SNAP-Cell 647-SiR or 1 μ M SiR-Clip were incubated with cells for 45 min at 37 °C. For STED measurements, cells were washed with imaging medium for 30 min and imaged subsequently.

5.2.2.3 Staining of cells with fluorogenic PR inhibitor

HeLaK cells were incubated with 1 μ M SiR-C2/C4/C6-RTV in imaging medium 20 min prior to imaging.

5.2.2.4 Flow cytometry

Flow cytometry was used in this study to survey cells expressing the FRET-based sensor in combination with different viral constructs.

Prior to measurement, the cells were prepared as follows: the cells were first harvested and centrifuged for 5 min at 1,500 rpm and 4 °C to remove growth medium. Subsequently, the cells were resuspended in 1 ml PBS and centrifuged again. The supernatant was then removed, and the cells were resuspended in 1 % FCS (in PBS). Finally, the cells were analyzed using the BD FACSCanto HTS flow cytometer. The scattered light caused by the passing cells is then analyzed to give information about the size (forward scatter, FSC) and complexity (sideward scatter, SSC) of the cells and thereby allows distinguishing between dead and living cells and between different cell types. Cells expressing fluorescent proteins were detected by excitation with a blue laser (488 nm) and a red laser (561 nm) depending on the optimal excitation peak of the corresponding fluorophore. Filter sets were also chosen to match best with the optimal emission peak of the corresponding fluorophore.

5.2.2.4.1 FACS-based FRET assay

The proteins to be analyzed were Clover and mScarlet (Lam et al. 2012; Bindels et al. 2017). Clover acts as the donor fluorophore, as it emits light at 515 nm following excitation at 488 nm. The energy is subsequently transferred to mScarlet, the acceptor molecule, leading to the emission of light at 520 nm. While FRET was formerly analyzed by fluorescence microscopy, the FACS-based FRET assay takes advantage of measuring FRET efficiencies by flow cytometry.

To analyze intracellular HIV-1 PR activity by applying the FACS-based FRET assay, HEK293T cells were co-transfected with plasmid DNA encoding the FRET-based sensor in combination with different viral constructs. Following 24 h of incubation, the cells were prepared for flow cytometric analysis (see 5.2.2.4). For each FRET measurement, five different controls were prepared. Cells transfected with pCHIV were used to identify the proportion of viable cells and cells exclusively expressing Clover.Vpr or mScarlet.Vpr were used to exclude false-positive FRET signals. Cells expressing Clover.Vpr and mScarlet.Vpr acted as a negative control, while

cells expressing Clover-mScarlet.Vpr and pCHIV PR D25N acted as a positive control for FRET. Cells expressing Clover-mScarlet.Vpr and pCHIV wt were treated with 5 μ M of LPV, EFV, NNRTI11, NNRTI26 and measured for decrease on FRET⁺ cells. Cells expressing Clover-mScarlet.Vpr and pCHIV dimer PR served as positive control for intracellular PR activity (Kräusslich, 1998). Emitted signals were detected by flow cytometry using the 488 nm laser to excite Clover and the 561 nm laser to excite mScarlet. Clover signals were subsequently detected using a 530/30 filter, while mScarlet signals were detected using a 575/25 filter. To measure FRET signals, the cells were excited with the 488nm laser and the resulting signals were detected using a 575/25 filter.

5.2.3 Molecular biological methods

5.2.3.1 Bacterial transformation and plasmid amplification

For plasmid preparation and cloning, the chemo-competent *E. coli* strain DH5 α was used. For working with retroviral DNA the *E. coli* Stbl2 was used because of its low recombination rates.

Dh5 α : Gibco, genotype: F- 80dlacZM15 (lacZYA-argF) U169 recA1 endA1 hsdR17(rk-, mk+) phoA supE44 - thi-1 gyrA96 relA1 28 5.

Stbl2: Invitrogen, genotype: F- mcrA Δ (mcrBChsdRMSmrr) recA1 endA1 lon gyrA96 thi supE44 relA1 λ - Δ (lac-proAB).

50 μ l of bacteria were thawed on ice and mixed with 100-500 ng of the desired plasmid DNA. The cells were then kept on ice for 10 min to allow the plasmid DNA to attach to the bacterial cell wall. Afterwards, the cells were heat-shocked for 45 s at 42 $^{\circ}$ C. The cells were mixed with 500 μ l LB medium without antibiotics (see 5.1.2.5.2) and then incubated at 37 $^{\circ}$ C for 60 min while shaking at 350 rpm. Afterwards, the bacterial suspension was spread onto agar plates (see 5.1.2.5.2) supplemented with appropriate antibiotics to select bacteria containing the desired plasmid DNA. The agar plates were then incubated at 37 $^{\circ}$ C overnight.

5.2.3.2 Preparation of plasmid DNA from bacterial mini cultures

For small-scale isolations of plasmid DNA from bacterial mini cultures, the alkaline lysis method was conducted as follows: 1 ml of the bacterial mini cultures were cultivated in LB with antibiotics and shaken over night at 37 $^{\circ}$ C. The next day, cultures were centrifuged for 3 min at 13.000 rpm, the supernatant was removed, and the cell pellet was resuspended in 200 μ l buffer S1 (Quiagen, Hilden). To lyse the bacterial cells, 200 μ l of buffer S2 were added and the solution was briefly mixed. Afterwards, 200 μ l of buffer S3 were added to neutralize the solution and the sample was incubated on ice for 5 min. The samples were then centrifuged for 10 min at 13,000 rpm and 4 $^{\circ}$ C. The pellet was subsequently discarded while the supernatant was vigorously mixed with 480 μ l isopropanol to precipitate the DNA. The samples were again centrifuged for 10 min at 13,000 rpm and 4 $^{\circ}$ C and the supernatant was discarded. Next, the DNA pellet was washed with 1 ml 70 % ethanol and the samples were centrifuged for 5 min at 13,000 rpm and 4 $^{\circ}$ C. The supernatant was discarded, and the plasmid DNA pellet

was dried at 55 °C. Finally, the isolated plasmid DNA was resuspended in 30 µl deionized H₂O and digested with HindIII and PstI to control for infectious HIV-1 plasmid DNA (see 5.2.3.5).

5.2.3.3 Gene amplification by polymerase chain reaction (PCR)

In this study, the Q5 DNA Polymerase was used for molecular cloning, as it has proof-reading ability. Specific primers (see 5.1.2.6.1) were used including a short sequence complementary to the template DNA and a restriction site to allow subsequent cleavage of the PCR product by restriction endonucleases. The reaction mix was prepared as follows: 0.5 µl template DNA was mixed with 3 µl 10 mM dNTP mix, 0.75 µl forward primer, 0.75 µl reverse primer, 5 µl 10X Q5 buffer with MgCl₂, 0.25 µl Q5 DNA Polymerase and made up to 50 µl with deionized H₂O. Generally, 35 cycles of amplification were conducted to obtain sufficient amounts of PCR product. The thermal cycling profile is shown.

Step	Temperature	Time	Cycles
Initial denaturation	96 °C	5 min	
Denaturation	96 °C	1 min	30x
Annealing	52 °C	1 min	
Extension	72 °C	1.5 min	
Final Extension	72 °C	10 min	
Storage	4 °C	hold	

5.2.3.4 Agarose gelelectrophoresis

At first, 1 % agarose gels were prepared by dissolving agarose powder in 1xTAE buffer (see 5.1.2.4). 6 µl Midori Green were added to 50 ml agarose solution. After polymerization of the gel, 20 µl control digested plasmid DNA or 50 µl of digested plasmid for ligation and 7µl of a DNA ladder 1 kb Plus were transferred into the sample wells. Electrophoresis was conducted at 90 V for approximately 30-45 min. To visualize the DNA fragments, the agarose gel was exposed to UV light at 254 nm, while DNA was excised from preparative gels under 360 nm illumination.

5.2.3.5 DNA digest and ligation

To enable further processing of particular DNA molecules recovered by gel electrophoresis, the desired DNA was extracted from the agarose gel using the NucleoSpin Gel and PCR Clean-up kit as recommended by the manufacturer. The DNA was finally eluted from the silica filter by adding deionized H₂O. 10 µl deionized H₂O were used to elute smaller DNA fragments like PCR products, while 20 µl were used to elute larger molecules like vector DNA.

Diagnostic restriction digests were conducted by mixing 2 µl 10x Cutsmart buffer, 0.5 µl of each restriction enzyme, 2 µg DNA and deionized H₂O to a total volume of 20 µl. The samples were then incubated for 30 min at 37°C. For molecular cloning, 2 µl of 10x Cutsmart buffer were mixed with 1 µl of each restriction enzyme, 2-10 µl of DNA and deionized H₂O to obtain a total volume of 20µl. 0.5 µl of alkaline phosphatase was additionally added after 5 min to prevent recircularization of the linearized vector DNA that was digested with only one enzyme.

For ligation reactions, 100 ng (determined by Nano Drop) of digested and purified vector was mixed with the digested and purified insert in a 1:3 ratio vector:insert. Subsequently, 2 µl of 10x T4 ligase buffer and 0.1 µl of T4 DNA ligase was added, reactions were filled up with water to 20 µl and incubated over night at 4 °C. 5 µl were used for transformation of bacteria (see 5.2.1).

5.2.4 Cloning procedures

5.2.4.1 Cloning by PCR

Inserts were amplified via PCR as described in 5.2.3.3 with primers listed in 5.1.2.6.1. Following amplification, fragments were purified with the NucleoSpin Gel and PCR Clean-up kit as recommended by the manufacturer. Vectors and PCR products were digested using appropriate restriction enzymes for 2h at 37°C and loaded on a 1% agarose gel. Following running for 30 min at 80V, bands were cut out during brief UV illumination and DNA was extracted from the gel. Gel extraction and the following ligation were performed as described in 5.2.3.5.

5.2.4.2 Subcloning

For construction of pKHIV^{ieCFP}, pKHIV and pNLC-43^{ieCFP} were digested by BssHII and SphI for 2 h at 37 °C, the constructs were loaded on a 1 % agarose gel and run for 30 min with 80 V. After brief UV illumination, the bands were cut out and purified with the NucleoSpin Gel and PCR Clean-up kit as recommended by the manufacturer. Gel extraction and the following ligation were performed as described in 2.2.3.5.

Subcloning of the ieCFP in pCHIV context was performed by digestion of pKHIV^{ieCFP} and pCHIV with AgeI and ClaI for 2h at 37°C. The following steps were conducted as described above.

For the cloning of pCHIV NC-RT, DNA fragment was designed with the following sequence and synthesized by Geneart:

Apal

aaattgca**gggccc**ctagaaaaaggctgttggaatgtggaaggaaggacaccaaataaagat

aat(I)/ggt(G) atc(I)

tgtactgagagacaggct**aat**tttaggaagatctggc**ctc**ccacaaggaaggccaggaattttctcagagcagaccag
agccaacagccccaccagaagagagcttcaggttgggaagagacaacaactccctctcagaagcaggagccgatagac
aaggaactgtatcct

atc(I)/+gct(A)

ttagct**tc**cctcagatcactcttggcagcgaccctcgtcacaataaagataggggggcaattaaaggaagctctattagataca
ggagcagatgatacagattagaagaaatgaattgccaggaagatggaaccaaataatgatagggggaattggaggtttatc
aaagtaagacagtatgatcagatactatagaaatctgcggacataaagctataggtacagattagtaggacctacacctgtca
acataattggaagaa

att(I)/+gct(A)

atctgttgactcagattggctgcactttaaatttccattagtcctattgagactgtaccagtaaaattaaagccaggaatggatggc
 ccaaagttaaacaatggccattgacagaagaaaaataaaaagcattagtagaaattgtacagaaatggaaaaggaagga
 aaaatttcaaaaattgggcctgaaaatccatacaatactccagtatttgcataaagaaaaagacagtactaaatggagaaaa
 ttagtagatttcagag Sbfl

aacttaataagagaactcaagatttctgggaagttcaattaggaataccacatcctgcagggttaaac

Here, all PR cleavage sites between NC and RT were mutated to impair PR autoprocessing. In a first step, pCHIV and the oligo were digested with Apal and Sbfl. The cloning protocol was performed as described above.

pCHIV contains 2 Apal cleavage sites. Therefore, this fragment needed to be inserted after exchanging the NC-RT domain. In a second step, the NC-RT containing viral construct was digested by Apal. Then the Apal fragments of pCHIV and pCHIV eGFP were inserted by a second ligation. This way, pCHIV NC-RT and pCHIV NC-RT eGFP were constructed (see table).

Plasmid number	Vector	Insert	Plasmid name	Antibiotics Resistance
1147	pVpr.eGFP x Agel/BsrGI	PCR Citrine x Agel/BsrGI	pCitrine.vpr	K
1149	pVpr.eGFP x Agel/BsrGI	PCR Clover xAgel/BsrGI	pClover.vpr	K
1182	eGFP.Vpr x Agel/XhoI	PCR CD4 Split GFP 1-10 x Agel/XhoI	Split GFP 1-10. Vpr	K
1183	eGFP.Vpr x Agel/XhoI	PCR CD4 Split GFP 11 x Agel/XhoI	Split GFP 11. Vpr	K
!1209	663 x MluI/XbaI	PCR GFP11 linker MluI/XbaI	pNLC.isfGFP11linker	A
!1210	663 x MluI/XbaI	PCR linker GFP11 MluI/XbaI	pNLC.ilinkersfGFP11	A
!1211	663 x MluI/XbaI	PCR GFP11 MluI/XbaI	pNLC.isfGFP11	A
1286	pKHIV x BssHII SphI	1209 x BssHII SphI	pKHIV.isfGFP11linker	A
1287	pKHIV x BssHII SphI	1210 x BssHII SphI	pKHIV.ilinkersfGFP11	A
1288	pKHIV x BssHII SphI	1211 x BssHII SphI	pKHIV.isfGFP11	A
1292	416 x BssHII SphI	1209 x BssHII SphI	pKHIV.isfGFP11linker (PR-)	A
1293	416 x BssHII SphI	1210 x BssHII SphI	pKHIV.ilinkersfGFP11 (PR-)	A
1294	416 x BssHII SphI	1211 x BssHII SphI	pKHIV.isfGFP11 (PR-)	A
1295	528 x Agel ClaI	1286 x Agel ClaI	pCHIV.isfGFP11linker	A
1296	528 x Agel ClaI	1287 x Agel ClaI	pCHIV.ilinkersfGFP11	A
1297	528 x Agel ClaI	1288 x Agel ClaI	pCHIV.isfGFP11	A
1298	1127 x Agel ClaI	1292 x Agel ClaI	pCHIV.isfGFP11linker (PR-)	A

1299	1127 x AgeI ClaI	1292 x AgeI ClaI	pCHIV.ilinkersfGFP11 (PR-)	A
1300	1127 x AgeI ClaI	1294 x AgeI ClaI	pCHIV.isfGFP11 (PR-)	A
1344	1149x Age/Xho	PCR mScarlet Age/Xho	mScarlet.Vpr	K
1364	pKHIV x BssHII/SphI	1341 x BssHII/SphI	pKHIV iCFP	A
1365	1162 x BsrGI	1345 x BsrGI	Clover-mScarlet.Vpr	K
1370	528xAge/Cla	1364 x Age/Cla	pCHIV iCFP	A
1451			NC-RT Oligo (Geneart)	A
1453	528xApal	1451xApal	pCHIV NC-RT	A
1454	355xApal	1451xApal	pCHIV NC-RT eGFP	A

5.2.5 Virological methods

5.2.5.1 Preparation of virus-like particles (VLPs)

3x10⁷ 293T cells were seeded in a T175 flask 24 h prior to transfection using the PEI method. 70 µg pCHIV or a 1:1 mixture of pCHIV and a fluorescently tagged variant thereof were transfected per flask. Supernatants were harvested app. 40-48 h post transfection, cleared by brief centrifugation at 1500 rpm for 5 min at 4°C and subsequently filtered through 0.45 µm filters. 32 ml of supernatant were layered upon a 6 ml sucrose cushion (20 % sucrose (w/w) in PBS) and pelleted in the ultracentrifuge at 28'000 rpm for 2 h at 4 °C with a SW32 rotor. The pellet was the resuspended in 50 µl of PBS. For smaller preparations, 293T cells were seeded in 6-well plates at 3x10⁵ cells/well transfected with 2 µg DNA and pelleting performed in a table-top ultracentrifuge at 44'000 rpm for 45 min-1 h. The pellet was the resuspended in 20 µl of PBS.

5.2.5.2 SNAP labeling of VLPs

600 nM SNAP-Cell 647-SiR was incubated with VLPs in PBS for 45 min at 37°C. 10 µl VLPs in PBS were attached to an 8 well labtek for 30 min at RT and washed twice with PBS. For imaging, 200 µl PBS were added to each well.

5.2.6 Imaging methods

5.2.6.1 Total internal reflective fluorescence microscopy (TIRF)

TIRF live cell imaging was performed at a Ti2 Microscope (Nikon, Düsseldorf) with an Apo TIRF 60x Oil DIC N2 (NA 1.49) objective and 1.5x zoom. A 488-640 dual filter was used for GFP and SiR measurements. The TIRF angle was adjusted manually. The microscope was equipped with an Andor DU-897 X-11099 EMCCD camera (Andor, Belfast, Ireland). For live-

cell imaging, cells were kept at 37 °C with 5 % CO₂. For timelapse experiments, cells were imaged every 5 s for 2-4 h.

5.2.6.1.1 Förster resonance energy transfer (FRET)

A 405-488-561-640 quadruple filter was used for FRET measurements. DD was detection of Clover signal after excitation with 488 nm, AA measured mScarlet signal with 561nm excitation and DA detected mScarlet fluorescence after 488 nm excitation.

5.2.6.1.2 Fluorescence recovery after photobleaching (FRAP)

The 405-488-561-640 quadruple filter was used for FRAP measurements as well. Here, only DD and AA signals were detected (see 5.2.6.1.1). Then, 561nm laser was increased to 100 % laser power and a region of interest was illuminated for 2 s. Afterwards, DD and AA signals were measured again.

5.2.6.2 Laser scanning confocal microscopy

Confocal imaging was performed with a Leica SP8 TCS DLS microscope (Leica Microsystems, Wetzlar) with a 63x/1.4 HC PL APO CS2 Oil objective with HyD detectors. Imaging settings were 1024x1024 pixels acquired with 400 Hz bidirectional and 5x zoom for particles, 2x zoom for cells. GFP was excited with the Argon laser at 488 nm and detected at emission 496-567 nm, 633 nm with the HeNe laser and emission at 650-750 nm.

5.2.6.2.1 Förster resonance energy transfer (FRET)

Particles were excited with 488 nm and emission detected at 489-550 nm (DD) and 570-631 nm (DA) and 561 nm excitation with the DPSS yellow laser and emission at 570-631 nm (AA).

5.2.6.3 Stimulated emission depletion (STED)

STED imaging was performed at a $\lambda = 775$ nm STED system (Abberior Instruments GmbH, Göttingen, Germany), using a 100 x Olympus UPlanSApo (NA 1.4) oil immersion objective with 590 and 640 nm excitation laser lines at room temperature. Nominal STED laser power was set to ~ 60 % of the maximal power of 1200 mW with 10 ms pixel dwell time and 15 nm pixel size.

5.2.6.4 Fluorescence lifetime imaging microscopy (FLIM)

eCFP lifetime imaging was performed on a home-built setup by the AG Lamb (Munich). Particles and cells were excited with a pulsed $\lambda = 445$ nm laser with 1-2 μ W laser power as measured before the microscope stand. Fluorescence was detected at $\lambda = 479 \pm 40$ nm at an MPD single-photon counting module without prior polarization selection. Laser powers were adjusted with a count rate of about 10-30 kHz at the detector. Single frames were acquired with a pixel size of 60 nm and a total field of view of 30x30 μ m in 5 s. 80 frames were acquired per field of view at at least three different positions per sample. Phasor analysis of lifetime data

was performed by the AG Lamb. For live-cell imaging of late stage cells, 30x30 μm fields were imaged in 5000 ms with 500 lines and 80 frames. For timelapse experiments, cells were imaged with 5 s breaks between frames for 720 frames. Atto425 was used as reference for the phasor plot with a lifetime of $\tau = 3.0$ ns. The focus was set close to the surface and measurements were performed 6 times for 60 s with 5.8 μW laser power.

5.2.7 Image analysis

5.2.7.1 Image processing

Microscopy images were processed with Fiji (Laboratory for Optical and Computational Instrumentation (LOCI), University of Wisconsin-Madison, Madison, USA). Camera offset was measured in an area without cells or particles and subtracted from the whole image. Local background subtraction was carried out with the rolling ball method with varying size of 5-50 pixels. A median filter of 1 pixel was applied to smoothen the signal. A mask was created using the channel with the strongest signal and the particle picker was applied to the mask to detect particles with the size of 4-40 pixels. Signal intensities of the detected particles were exported for the separate channels.

5.2.7.2 FRET analysis

To measure the FRET signal, the separate channels were first multiplied with the mask and then all values were divided by 255 using the Fiji Image calculator. Then, the FRET values were generated by dividing $I(\text{DA})$ by $I(\text{DD})$. The values were exported by applying the detected particles to this image.

5.2.7.3 Acceptor bleaching

The bleached area was cropped and a mask was generated in the GFP channel. Again, the particles were detected, and the signal intensity was measured for the Clover and mScarlet signal pre and post bleaching. The formula applied was: $(I(\text{post})\text{Clover} - I(\text{pre})\text{Clover})/I(\text{post})\text{Clover}$.

5.2.7.4 FRAP analysis

To measure the signal of mScarlet, ROIs were manually drawn on assembly sites and the signal intensity over time was extracted. Recovery was calculated by: $(I(\text{recovery})\text{mScarlet} - I(\text{bleach})\text{mScarlet})/I(\text{pre})\text{mScarlet}$.

5.2.7.5 Co-localization analysis

Mean signal intensities were measured for all detected particles. A signal threshold was set for a positive signal in each channel. % colocalization was determined by positive signal overlap for each particle.

5.2.7.6 Single assembly sites kinetics (Tracking via Imaris)

Newly formed particles at the plasma membrane were tracked with Imaris and signal intensities were grouped for assembly kinetics. The GFP/Clover channel was mostly used for tracking. Diameters of detected punctae at the plasma membrane were measured and set to a maximum of 0.6 μm . Background subtraction was not applied, since background subtracted files as described in 5.2.7.1 were analyzed. Minimal quality was set to detect early events and track duration was set to at least 10 min. Maximum distance between spots was set to 1 μm and 2 gaps were allowed. The signal intensity profiles over time were examined and grouped for exponential, linear, linear endpoint and mess. Exponential and linear endpoint tracks were exported for all channels.

5.2.8 Statistical analysis

Signal intensities were plotted using GraphPad Prism and exponential functions were fitted to the data. This way, the assembly kinetics were determined.

6 Results

6.1 Fluorescence-tagged virus-like particles can be visualized in fluorescence microscopy

The aim of this thesis was the detection of HIV-1 PR activity and active PR during the viral assembly process by fluorescence microscopy. Viral particles were tagged with fluorescent proteins to visualize the assembly process and nascent virus particles. Different targets for fluorescent tags previously identified to be tolerated in viral particle formation and incorporation into the viral particle were applied here: fluorescent proteins were coupled to the accessory protein Vpr, and Gag was tagged in between its MA and CA domains (Müller et al. 2004, McDonald et al. 2002). Various fluorescent proteins based on GFP, mCherry or SNAP (Eckhardt et al. 2011) were explored to establish virus derivatives tailored to the different applications.

Proteins incorporated into particles by coupling them to the viral protein r (Vpr) included mCerulean (Ex: 433 nm; Em: 475 nm), Citrine (Ex: 516 nm; Em: 529 nm), mScarlet (Ex: 569 nm; Em: 594 nm), and Clover (Ex: 505 nm; Em: 515 nm) (Fig. 13A). Alternatively, fluorescent proteins were introduced into the structural polyprotein Gag between MA and CA: eCFP (Ex: 433 nm; Em: 475 nm), eYFP (Ex: 513nm; Em: 527 nm), mCherry (Ex: 587 nm; Em: 610 nm), and eGFP (Ex: 488 nm; Em: 507 nm) (Fig. 13B). Virus particles harboring these fusion proteins were imaged by confocal microscopy. Punctate fluorescent signals corresponding to virus-like particles (VLPs) were detected in all cases. The apparent diameter of approximately 300 nm resulted from the diffraction limit of light microscopy as introduced in 4.3. Microscopic appearance of the samples was comparable for all fluorescently labeled VLPs and independent of the location of the tag. This allowed further tests of the fluorescent tags concerning their applicability for double labeling of VLPs and assembly sites at the plasma membrane.

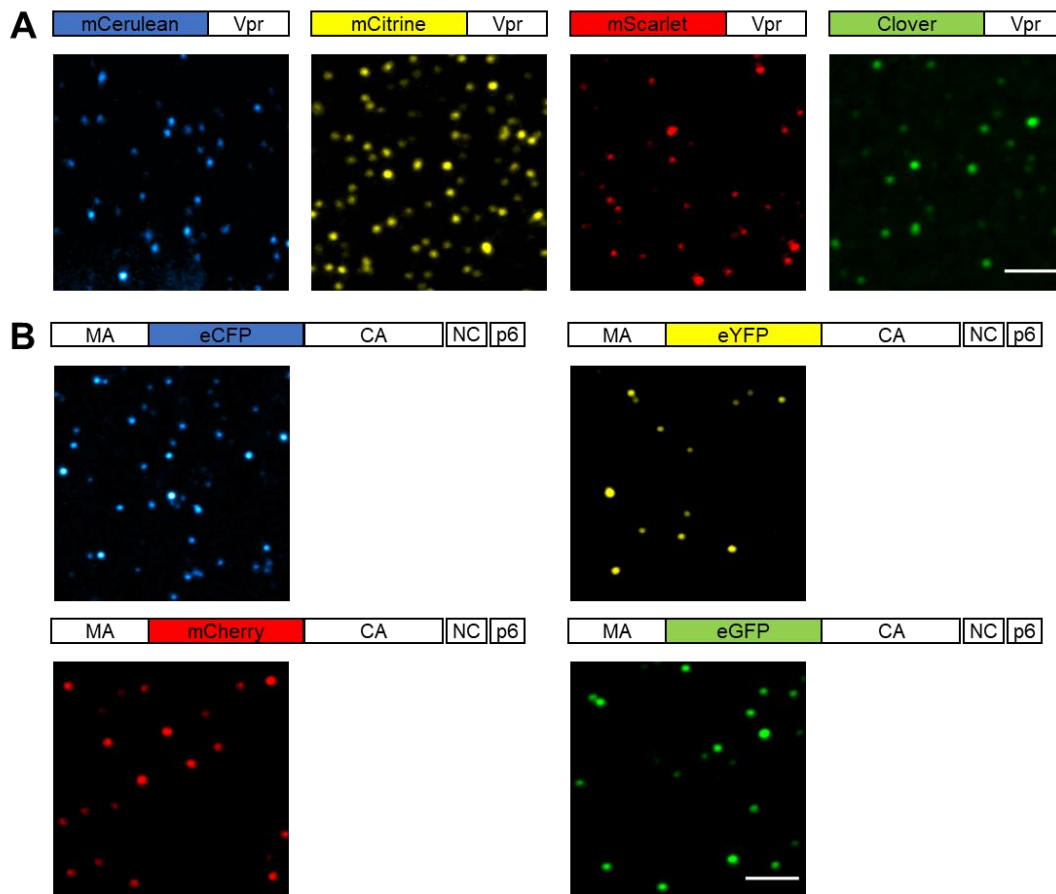


Fig. 13: Virus-like particles can be visualized via incorporated fluorescent proteins. **A:** Schematic model of the indicated fluorescent proteins coupled to Vpr and confocal images of the corresponding purified virus-like particles depicted in pseudocolor LUT. HEK 293T cells were co-transfected with pCHIV wt and pVpr.FP in a 1:10 molar ratio. Supernatant was harvested at 48 hpt and concentrated via ultracentrifugation through a 20% sucrose cushion. VLPs were resuspended in PBS, adhered to an 8-well labtek chamber slide and imaged by LSC. Scale bar 2 μ m. **B:** Schematic model of stated fluorescent proteins in Gag, introduced between the MA and CA domain. Below, confocal images of corresponding purified virus-like particles depicted in pseudocolor LUT. HEK 293T cells were co-transfected with pCHIV wt and pCHIV^{fluorescent protein} in a 1:1 molar ratio. Further sample preparation as described in A. Scale bar 2 μ m.

In order to allow for analyses combining a FRET pair (Clover-Ruby or Citrine-Cerulean) tagged to Vpr with a label within Gag, the panel of fluorescence tags was expanded with the self-labeling SNAP-tag (Reymond et al. 2011). SNAP was inserted in Gag and labeled with SNAP-Cell 647-SiR, a dye emitting in the far-red range (Eckhardt et al. 2011). For co-localization analyses, SNAP-Cell 647-SiR labeled Gag was combined with Clover.Vpr (Fig. 14A) by co-transfection of producer cells. For VLPs purified from the tissue culture supernatant of co-transfected cells, single and double labeled VLPs were detected (Fig. 14B). Double labeled particles and assembly sites at the ventral plasma membrane of HeLa Kyoto cells were identified by co-localization of SNAP-Cell 647-SiR and Clover (Fig. 14B, C, right panel).

Signal co-localization of both tags and established imaging of assembly sites by TIRF microscopy allowed proceeding to live-cell imaging.

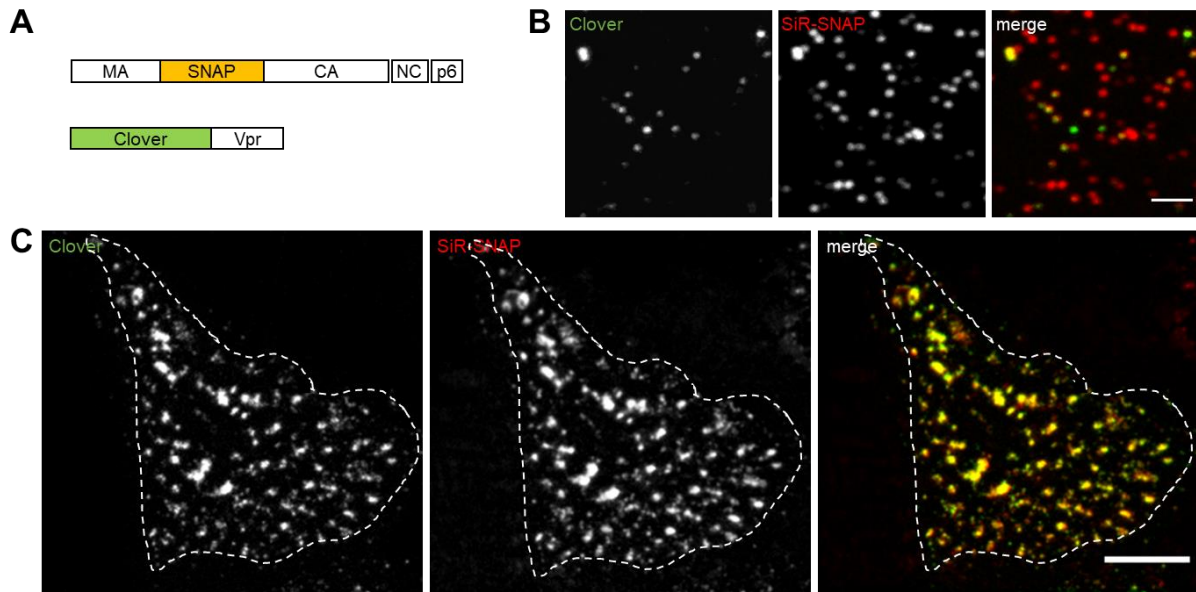


Fig. 14: Double labeling of viral particles and assembly sites. **A:** Schematic model of fluorescent proteins introduced into Gag, inserted between the MA and CA domain or coupled to Vpr. **B:** Confocal images of concentrated virus-like particles carrying Gag.SNAP and Clover.Vpr. HEK 293T cells were co-transfected with pCHIV wt, pCHIV^{SNAP} and pClover.Vpr in a 1:1:10 molar ratio. Supernatants were harvested 48 hpt and concentrated via ultracentrifugation through a 20 % sucrose cushion. VLPs were resuspended in PBS and stained with 600 nM SNAP-Cell 647-SiR for 30 min, followed by adhesion to an 8-well labtek and imaging by LSC. Scale bar 2 μ m. **C:** TIRF images of assembly sites at the ventral plasma membrane. HeLa Kyoto cells were co-transfected with pCHIV wt, pCHIV^{SNAP} and Clover.Vpr in a 1:1:10 molar ratio and 24 hpt stained with 600nM SNAP-Cell 647-SiR for 30 min prior to imaging by TIRF microscopy. Scale bar 10 μ m.

6.2 Live-cell imaging of the viral assembly process

In order to correlate PR activation with the viral assembly process by live cell imaging, I first set out to establish a baseline for analysis of HIV-1 assembly at the plasma membrane using the newly generated virus derivatives. In this study, laser scanning confocal (LSC) and total internal reflection fluorescence (TIRF) microscopy were applied to image fluorescently labeled purified VLPs and assembly sites at the plasma membrane of HeLa Kyoto cells (Fig. 14, 15).

Confocal imaging scans the sample point-by-point with an *xy*-resolution of approximately 200 nm and a *z*-resolution of 500 nm (Fig. 15A, upper panel, Balagopalan et al. 2011). TIRF microscopy is a widefield imaging-based technique, where light is directed towards the sample in a critical angle and therefore reflected at the glass surface. The evanescent wave of the reflected light can penetrate the sample for approximately 200 nm (Fig. 15A, lower panel, Mattheyses et al. 2010), which restricts observation to the ventral plasma membrane and strongly reduces background from intracellular labeled proteins. Here, Gag SNAP expressing pCHIV were labeled live with SNAP-Cell 647-SiR dye added to the cell culture supernatant (Fig. 15B, C).

For purified VLPs adhered to a glass surface, both imaging techniques showed comparable results concerning detection of signal and background (Fig. 15B). For imaging of living cells, the SNAP-Cell 647-SiR dye was present during the measurement, therefore a higher nonspecific background signal was detected in both imaging techniques (Fig. 15C). Viral proteins are expressed in the cytoplasm and assembled at the plasma membrane. For LSC

microscopy, the cytoplasmic signal of Gag SNAP-Cell 647-SiR is too intense to allow the detection of assembly sites at the plasma membrane of HeLa Kyoto cells (Fig. 15C, upper panel).

For TIRF microscopy, the influence of cytoplasmic background was decreased significantly (Fig. 15C, lower panel), so that viral assembly sites at the ventral plasma membrane of HeLa Kyoto cells were clearly visible over the cytoplasmic background. Therefore, TIRF microscopy was applied for live-cell imaging of the viral assembly process. Analysis of fluorescently labeled assembly sites concerning their assembly kinetics was conducted next to validate our system by comparison to published values.

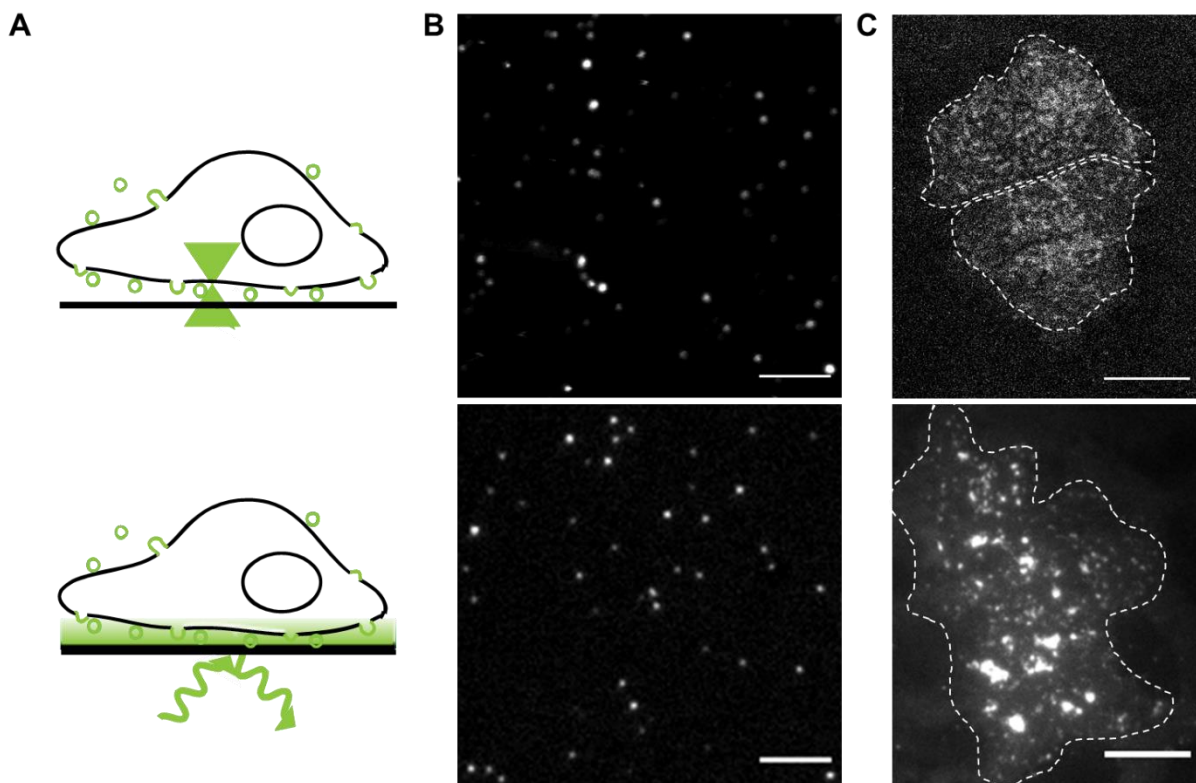


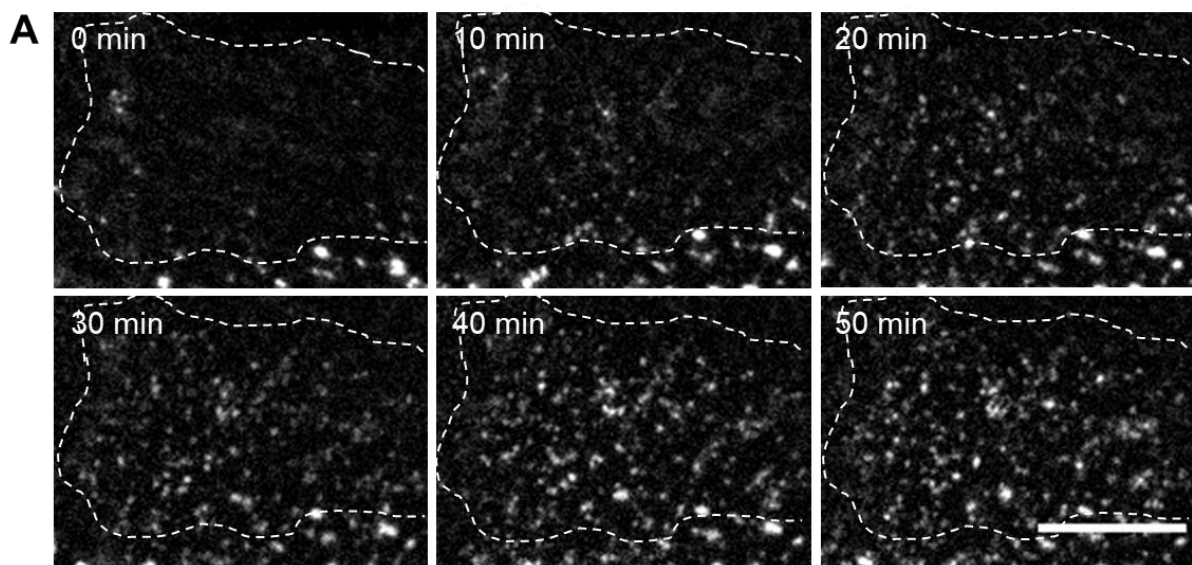
Fig. 15: LSC and TIRF microscopy of SNAP-Cell 647-SiR labeled particles and assembly sites. **A:** Schematic model of confocal (upper panel) and TIRF (lower panel) microscopy sample illumination. **B:** Concentrated virus-like particles imaged by LSC (upper panel) and TIRF (lower panel) microscopy. HEK 293T cells were co-transfected with pCHIV wt and pCHIV^{SNAP} in a 1:1 molar ratio. Supernatant was harvested 48 hpt and concentrated via ultracentrifugation through a 20 % sucrose cushion. VLPs were resuspended in PBS and stained with 600 nM SNAP-Cell 647-SiR for 30 min, followed by adhesion to an 8-well labtek and imaging by LSC. Scale bar 2 μ m. **C:** Assembly sites at the ventral plasma membrane of co-transfected HeLa Kyoto cells imaged by confocal (upper panel) and TIRF (lower panel) microscopy. HeLa Kyoto cells were co-transfected with pCHIV wt and pCHIV^{SNAP} in a 1:1 molar ratio and 24 hpt stained with 600 nM SNAP-Cell 647-SiR for 30 min prior to imaging by TIRF microscopy. Scale bar 10 μ m.

For validation of our live-cell imaging system, HeLa Kyoto cells were transfected with pCHIV expressing fluorescent tags coupled to Vpr or inserted into the structural protein Gag in between the MA and CA domain. Results obtained with the newly generated virus derivatives were compared with published work from our group obtained with pCHIV^{eGFP} using different microscopy setups and a different tracking algorithm (Ivanchenko et al. 2009; Lampe et al.

2007) to verify accuracy of imaging and quantification methods and test for a potential influence of the tags on virus assembly behavior.

Late stage virus-producing cells characterized by large patches of assembled particles at the plasma membrane were employed to adjust the focal plane and the TIRF angle. Laser intensities were optimized to detect early assembly sites and to minimize phototoxicity. Nascent virus-like particles were detected as plasma membrane punctae. Cells showing very few punctae on the plasma membrane, were imaged for 2 h. Over this time period, an increasing number of assembly sites was detected, reaching hundreds of punctae (Fig. 16). Assembly sites were defined by an increase in signal intensity over time due to accumulation of tagged proteins at the site.

Imaging by TIRF microscopy was optimized concerning cell viability and prediction of cells to start the assembly process in the course of this work. Imaging media and laser intensities were varied, and strong cellular Gag expression was identified as signal for subsequent viral assembly. Fig. 16 shows micrographs of exemplary cells expressing HIV^{SNAP} and stained with SNAP-Cell 647-SiR (Fig. 16A) or expressing untagged HIV together with Vpr.Clover (Fig. 16B). The assembly process at the plasma membrane was captured over a time course of 2 h. In accordance with previous studies using HIV^{eGFP} (Ivanchenko et al. 2009), a gradual increase in the number of assembly sites occurred mainly within the first 50-60 min of observation illustrated by the frames displayed in Fig. 16. This period was selected for further analysis.



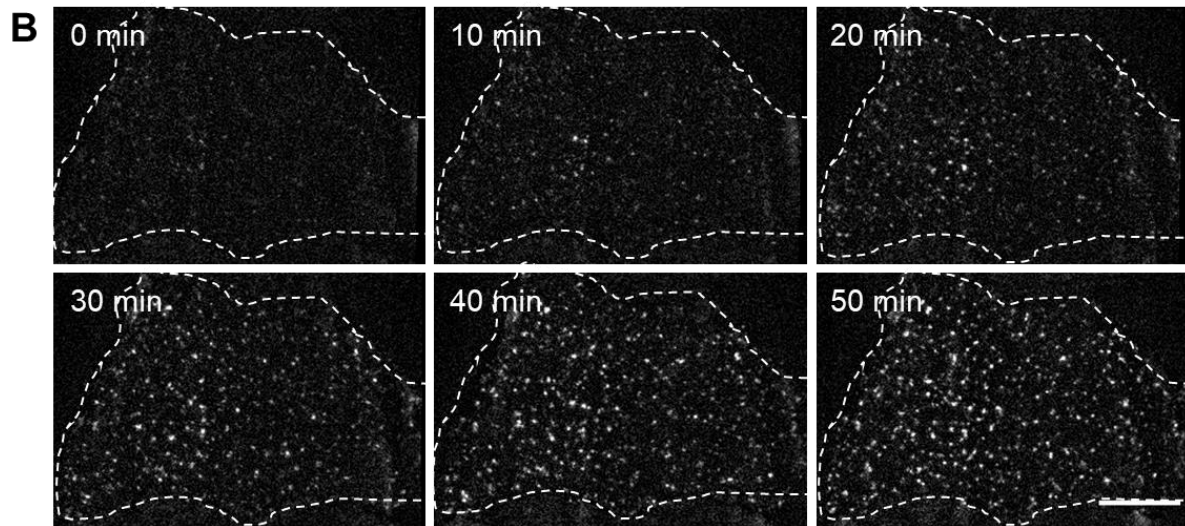


Fig. 16: Live-cell imaging of the assembly process at the plasma membrane of HeLa Kyoto cells by TIRF microscopy. **A:** Time lapse measurement of Gag.SNAP assembly at the plasma membrane of HeLa Kyoto cells. HeLa Kyoto cells were co-transfected with pCHIV wt and pCHIV^{SNAP} and stained at 16 hpt with 600 nM SNAP-Cell 647-SiR 30 min prior to imaging. Cells were imaged every 5 s for 1-2 h. Images show individual frames recorded for a representative cell at the indicated times after the start of the observation. **B:** Live imaging of Clover.Vpr recruitment to the plasma membrane of HeLa Kyoto cells. HeLa Kyoto cells were co-transfected with pCHIV wt and pClover.Vpr in a 1:10 molar ratio. At 16 hpt, cells were imaged every 30 s for 1-2 h. Images show individual frames recorded for a representative cell at the indicated times after the start of the observation. Scale bars: 10 μ m.

Next, the assembly dynamics were analyzed and compared with data published previously for the assembly of HIV^{eGFP} under similar conditions (Ivanchenko et al. 2009). Detection of punctae and analysis of signal intensity of individual punctae over time was performed by tracking with Imaris. Imaris is a commercial software applied here to detect spots and track them over time and was found most robust compared to methods previously applied in this group (Ivanchenko et al. 2009; Rahman et al. 2014). At early time points of observation (< 20-50 min), assembly sites were well separated and could easily be tracked. The continuous formation of new assembly sites resulted in spatial crowding, hampering tracking of punctae at later time points.

In order to determine whether Gag.SNAP (which had not yet been analyzed in live-cell assembly experiments), and Vpr (which is indirectly recruited to the viral assembly site) accumulate at nascent budding sites with similar kinetics than previously observed for Gag.eGFP, I performed quantitative analysis of assembly kinetics. Tracks with a minimum length of 10 min, displaying a clear increase in intensity over time were selected for these analyses. A total of 150 tracks from two independent experiments were averaged, and the mean intensity over time was fitted to a saturating single exponential equation. Fig. 17 shows data obtained for cells expressing HIV^{SNAP} (Fig. 17A) and Clover.Vpr, which is indirectly recruited to viral assembly sites by interaction with the p6 domain of Gag (Fig. 17B). Each signal was normalized to the maximum intensity of the assembly site. For HIV^{SNAP}, a curve fit yielded a rate constant of $0.002935 \pm 0.002041 \text{ s}^{-1}$. This was comparable to assembly kinetics of HIV^{eGFP} ($\sim 5 \cdot 10^{-3} \text{ s}^{-1}$; Ivanchenko et al., 2009). Accumulation of Clover.Vpr at HIV-1 assembly sites occurred with a rate of $0.00608 \pm 0.008681 \text{ s}^{-1}$, slightly faster than the kinetics of labeled Gag.

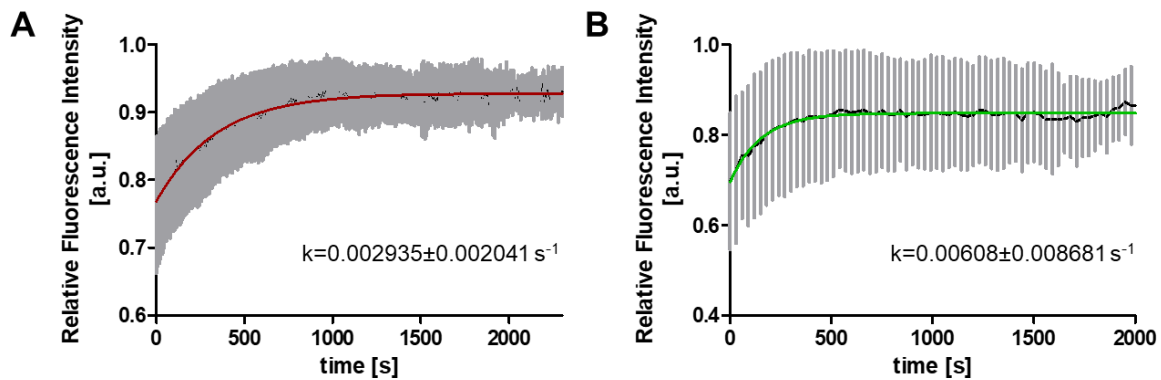


Fig. 17: Assembly kinetics of pCHIV^{SNAP} and pCHIV with pClover.Vpr. **A:** Plot of mean signal intensity over time of assembly sites of pCHIV^{SNAP} transfected HeLa Kyoto cells stained with SNAP-Cell 647-SiR described in Fig. 16A. Mean value and SD of Gag.SNAP fluorescence intensity over time, exhibiting saturating exponential assembly kinetics. $n=50$ assembly sites from 2 cells with exponential fit (red line) and mean rate constant. **B:** Plot of mean signal intensity over time of assembly sites of pCHIV with pClover.Vpr transfected HeLa Kyoto cells depicted in Fig. 16B. Mean value and SD of Clover.Vpr fluorescence intensity over time, exhibiting saturating exponential assembly kinetics. $n=150$ assembly sites from 2 cells with exponential fit (green line) and mean rate constant.

Fluorescent labeling of VLPs and assembly sites was established and allowed visualization of the viral assembly process by live-cell imaging. Virus derivatives used in this work were shown to exhibit assembly kinetics comparable to previously established values. This provided an essential basis for live-cell analysis of viral assembly site formation in parallel to PR activation or activity.

The aim of this project was the detection of HIV-1 protease (PR) activity and active PR during viral assembly. Therefore, different FRET, FLIM and PR-inhibitor-based fluorescence sensors were generated and characterized to assess their applicability for live-cell imaging.

6.3 Design of sensors to detect HIV-1 PR activity during viral assembly

Different sensors were designed to enable detection of proteolytic processing by fluorescent microscopy. They were based on physical characteristics of fluorescent proteins that changed depending on HIV-1 PR. Sensors depict PR activity, so it could be measured despite the resolution limit of fluorescent microscopy. Three different processes were detected: (i) proteolytic processing of an external sensor (ii) Gag processing and (iii) formation of active PR.

6.3.1 An external FRET-based sensor was specifically cleaved by HIV-1 PR

For a FRET-based analysis of PR activity, the autofluorescent proteins Clover and mScarlet were coupled via an HIV-1 PR cleavage site (corresponding to the cleavage site between MA and CA) and linked to Vpr to allow its incorporation into viral particles (Fig. 18A). Proteolytic cleavage of the FRET-based sensor was to detect the enzymatic activity of HIV-1 PR.

Clover acted as the donor fluorophore. In an uncleaved sensor, the energy upon excitation is transferred to mScarlet, the acceptor fluorophore, leading to acceptor signal emission (Lam et al. 2012, Bindels et al. 2017). This is only possible when the spatial distance between the

acceptor and donor fluorophores is small (<10 nm). Upon proteolytic processing, the fluorescent proteins dissociate, and FRET is no longer possible due to the increase in steric distance (Fig. 18A).

To confirm incorporation in the viral particle and HIV-1 PR-specific cleavage of the FRET-based sensor, concentrated VLPs were lysed and detected by immunoblot with antisera against Vpr and CA simultaneously (Fig. 18B).

Endogenous Vpr has a molecular mass of 14 kDa and was detected in all VLPs (Fig. 18B, left panel). As controls, Clover (Fig. 18B, lane 1, donor only) and mScarlet (Fig. 18B, lane 2, acceptor only) were coupled to Vpr separately. Both constructs had a size of 41 kDa. Co-transfection of pClover.Vpr and pmScarlet.Vpr (Fig. 18B, lane 3) served as FRET negative control. In this experiment, lower amounts of VLPs were produced for this sample, causing weaker bands in the western blot (Fig. 18B, left and right panel). All controls and uncleaved sensor (Fig. 18B, lane 4) were packaged into viral particles containing catalytically inactive (D25N) PR. Therefore, no Gag processing was observed (Fig. 18B, lane 6-9). Full-length Gag has size of 55 kDa. Uncleaved sensor was detected at 70 kDa (Fig. 18B, lane 4). An unspecific degradation product of the FRET-based sensor was observed with a size of 35 kDa (marked by *). PR-specific cleavage of the sensor and Gag was observed for the sensor and wild-type pCHIV (Fig. 18B, lane 5, 10). A specific band for the cleaved FRET-based sensor was detected at 42 kDa (Fig. 18B, lane 5), as expected for mScarlet.Vpr, and for CA at 24 kDa (Fig. 18B, lane 10).

Incorporation in the viral particle and HIV-1 PR-specific cleavage of the FRET-based sensor was confirmed by immunoblot analysis. Next, changes in the FRET signal upon proteolytic processing of the sensor was analyzed in purified VLPs by LSC microscopy.

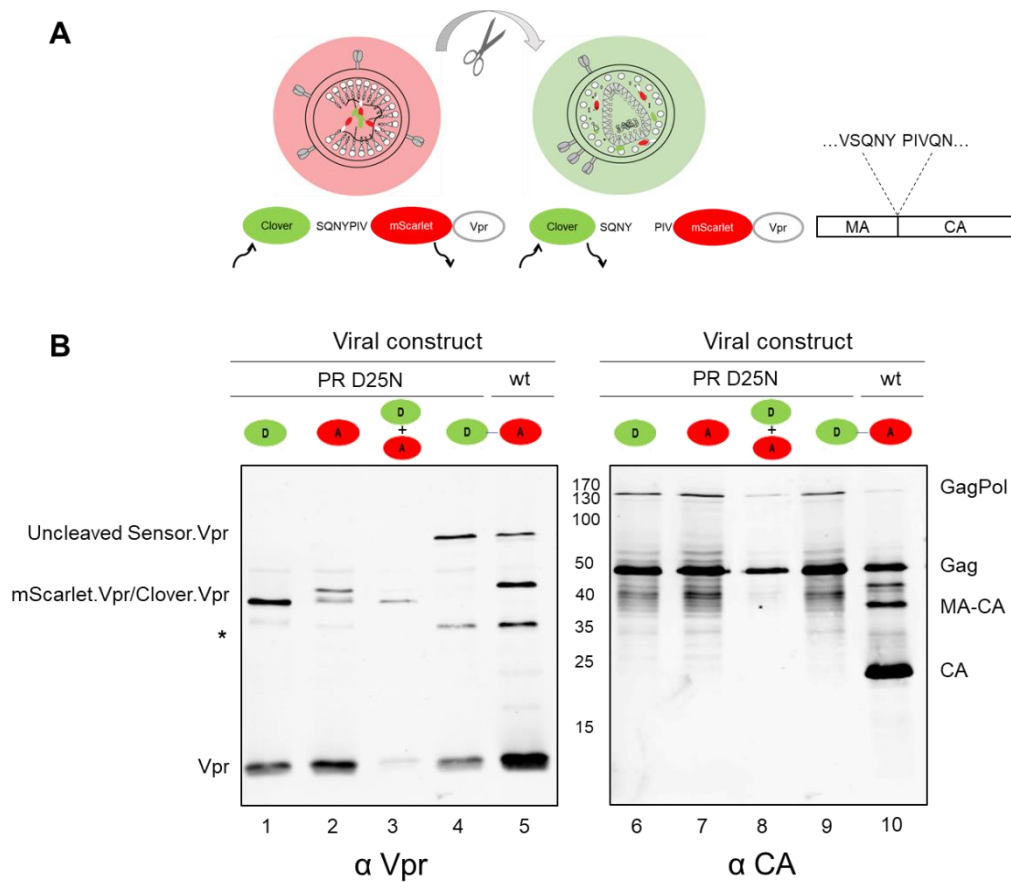


Fig. 18: Sensor incorporation and analysis of PR dependent sensor and Gag cleavage in virus-like particles (VLPs). **A:** Scheme of PR dependent FRET sensor cleavage. Clover and mScarlet are linked by the PR cleavage site found between MA and CA in Gag (right). **B:** 293T cells were co-transfected with pCHIV PR D25N or wt and pFRET-based sensor or control constructs. 48 hpt, supernatants were harvested and concentrated via ultracentrifugation through a 20 % sucrose cushion, followed by immunoblot analysis using antiserum raised against HIV-1 Vpr and CA. D donor, A acceptor, D + A describes co-transfection, D-A depicts the FRET-based sensor. * represents an unspecific degradation product.

To assess the changes in the FRET signal due to proteolytic processing, purified VLPs were analyzed by fluorescence microscopy. Nascent viral particles were previously shown to contain FRET-based sensor cleaved by HIV-1 PR; therefore, a PR-specific FRET signal change would verify the applicability of the sensor for further live-cell imaging analysis. For confocal imaging of VLPs, control and sensor constructs were co-transfected with wild-type and Gag.SNAP pCHIV in a 1:1 ratio (Fig. 19). Gag.SNAP was labeled with SNAP-Cell 647-SiR to identify virus particles. Here, virus particles were verified by the SNAP-Cell 647-SiR signal (Fig. 19A, 5th column).

The first column of Fig. 19A depicts Clover signal after excitation with 488 nm (DD = Donor excitation/Donor emission), the second displays signal of mScarlet fluorescence after 488 nm excitation (DA = Donor excitation/Acceptor emission). In the third column, mScarlet signal was measured with 561 nm excitation (AA = Acceptor excitation/Acceptor emission). FRET images and values were calculated by DA/DD (Fig. 19A, 4th column, B, C). In Fig. 19A, FRET values are depicted by the LUT fire. Low FRET values (0.0) are depicted in blue, high FRET values (1.4) are displayed in yellow. Mean FRET values and SD were calculated analyzing 500 particles per sample (Fig. 19B). The frequency distribution of FRET values of the uncleaved

sensor (D25N PR), was compared with FRET values after PR specific cleavage of the sensor in a wild-type pCHIV (Fig. 19C).

VLPs containing the donor only (Clover.Vpr) were imaged to determine the bleed through of the donor into the DA channel (Fig. 19A, upper row). No unspecific signal was detected in the acceptor channel (AA). A mean FRET value of 0.05 ± 0.023 was calculated for ~ 500 particles, suggesting a weak bleed through of the donor in the DA channel (Fig. 19B). Co-transfection of pClover.Vpr and pmScarlet.Vpr with pCHIV enabled detection of unspecific FRET signal due to molecular crowding of the fluorescent proteins, named FRET negative control. Donor (DD) and acceptor (DA and AA) signals were detected in the particles (Fig. 19A, second row). The mean FRET value increased threefold to 0.14 ± 0.13 in ~ 500 particles (Fig. 19B). The sensor in VLPs containing catalytically inactive PR (D25N mutation at the active site) remained uncleaved and was used to determine the maximum FRET value. Fluorescence signal was detected in all channels (Fig. 19A, 3rd row). Mean FRET values of 0.65 ± 0.31 were calculated in ~ 500 particles (Fig. 19B). The histogram shows a gaussian distribution of FRET values for the particles (Fig. 19C). For the sensor in VLPs containing the wild-type PR, fluorescence signal was detected in all channels as well (Fig. 20A, 4th row). A mean FRET value of 0.32 ± 0.31 was determined (Fig. 19B), which is a 50% lower mean FRET signal compared to catalytically inactive D25N PR. Correspondingly, a clear shift of FRET ratio distribution to low values was detected in the population of VLPs carrying wild-type PR (Fig. 19C). Approximately 80% of the population exhibited FRET values below 0.2.

Analysis of PR-dependent FRET changes in purified VLPs revealed a clear discrimination of cleaved and uncleaved FRET-based sensor. For further analysis, the optimal amount of incorporated sensor concerning proteolytic processing was tested by titration experiments.

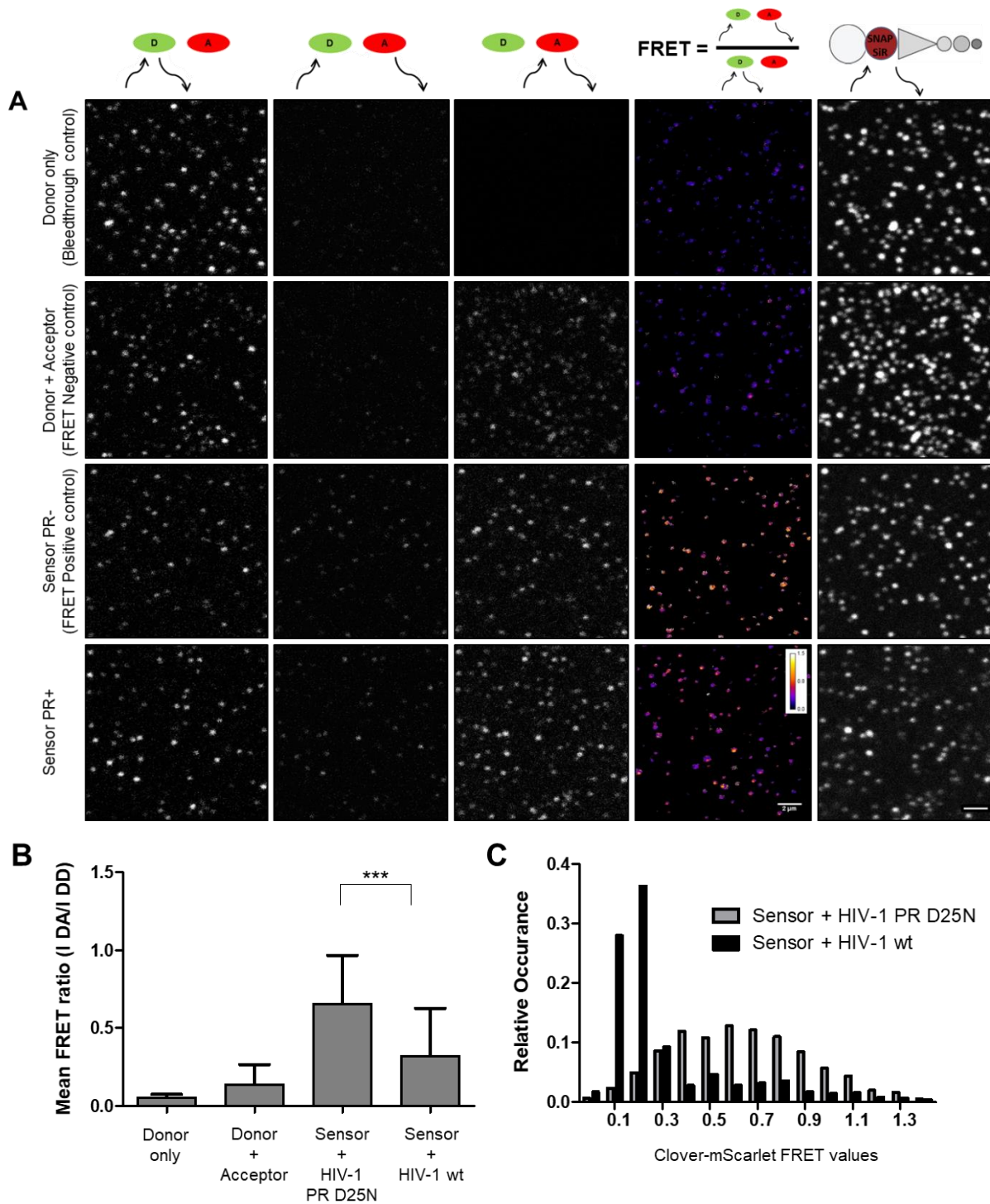
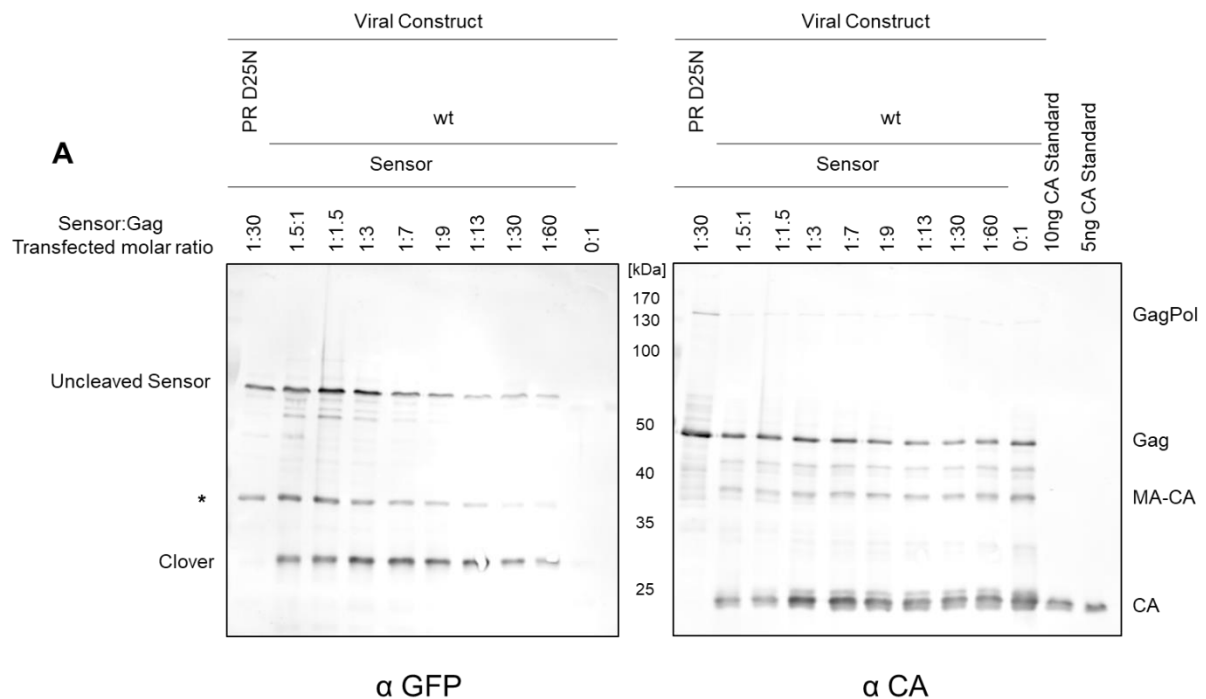


Fig. 19: Analysis of PR dependent FRET signal changes in virus-like particles (VLPs). **A:** 293T cells were co-transfected with pCHIV PR D25N or wt and pCHIV^{SNAP} in a 1:1 ratio and FRET-based sensor or control constructs (1:30 ratio). 48 hpt, supernatants were harvested and concentrated via ultracentrifugation through a 20 % sucrose cushion. Concentrated VLPs were attached to 8-well labtek and imaged by LSC microscopy. Donor signal intensity was measured upon Donor excitation (DD), Acceptor signal intensity was analyzed for Donor (DA) and Acceptor (AA) excitation. FRET values were calculated by dividing signal intensity measured in DA by DD: I(DA)/I(DD). Scale bar 2 μ m. **B:** Quantification of mean FRET values in VLPs. Mean and SD of 500 particles per sample are shown. Statistical analysis via unpaired two-tailed t-test ($p < 0.0001$). **C:** Frequency analysis of mean FRET values of indicated viral particles ($n=500$). I Intensity.

High Vpr amounts in VLPs have been found to impair Gag processing (Lampe et al., 2007). Therefore, amounts of incorporated sensor needed to be controlled for an optimal proteolytic cleavage of sensor and Gag.

Molar ratios of sensor plasmid to pCHIV were titrated in the range of 1:0.66 to 1:60. As a negative control for sensor and Gag processing, the sensor was co-transfected with a pCHIV derivative expressing catalytically inactive PR (D25N mutation at the active site). pCHIV wt was transfected alone as control for optimal Gag cleavage. VLPs were purified from transfected cells, lysed and analyzed by immunoblot with antisera raised against recombinant GFP (reactive against all GFP derivatives, including Clover and eCFP) and HIV-1 CA (Fig. 20A). Specific bands corresponding to Clover and CA were detected in the presence of a virus comprising wild-type PR. Signal intensities of bands representing uncleaved sensor and Clover, or uncleaved Gag derived precursor and CA, respectively, were quantitated to determine the degree of processing (Fig. 20B). Figure 20 B displays the relative degree of cleavage in % for each sample. A maximum relative Gag cleavage of 80% was determined in the absence of sensor. Lower amounts of sensor (up to a molar ratio of 1:9 sensor plasmid to pCHIV) did not affect relative Gag processing; increasing sensor concentrations reduced Gag processing efficiency and resulted in suboptimal sensor cleavage. An optimal sensor cleavage was achieved with a molar ratio of 1:13, while Gag processing was highest for a molar ratio of 1:30. The molar ratio 1:30 was used for all other productions of VLPs (Fig. 18, 19) and further analysis in HEK293T cells. 80% cleavage of the FRET-based sensor was in line with the population size exhibiting FRET values below 0.2 (Fig. 19).

Since HIV-1 specific processing of the FRET-based sensor was confirmed in VLPs, it was next applied to test the influence of various probes on intracellular HIV-1 PR activity.



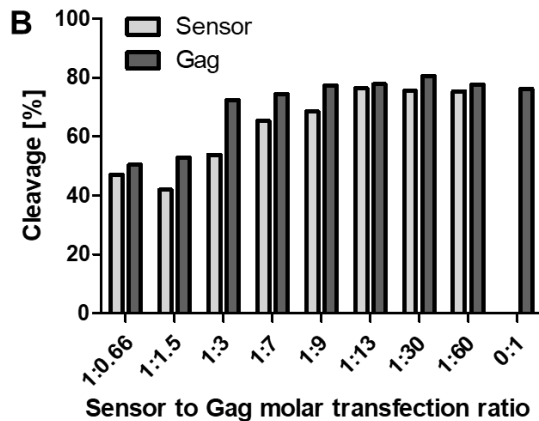


Fig. 20: Effect of sensor plasmid titration on bulk processing efficiency. **A:** 293T cells were co-transfected with the plasmid expressing the FRET-based sensor and pCHIV at the indicated molar ratio. At 48 hpt, supernatants were harvested and concentrated via ultracentrifugation through a 20% sucrose cushion, followed by immunoblot analysis using antiserum raised against GFP and HIV-1 CA. * represents an unspecific degradation product typically observed for proteins comprising red fluorescent proteins. **B:** Quantitation of median signal for sensor and Gag processing products from immunoblots using Image Studio light software.

PR-dependent cleavage of the sensor in cells was observed by flow cytometry to investigate manipulation of intracellular PR activity (Fig. 21). Sensor and control plasmids were co-transfected with pCHIV in HEK293T cells (1:30). Cell harvest and FACS FRET analysis were conducted 24 hpt. The sensor was co-transfected with HIV-1 pCHIV comprising wt PR, PR D25N and a constitutively active PR (dimer PR) (Kräusslich et al. 1998). Unlabeled pCHIV without addition of sensor was used as control. FACS-FRET was employed to detect drug mediated changes in intracellular PR activity – inhibition of proteolytic activity by PR inhibitors, or enhancement of intracellular PR activity by NNRTIs that stabilize the GagPol dimer. Therefore, cells transfected with the sensor plasmid and wild-type pCHIV were additionally treated with the protease inhibitor Lopinavir (LPV, 5 μ M) or non-nucleosidic reverse transcriptase inhibitors (NNRTI) e.g. Efavirenz (EFV, 5 μ M).

Live cells were gated for further analysis of fluorescence intensity (Fig. 21A). Double positive cells were further analyzed for their intensity in the FRET channel (Fig. 21B). Clover only and mScarlet only controls were utilized for laser compensation setting (Fig. 21A). Results from this experiment are summarized in Figure 21 C. When the sensor plasmid was co-transfected with a virus derivative carrying an inactive PR (pCHIV PR D25N), 99,5% FRET positive cells were measured by FACS FRET (Fig. 21C). Weak intracellular PR activity was detected upon co-transfection of pClover-mScarlet.Vpr with wild-type pCHIV. In this case, the FRET positive population decreased to $81 \pm 4\%$ (Fig. 21C). The constitutively active PR decreased the FRET positive population to $28.8 \pm 8.5\%$ (Fig. 21C). These values indicated that the FACS based system can be used to monitor changes in intracellular PR activity. DMSO (inhibitor solvent control) had no influence on PR activity and yielded comparable FRET values to untreated cells expressing wild-type HIV (Fig. 21C). Premature PR activation induced e.g. by EFV decreased the amount of FRET⁺ cells due to intracellular PR activity by $17.5 \pm 9\%$ compared to wild-type (Fig. 21C). LPV rendered the PR inactive (Fig. 21C). Different NNRTIs were tested to determine their effect on intracellular PR activity. NNRTI 11 activated PR strongly, decreasing the FRET positive population to 53.33 ± 4.66 (Fig. 21C). NNRTI 26 did not impact PR activity and was comparable to wild-type values with $79.05 \pm 10.08\%$ FRET positive cells (Fig. 21C). These exemplary results confirmed the suitability of the system for determining the

influence of compounds on PR activity in virus producing cells. Since the central aim of this work was dynamic analysis at individual assembly sites, however, bulk measurements were not further pursued.

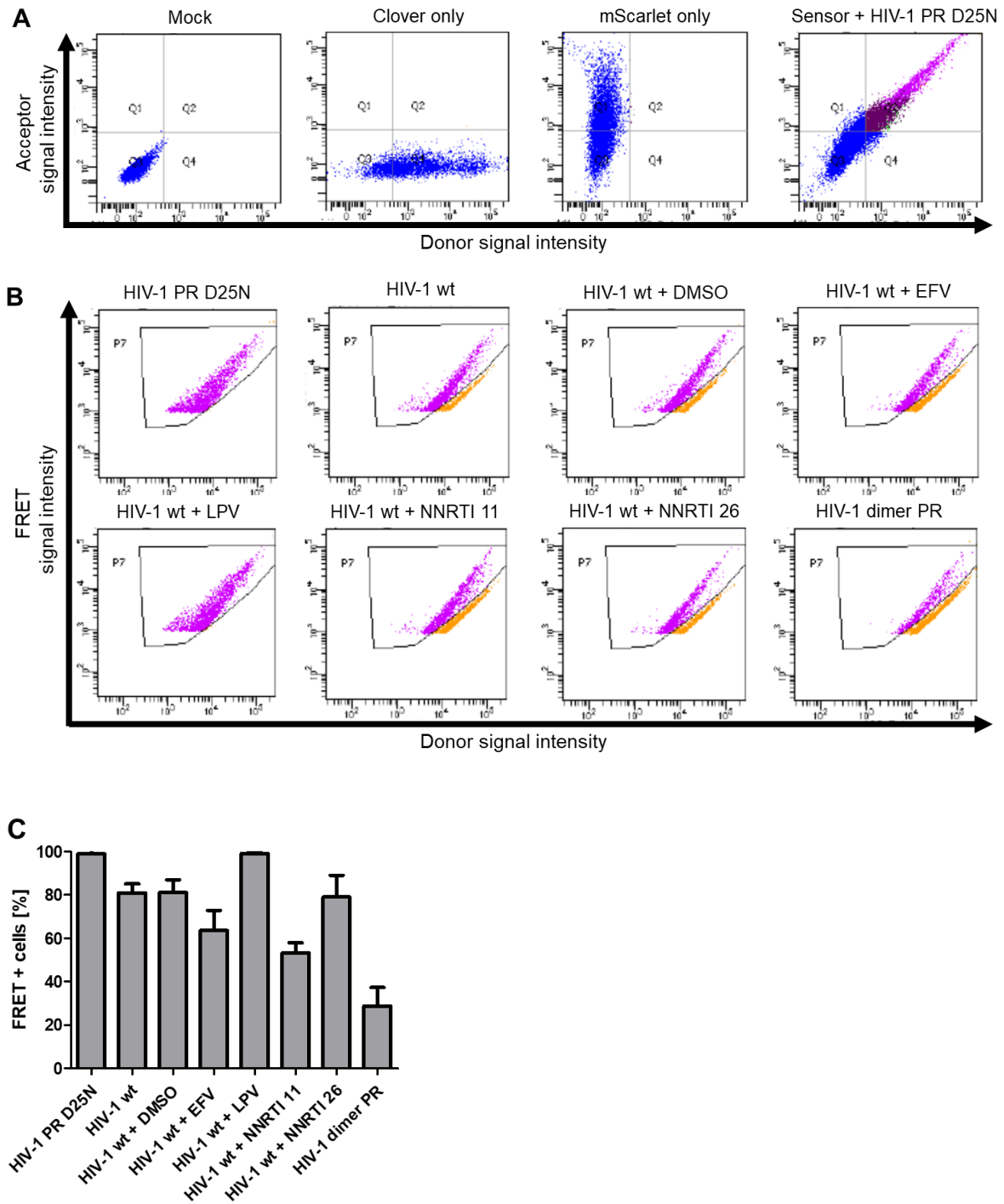


Fig. 21: Quantification of intracellular HIV-1 PR activity by FACS FRET. **A:** HEK293T cells were co-transfected in with the -FRET-based sensor and pCHIV containing wt PR, PR D25N and constitutively active PR. Additionally, HIV-1 wt expressing cells were treated with PR inhibitor LPV, as well as RT inhibitors EFV, NNRTI 11 and NNRTI 26 [all 5 μ M]. 24 hpt, cells were analyzed by flow cytometry. Samples were gated for donor and acceptor double positive populations. **B:** Intracellular donor signal intensity was plotted against FRET signal (DA) to detect shift of population upon proteolytic processing of the sensor. **C:** Quantification of FRET positive cells. Mean and SD from 4 independent experiments.

To validate the FRET potential of the sensor for live-cell imaging by TIRF microscopy, acceptor bleaching experiments were conducted at the HIV-1 budding sites on the plasma membrane of HeLa Kyoto cells (Fig. 22). In an uncleaved sensor, energy is transferred from the donor to the acceptor fluorophore (Fig. 22B). The amount of transferred energy can be determined by quantification of donor signal increase upon acceptor bleaching (Fig. 22B, C). Plasmids pClover.Vpr (donor control) or pClover-mScarlet.Vpr (reporter) were co-transfected with pCHIV encoding either HIV-1 PR D25N or wild-type PR (Fig. 22A). The left panel depicts donor (Fig. 22A, 1st column) and acceptor signal (Fig. 22A, 2nd column) before acceptor bleaching, while the right panel indicates signals recovered after bleaching. The bleached area is marked by a rectangle. The increase in donor signal was quantified by measuring its intensity at the bleached site before and after acceptor bleaching and inserting these values in the equation in Fig. 22C. Clover.Vpr showed an unspecific donor signal increase of $6 \pm 7\%$ (Fig. 22D) upon bleaching. Sensor expressed together with wild-type HIV-1 PR (and thus presumed to be largely processed to Clover and mScarlet.Vpr) displayed a donor signal increase of $8 \pm 7\%$, comparable to the Clover.Vpr control, while donor signal intensity in the uncleaved FRET-based sensor was increased by $27 \pm 13\%$ upon acceptor bleaching. This led to an estimated FRET potential at HIV-1 budding sites of approximately 20 %. This potential allowed a discrimination of changes in the FRET signal by TIRF microscopy and FRET measurements were therefore pursued further.

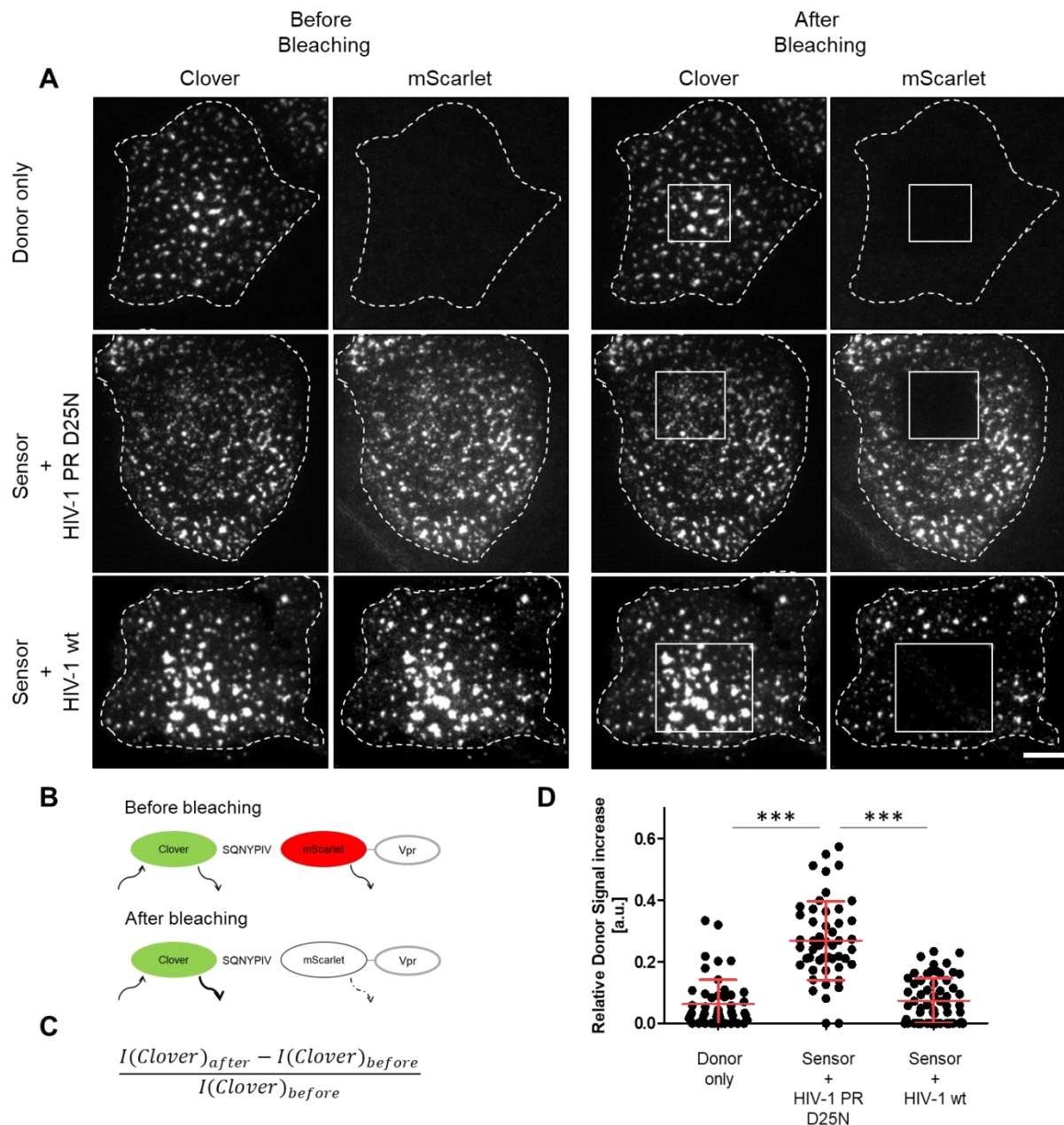


Fig. 22: Maximum FRET efficiency detected by increase of donor signal intensity upon acceptor photobleaching. **A:** HeLa Kyoto cells were co-transfected with pClover.Vpr and pClover-mScarlet.Vpr and pCHIV carrying wt or D25N PR. At 24 hpt, acceptor bleaching was conducted at the plasma membrane with 561 nm laser. Images were detected prior to and directly after bleaching. Scale bar 5 μm . **B:** Scheme of acceptor bleaching technique. **C:** Equation for donor signal quantification. **D:** Quantification of donor signal increase. Mean and SD in red. $n=50$ patches of 5 cells measured in 2 independent experiments. Statistical analysis via unpaired two-tailed t-test ($p<0.0001$).

In the uncleaved sensor, Clover and mScarlet are present in a 1:1 molar ratio. This enabled me to analyze fluorescence signal recovery after photobleaching (FRAP) of the acceptor by using the area of Clover signal as an intramolecular control. In principle, this system could be applied to distinguish between cell associated and released viral particles on the plasma membrane of cells. Released viral particles are incapable of replenishing fluorescent sensor molecules, while assembly sites allow exchange of proteins with the cytoplasmic reservoir and therefore should exhibit fluorescence recovery.

The sensor was co-transfected into HeLa Kyoto cells with a proviral plasmid encoding either wt PR or PR D25N. The acceptor fluorophore mScarlet was bleached, and the signal intensity was measured with a frame rate of 1 min for 30 min (Fig. 23A). Relative fluorescence intensity at the assembly sites was quantified and plotted over time. Fluorescence intensity measured outside the bleached area did not change. Within the bleached region, a very slow gradual increase of mScarlet fluorescence intensity was observed at all previously fluorescent sites, indicating that all spots and patches comprised budded particles as well as particles still connected to the plasma membrane and/or accumulated new assembly sites over the course of the experiment. Fluorescence recovery in this region at 30 min after photobleaching was calculated using the equation shown in Fig. 23C, yielding a total recovery of $14.93 \pm 7 \%$, suggesting that a substantial proportion of particles in the area was already released at the time of bleaching. More precise tracking of individual assembly sites at an early stage of budding site formation should be considered for future experiments.

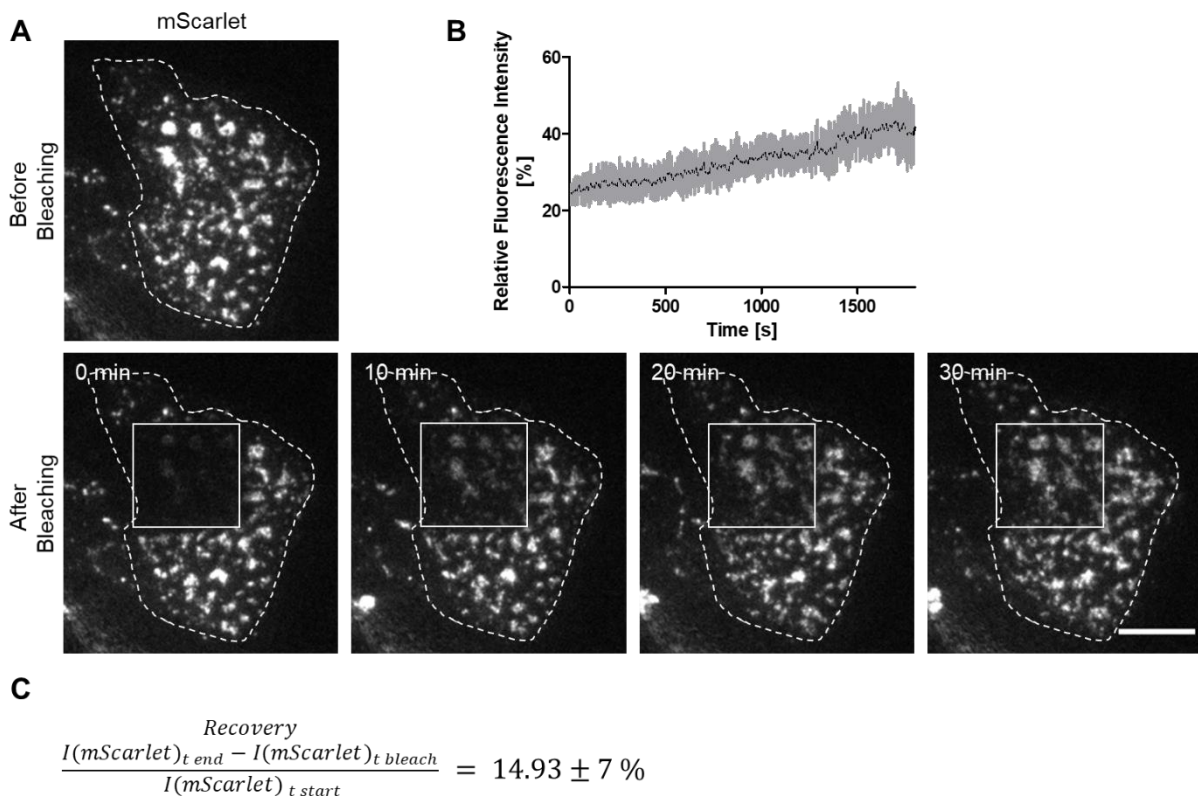


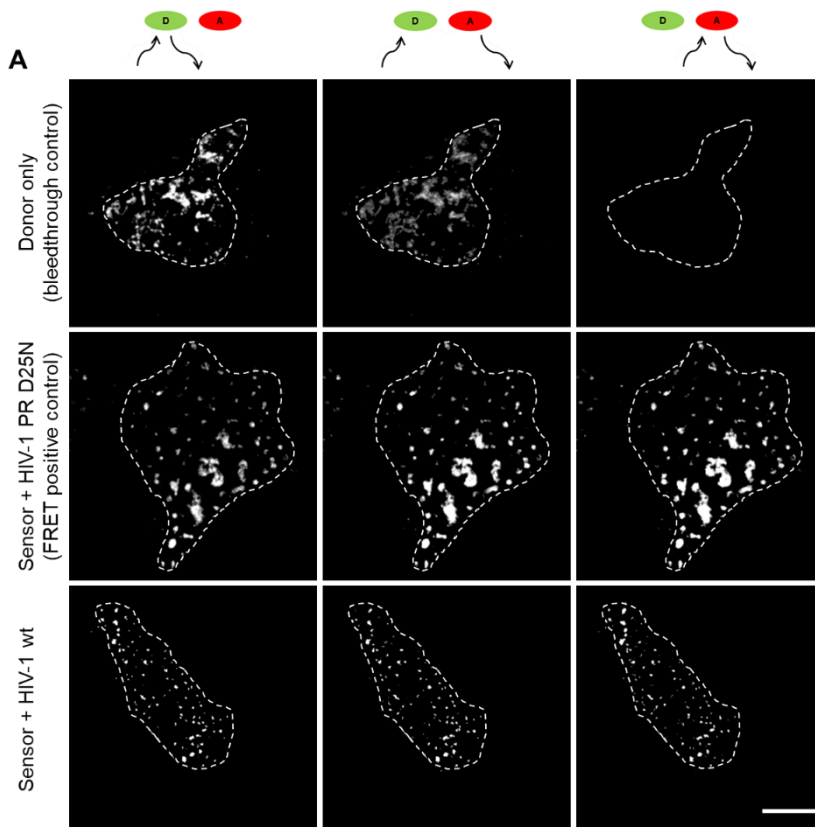
Fig. 23: Fluorescence recovery after photobleaching detected by TIRF microscopy. **A:** HeLa Kyoto cells were co-transfected with clover only and the sensor in the respective pCHIV carrying wt or D25N PR. 24 hpt, acceptor bleaching was conducted at the plasma membrane with 561 nm laser and fluorescence recovery measured at 1 frame/min for 30 min. The figure shows frames recorded at the indicated times after photobleaching. Scale bar 5 μm . **B:** Plot of relative mScarlet fluorescence intensity normalized to signal before bleaching and signal increase after bleaching. Mean in black and SD in gray. **C:** Formula for recovery quantification. Quantification of mScarlet recovery, mean and SD of $n=50$ clusters of 5 cells.

Finally, the applicability of the Clover-mScarlet.Vpr sensor for live-cell imaging was determined by analysis of FRET measurements at the assembly sites of HeLa Kyoto cells by TIRF microscopy. Plasmids expressing Vpr fused to the donor alone or the sensor were co-transfected with pCHIV either expressing HIV-1 PR D25N or wild-type PR into HeLa Kyoto

cells (Fig. 24A). Signal intensities were measured for donor upon donor excitation (DD), acceptor after acceptor excitation (AA) and acceptor after donor excitation (DA). FRET values were calculated by dividing signal intensities of DA by DD (Fig. 24B). The frequency distribution of the calculated FRET values from 4-500 individual sites (area of 4-40 pixels) was analyzed for each sample (Fig. 24C).

Bleed through of the donor into the DA channel yielded a mean FRET value of 0.16 ± 0.04 (Fig. 24B, C, upper panel) comparable to the mean value obtained for purified mature VLPs (Fig. 19). The positive FRET control, i.e. sensor expressed in the presence of HIV-1 PR D25N yielded FRET values of 1.1 ± 0.29 . Analysis of the frequency distribution of intensities indicated two populations (Fig. 24B, C, middle panel). This could depict different FRET efficiencies between cells. Co-expression of the Sensor with HIV-1 encoding wild-type PR yielded a lower FRET value of 0.59 ± 0.19 . Relative occurrence illustrated the shift of the population to lower FRET values, but additionally reveals two populations (Fig. 24B, C, lower panel).

This signal change was expected to be sufficient to detect proteolytic cleavage of the FRET-based sensor during viral assembly. Time-lapse measurements of the assembly process of Clover-mScarlet.Vpr featured assembly kinetics comparable to Clover.Vpr, but no change in FRET signal over time was observed (data not shown). Therefore, additional approaches were conducted to accomplish detection of proteolytic activity during the formation of viral particles.



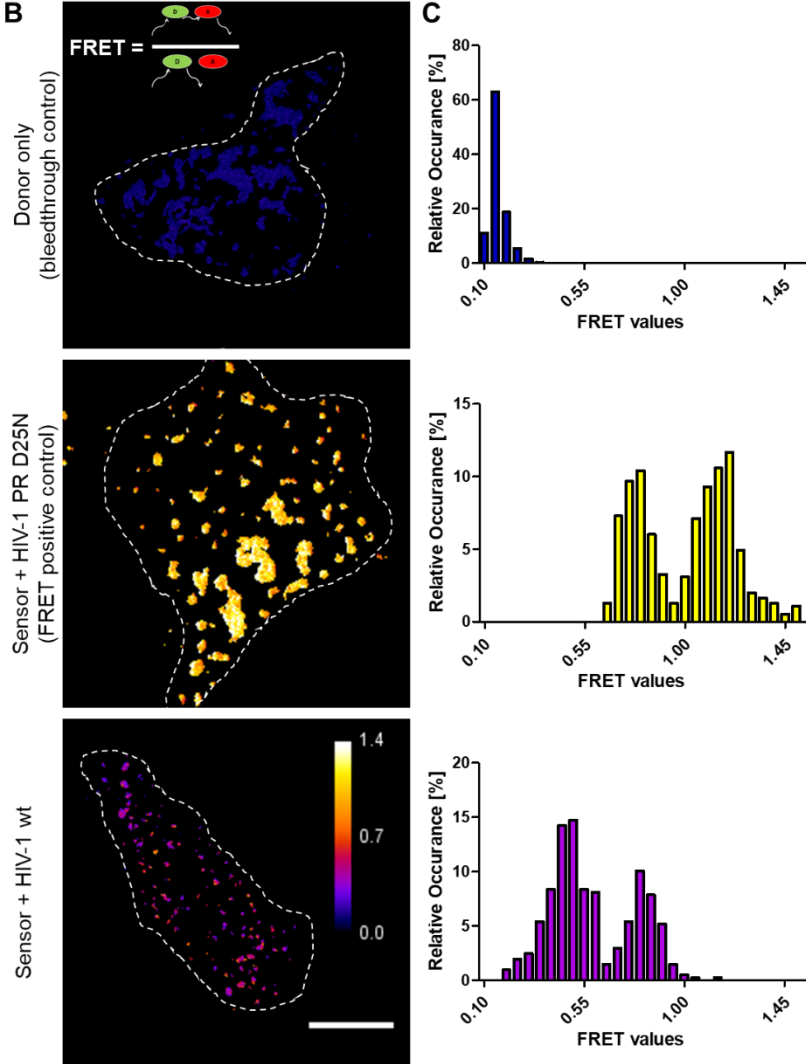


Fig. 24: PR dependent FRET changes detected at HIV-1 Gag assembly sites by TIRF microscopy. A: HeLa Kyoto cells were co-transfected with either Donor only or the sensor with pCHIV expressing wt or D25N HIV-1 PR. 24 hpt, late assemblies at the ventral plasma membrane were imaged by TIRF microscopy. Donor signal intensity was detected after Donor excitation (DD), while Acceptor signal intensity was measured upon Donor (DA) and Acceptor (AA) excitation. B: FRET ratios were calculated by $I(DA)/I(DD)$. Ratio images are depicted with the LUT fire. Scale bar: 1 μ m. C: Histograms depicting the relative frequency of mean FRET values at individual sites (area 4-40 pixels) on the plasma membrane in %. 400-500 clusters from 5 cells were analyzed per condition.

6.3.2 Internal labeling of Gag for detection of Gag processing as a marker for PR activity

Different tags were inserted in Gag to observe Gag processing during viral assembly: (i) split fluorescent proteins, that fluoresce upon proteolytic cleavage of Gag, (ii) a fluorogenic dye that can be applied to super-resolution microscopy and resolve changes in spatial distribution, and (iii) eCFP, that features changes in its fluorescent lifetime depending on localization in the Gag lattice or free diffusion in the viral particle.

6.3.2.1 Split fluorescent proteins and insertion in Gag does not enable distinction of mature and immature VLPs

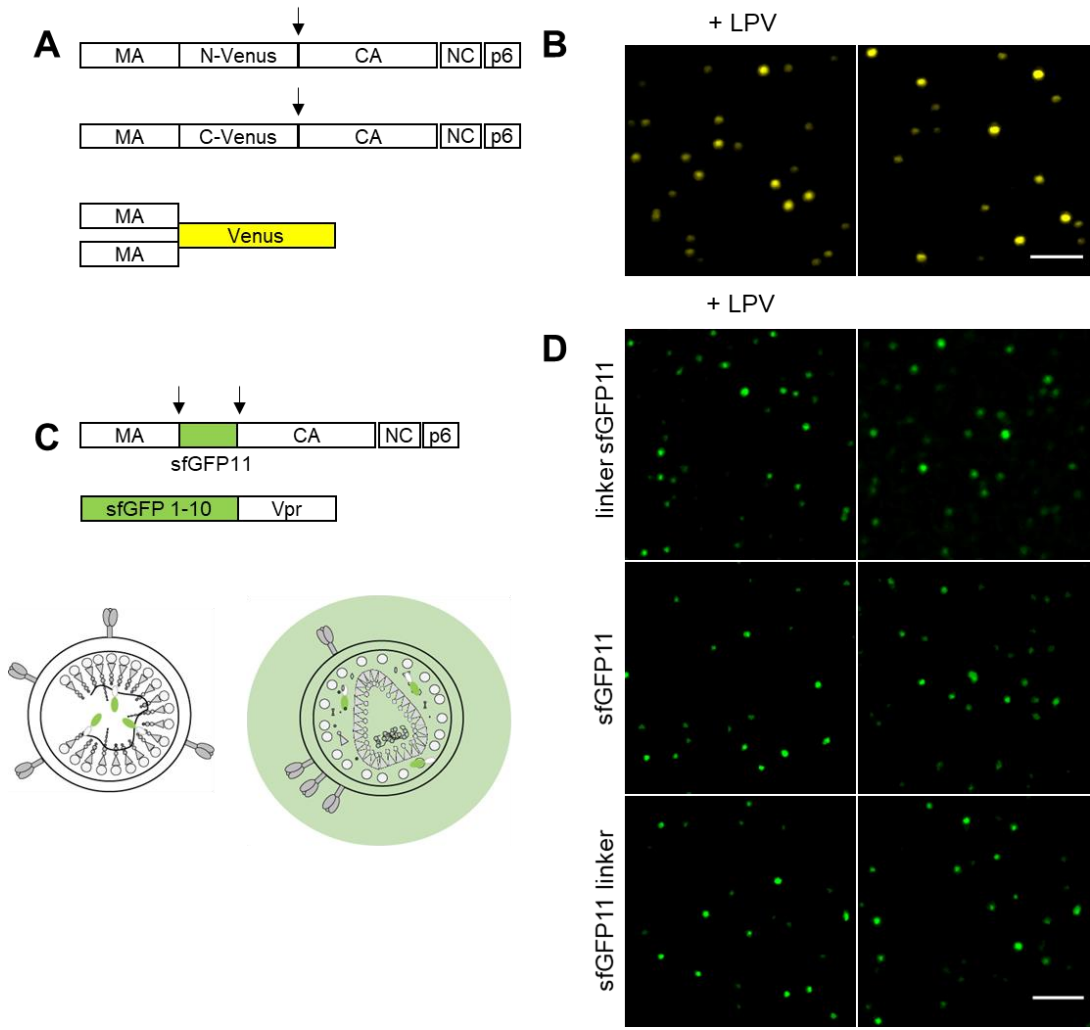
Fluorescent proteins are able to reassemble from its two complementary non-fluorescent fragments, which allows detection of fluorescence signal due to specific protein-protein interactions (Kerppola 2006, 2008). For the purpose of detecting gag processing, non-fluorescent split subdomains of the fluorescent protein Venus (Hernandez und Sandri-Goldin 2011) (Fig. 25A) were separately inserted as internal domains between the MA and CA domain of Gag, with the rationale that constraint induced by the Gag lattice should prevent their association into a complete fluorophore (Fig. 25). Release of the fluorophore subunits by PR mediated processing should enable them to interact and thus result in recovery of fluorescence.

Immature VLPs containing both modified Gag proteins were produced in presence and absence of the HIV-1 PR inhibitor LPV. In contrast to the assumption that fluorescence recovery was prevented by constraining the split domains in an immature lattice, these particles were observed to display strong fluorescence (Fig. 25B). Albeit relative fluorescence signal intensities measured for immature VLPs (20.9 ± 2.9) were somewhat lower than those measured for mature particles produced in the absence of LPV (30.8 ± 5.5) respectively, these data indicated that molecular interactions between moieties contained in Gag could already occur in the unprocessed state (Fig. 25E) indicating high inherent flexibility of the assemblies.

We therefore explored a different positioning of the split subunits, with one moiety expressed as part of Gag and the other attached to the accessory protein Vpr, which is not part of the Gag lattice. Super-folder GFP (sfGFP) was split in subunits $\beta 1-10$ and $\beta 11$, which have been described to reconstitute in the absence of fusion partners mediating their interaction (Cabantous et al. 2005; Cabantous und Waldo 2006). $\beta 11$ was inserted in Gag in between MA and CA flanked by PR cleavage sites (MA-CA) on each site, which should allow free diffusion of $\beta 11$ in the particle after proteolytic processing. Flexible linkers were attached N- or C-terminally of $\beta 11$. $\beta 1-10$ was coupled to Vpr for incorporation in the viral particle by interaction with the C-terminal p6 domain of Gag (Fig. 25C). This approach was based on the assumption that $\beta 1-10$ and $\beta 11$ should not interact in the immature particle due to the location of $\beta 11$ at the N-terminus of Gag in the tight immature lattice and $\beta 1-10$ in the particle interior.

pCHIV expressing $\beta 11$ with or without linkers was co-transfected with p $\beta 1-10$.Vpr in HEK 293T cells grown in the presence or absence of LPV (Fig. 25D). Analysis of mean signal intensity per particle revealed an impact of linkers on the recovered fluorescence signal, with linkers allowing for more efficient reconstitution of the fluorophore (mean intensities in mature articles

of 43.0 ± 9.1 or 37.8 ± 8.2 , as compared to 22.8 ± 1.4 in the absence of linker). However, no significant difference in fluorescence intensity between immature and mature particles was observed for any of the three variants (Fig. 25F). Again, these results indicated that the assemblies produced using these variants did not comprise a regularly packed Gag lattice, providing flexibility for fluorophore interactions even in the absence of processing. The split fluorophore approach was thus deemed unsuitable for the investigation of Gag processing and not further pursued.



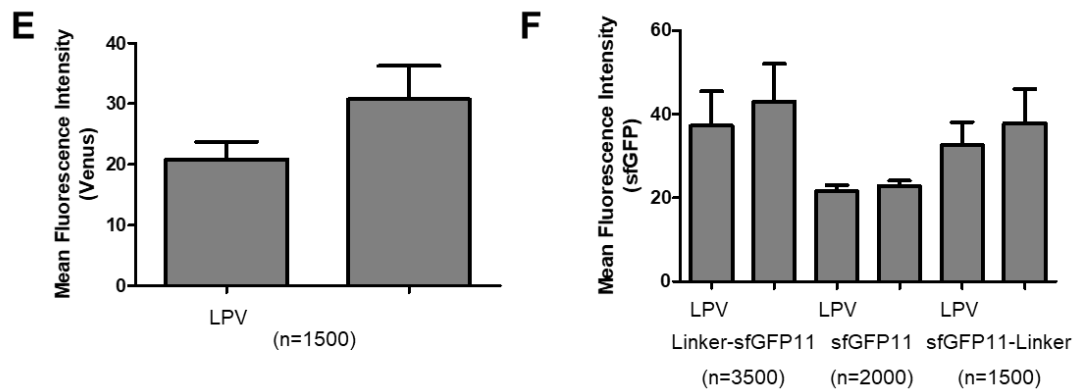


Fig. 25: Maturation of viral particles not detectable with split systems of fluorescent proteins. **A:** Schematic model of Venus split in N- and C-terminal domains. After proteolytic processing of Gag, Venus domains can form the fluorescent protein. **B:** 293T cells were co-transfected with and pCHIV^{C-Venus} and pCHIV^{N-Venus} in a 1:1 ratio together with pCHIV wt (1:1:2 molecular ratio) in duplicates. 1 sample was treated with 2 μ m LPV. 48 hpt, supernatants were harvested and concentrated via ultracentrifugation through a 20% sucrose cushion. Concentrated VLPs were attached to 8-well labtek and imaged by LSC microscopy. Confocal images of corresponding purified VLPs depicted in pseudocolor LUT. Scale bar 2 μ m. **C:** Schematic model of split sfGFP system. sfGFP11 is inserted between MA and CA, while sfGFP1-10 is coupled to Vpr for incorporation. Only freely diffusing sfGFP11 upon proteolytic processing can form a fluorescence sfGFP. **D:** 293T cells were co-transfected with and pCHIV^{sfGFP11} and pCHIV wt in a 1:1 ratio together with sfGFP1-10.Vpr (1:10 molecular ratio) in duplicates. 1 sample was treated with 2 μ m LPV. 48 hpt, supernatants were harvested and concentrated via ultracentrifugation through a 20% sucrose cushion. Concentrated VLPs were attached to 8-well labtek and imaged by LSC microscopy. Confocal images of corresponding purified virus-like particles depicted in pseudocolor LUT. Scale bar 2 μ m. **E:** Quantification of mean fluorescence intensity of Venus signal per VLP \pm LPV. Mean and SD of 1500 particles. **F:** Quantification of mean fluorescence intensity of sfGFP signal per VLP \pm LPV with different locations of a flexible linker on sfGFP11. Mean and SD of stated number of particles.

6.3.2.2 Changes in localization of fluorescence tags in Gag can be visualized by STED microscopy

For the reasons outlined above, all measurements were performed using TRIF microscopy, visualizing particles accumulating at the ventral membrane of the cell and the glass coverslip over a time period of 1-2 h after onset of assembly site formation. The morphology of particles formed under these conditions has never been analyzed. In order to investigate whether proteolytic processing does occur under these conditions, I made use of the observation of Hanne et al. (2016) that the resolution of STED super-resolution microscopy allows for discrimination of immature and mature HIV-1 particles. The high laser power of the STED laser beam results in rapid photobleaching and phototoxicity, which prevents application of this approach to live-cell analyses of maturation. However, it should be suitable to investigate the maturation status of cell-associated particles in still images.

Hanne et al. had used HIV-1 derivatives carrying a SNAP-tag or the closely related Clip-tag (Reymond et al. 2011) flanked by two PR cleavage sites (Figure 26A). Expression of the virus in the presence or absence of the PR inhibitor LPV yielded immature or mature particles, respectively. Characterization of purified particles stained with SiR-SNAP or SiR-Clip, respectively, by STED nanoscopy revealed a ring-like pattern for immature virions, in which the stained tag was present as part of the semi-spherical immature Gag shell. Proteolysis of the polyprotein should result in random distribution of the released tag within the virion. Accordingly, mature particles were indeed found to display a 'blob' or spot-like morphology (Hanne et al. 2016).

I wanted to make use of this system established for isolated particles, applying it to the analysis of assembly sites at the ventral membrane of virus expressing cells.

First assessment of pCHIV^{iClip} was conducted in purified VLPs as described by Hanne et al., 2016 to validate the system. Immature VLPs were produced in the presence of LPV, wild-type particles without additives. Images were acquired using an Abberior STED microscope in diffraction limited (confocal) and STED mode (Fig. 26B). In confocal microscopy, immature (+LPV) and mature (-LPV) samples were both detected as spots (Fig. 26B, left column). STED microscopy revealed a ring structure for immature VLPs imaged in the focal plane (Fig. 26B, upper row, middle and right column). Wild-type VLPs depicted a few rings, but mostly blob structures (Fig. 26B, lower row, middle and right column). Line profiles were analyzed to compare full width half maximum (FWHM) values of immature (Fig. 26D) and mature (Fig. 26E) particles measured for confocal and STED microscopy. For confocal microscopy, FWHM of 261 ± 31 nm was quantified for mature and 250 ± 16 nm for immature VLPs (Fig. 26C). Immature ring structures imaged by STED microscopy revealed the distance of the peaks depicted in Fig. 27D of 109 ± 28 nm, while blobs were measured to have a FWHM of 74 ± 14 nm.

Since these results were in line with the published data (Hanne et al. 2016). pCHIV^{iClip} could now be applied for visualization of mature and immature viral structures at the plasma membrane of HeLa Kyoto cells.

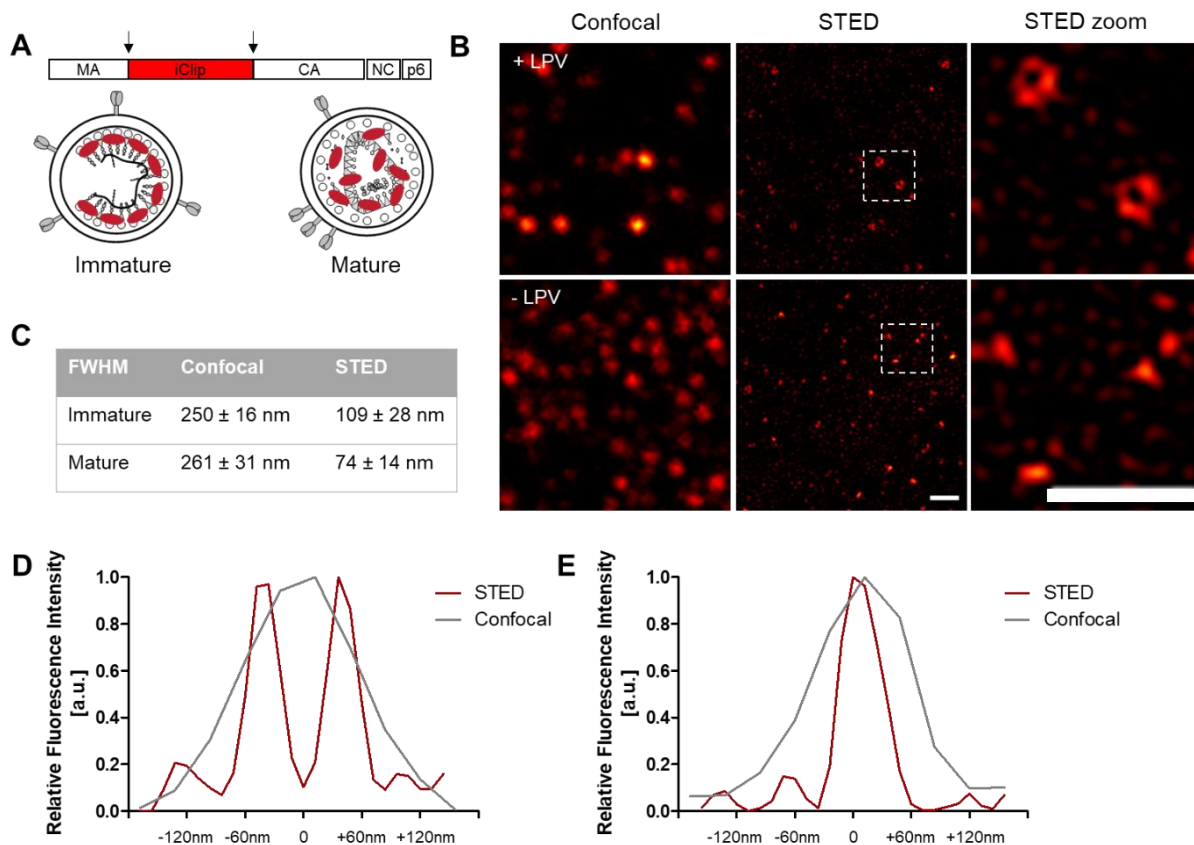


Fig. 26: Discrimination of mature and immature virus-like particles by STED microscopy. **A:** Schematic model of Clip tag inserted between the MA and CA domain in Gag, flanked by PR cleavage sites. In an uncleaved state, it is part of Gag and can be observed as ring-like structure. After proteolytic processing, it freely diffuses in the particle and is detected as a blob. **B:** Confocal and STED images of immature (+LPV) and mature (-LPV) purified VLPs stained with SiR-Clip and zoom of STED image. HEK 293T cells were co-transfected with pCHIV^{iClip} and pCHIV wt in a 1:1 molar ratio and either untreated or treated with 2 μ m LPV. Supernatant was harvested 48 hpt and concentrated via ultracentrifugation through a 20 % sucrose cushion. VLPs were resuspended in PBS and stained with 1 μ m SiR-Clip for 45 min at 37°C, followed by adhesion to an 8-well labtek II and imaging by STED microscopy.

Scale bar 0.5 μm . **C**: Measured diameter of viral particle by taking the peak width at half maximum of the line profile for confocal images and the blob, and by measuring the peak distance of the ring structure. **D**: Line profile of immature VLP (+LPV) with confocal and STED measurement. **E**: Line profile of mature VLP (-LPV) with confocal and STED measurement.

Live-cell imaging of the pCHIV^{iClip} stained with SiR-Clip was conducted at the plasma membrane of HeLa Kyoto cells grown in presence or absence of LPV for imaging of immature and mature released viral particles and assembly sites (Fig. 27, 28). Due to the confined space between the plasma membrane and the glass surface, released viral particles remained trapped and could therefore not be distinguished from assembly sites. In confocal microscopy, viral particles could not be resolved at this point (Fig. 27B). As we zoomed in on the plasma membrane with STED microscopy, we observed the whole plasma membrane covered by assembly sites and what appeared to be piles of released particles trapped underneath the cell (Fig. 27B). Cells grown in the presence of LPV displayed exclusively ring-like structures (Fig. 27A, C, upper panel). In contrast, both ring- and 'blob'-like structures were observed for untreated cells, indicating that processing does occur. featured ring- and blob-like structures (Fig. 27A, C, lower panel). The high density of structures prevented detailed analysis, however. These findings clearly show that late stages of virus production are unsuitable for live-cell microscopy and patches have to be excluded from tracking analyses.

Earlier time points of viral assembly were analyzed by imaging of cells displaying fewer particles on the plasma membrane. This might pinpoint the timing of Gag processing in relation to the state of assembly.

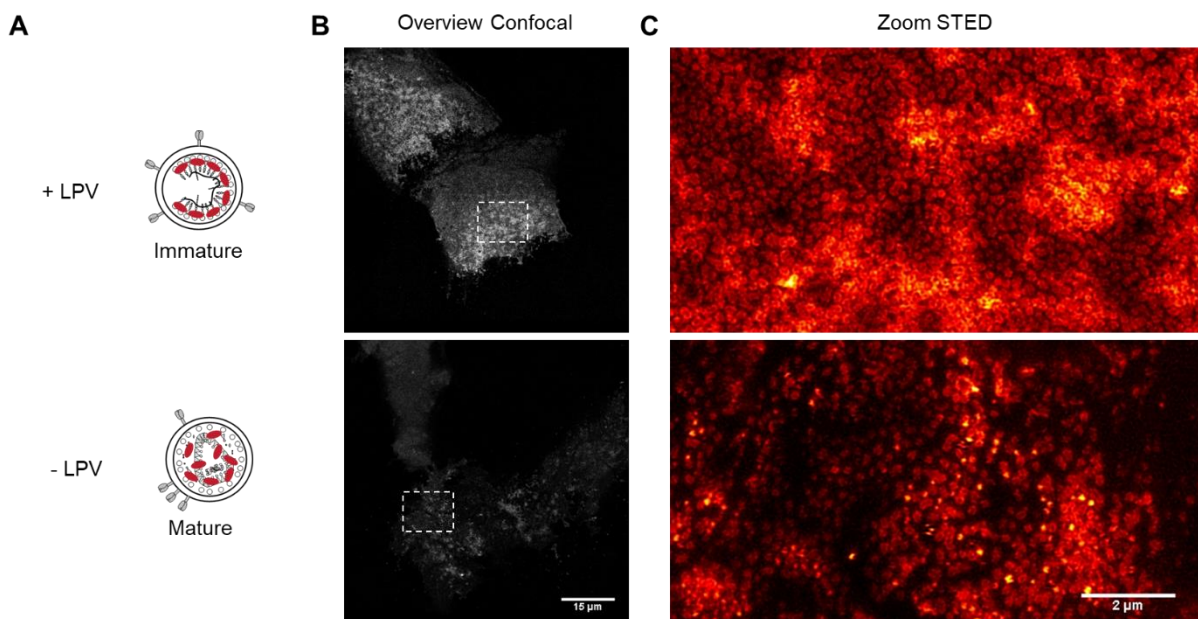


Fig. 27: Virus-like particles \pm LPV assemble at the plasma membrane of HeLa Kyoto cells. **A**: Schematic model of Clip tag inserted between MA and CA in Gag, flanked by PR cleavage sites. In an uncleaved state, it is part of Gag and can be observed as ring-like structure. In the processed state, it freely diffuses in the particle and is detected as a 'blob'. **B**: Confocal image of assembly sites and trapped particles at the plasma membrane of HeLa Kyoto cells stained with SiR-Clip. HeLa Kyoto cells were co-transfected with pCHIV^{iClip} and pCHIV wt in a 1:1 molar ratio and either untreated or treated with 2 μm LPV. 24 hpt, cells were stained with 1 μm SiR-Clip for 45 min at 37°C and washed for 30 min prior to imaging by STED microscopy. Scale bar 15 μm . **C**: Zoom of assembly sites and trapped particles stained with SiR-Clip detected by STED microscopy. Scale bar 2 μm .

Live-cell imaging of the pCHIV^{iClip} stained with SiR-Clip was conducted at the plasma membrane of HeLa Kyoto cells in presence of LPV for imaging of immature released viral particles and assembly sites (Fig. 28). Here, GagiClip is a component of the Gag lattice and should be detected as a ring-like structure in the viral particle, as described for the VLPs (Fig. 28A). The focal plane of the assembly sites was located with an overview confocal image (40 μm x 40 μm) (Fig. 28B). A smaller area (5 μm x 4 μm) was selected and imaged by confocal and STED microscopy concurrently (Fig. 28C). Late assembly sites or accumulations of released viral particles were detected as big patches by confocal microscopy (Fig. 28C, upper row). STED imaging of the same area of interest revealed individual particles and assembly sites that were detected as ring-like structures in the focal plane (Fig. 28C, lower row). Zoom ins are depicted for a clearer illustration of the ring-like structures (Fig. 28C, lower row, right panel).

STED imaging at viral assembly sites enabled discrimination of immature late buds and released viral particles. Therefore, this system is further applied to the analysis of wild-type assembly sites in the absence of LPV.

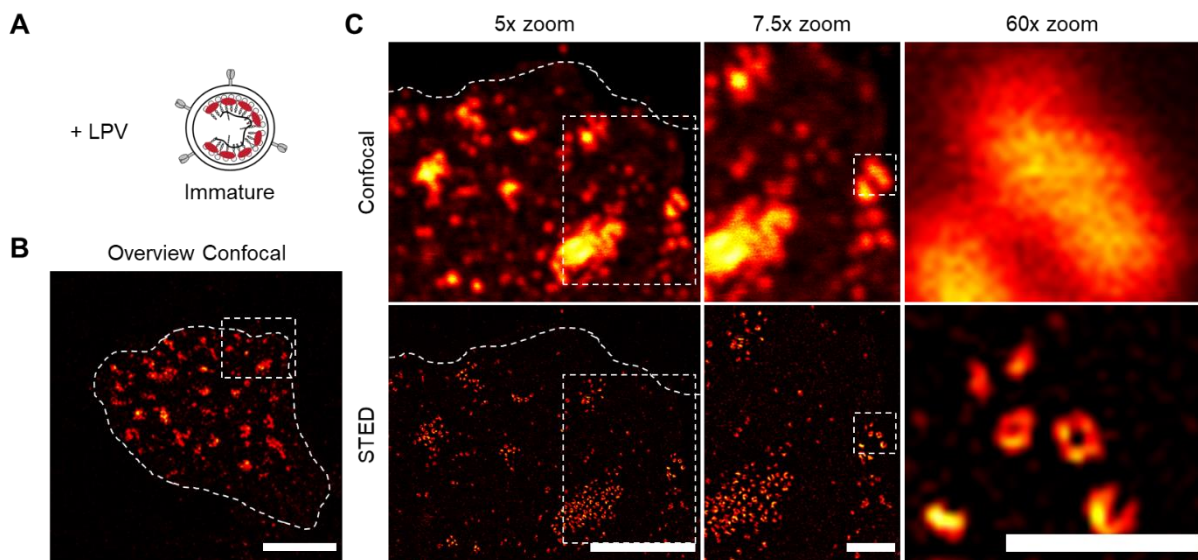


Fig. 28: Immature viral particles assemble at the plasma membrane of HeLa Kyoto cells. **A:** Schematic model of Clip tag inserted between MA and CA in Gag, flanked by PR cleavage sites. In an uncleaved state, it is part of Gag and can be observed as ring structure. **B:** Confocal image of immature (+LPV) assembly sites and trapped particles at the plasma membrane of HeLa Kyoto cells stained with SiR-Clip. HeLa Kyoto cells were co-transfected with pCHIV^{iClip} and pCHIV wt in a 1:1 molar ratio and treated with 2 μm LPV. 24 hpt, cells were stained with 1 μm SiR-Clip for 45min at 37°C and washed for 30 min prior to imaging by STED microscopy. Scale bar 10 μm . **C:** Zoom of assembly sites and trapped particles stained with SiR-Clip detected by confocal and STED microscopy and zoom ins as stated. Scale bar left: 2 μm , middle: 1 μm and right: 0.5 μm .

The analysis of transfected HeLa Kyoto cells in the absence of LPV was conducted as described for the immature assembly sites (Fig. 29). During the assembly process, late viral buds will be detected as ring-like structure, while proteolytic cleavage of Gag produces particles containing freely diffusing Clip-tag which should be captured as a compact “blob” (Fig. 29A). An overview image of the focal plane was measured by confocal microscopy (Fig. 29B). Upon higher magnification (zoom ins), areas that resembled patches in confocal microscopy revealed individual particles by STED imaging (Fig. 29C). Immature ring structures were detected in combination with mature blobs. This indicated the asynchronous assembly of viral particles on one cell and depicted stages of assembly and budding (ring structures) and mature

viral particles (blobs), indicating that processing does indeed occur under the conditions and in the time frame used in our experiments.

Hanne et al., 2016 visualized maturation of purified viral particles upon PR activation. This process was locally blocked in the field of view after imaging of viral particles by STED microscopy. Although the mature and immature structures were resolved at assembly sites by STED microscopy, measuring dynamic processes of PR activity during the viral assembly could not be accomplished with this system.

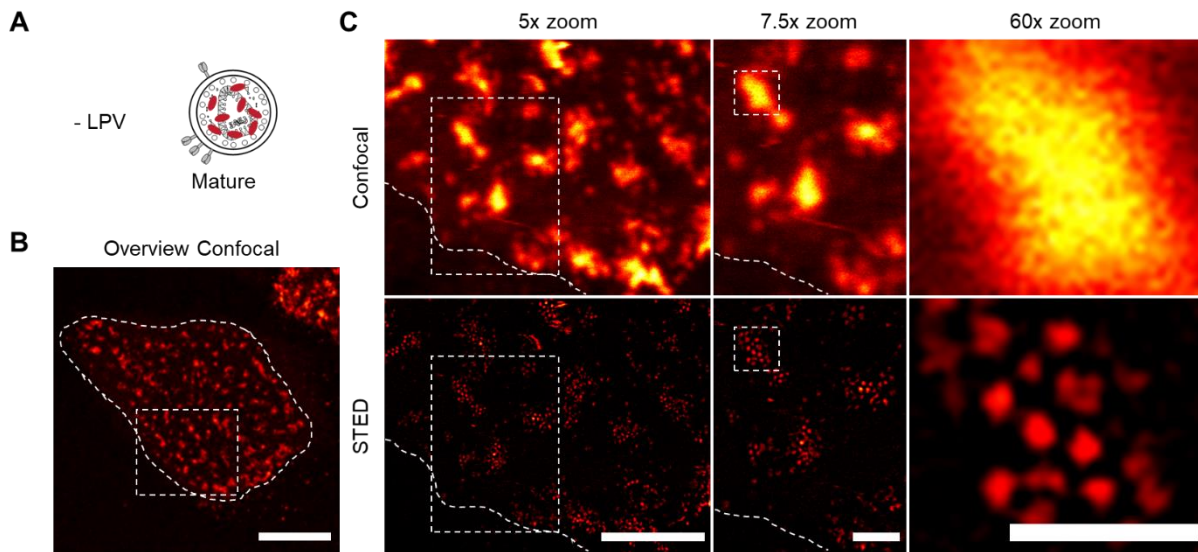


Fig. 29: Virus-like particles assemble at the plasma membrane of HeLa Kyoto cells in the absence of LPV. **A:** Schematic model of Clip tag inserted between MA and CA in Gag, flanked by PR cleavage sites. In a cleaved state, it freely diffuses in the particle and is detected as a blob. **B:** Confocal image of wt (-LPV) assembly sites and trapped particles at the plasma membrane of HeLa Kyoto cells stained with SiR-Clip. HeLa Kyoto cells were co-transfected with pCHIV^{iClip} and pCHIV wt in a 1:1 molar ratio. 24 hpt, cells were stained with 1 μm SiR-Clip for 45 min at 37 °C and washed for 30 min prior to imaging by STED microscopy. Scale bar 10 μm. **C:** Zoom of assembly sites and trapped particles stained with SiR-Clip detected by confocal and STED microscopy and zoom ins as stated. Scale bar left: 2 μm, middle: 1 μm and right: 0.5 μm.

6.3.2.3 Changes in fluorescence lifetime of eCFP in Gag can be visualized by FLIM microscopy

Close interaction of two molecules of the fluorescent protein eCFP result in a process called homo-FRET that can be measured by changes in the fluorescence lifetime of the protein (FLIM, (Suhling et al. 2015)). We tested, whether this property can be exploited as a readout for Gag processing. For this, eCFP was inserted in Gag in between the MA and CA domains (Fig. 30). The fluorophore was either flanked by two PR cleavage sites to allow for free diffusion in the particle upon proteolytic processing (ieCFP), or only by a C-terminal processing site, resulting in retention at the membrane bound MA domain after processing. and merely rearrange on the viral membrane after PR dependent cleavage (eCFP) (Fig. 30A). In the immature state, the fluorophore is part of the Gag lattice in both cases.

This project is a collaboration with the AG Lamb (Munich). They designed a system for imaging with laser scanning confocal (LSC) microscopy combined with Time-Correlated Single Photon

Counting (TCSPC). FLIM data is analyzed in the phasor space by observing clustering of pixels values in specific regions (Digman et al. 2008). For further information, see Materials and Methods.

To test specific PR dependent processing of pCHIV^{ieCFP} and pCHIV^{eCFP}, they were co-transfected with a wild-type pCHIV in a 1:1 ratio in the presence and absence of LPV. VLPs were purified from the supernatant of virus-producing HEK293T cells and analyzed by immunoblot with antisera detecting GFP and its derivatives or CA. For pCHIV^{ieCFP} and pCHIV^{eCFP} ± LPV, Gag.eGFP was detected with both antisera (~80kDa) (Fig. 30B, lane 2, 4, 6, 8). Proteolytic processing was detected for both constructs in the absence of LPV. pCHIV^{ieCFP} produced free eCFP (~27kDa), as well as CA (~24kDa) (Fig. 30B, lane 1 and 5). For pCHIV^{eCFP}, GFP antiserum detected a band ~40kDa, depicting MA-eCFP (Fig. 30B, lane 3). Processed CA was displayed precisely as for pCHIV^{ieCFP} (~24kDa) (Fig. 30B, lane 7). The designed constructs were proteolytically cleaved in the expected products of free eCFP and MA-eCFP. Therefore, they were assumed functional and applicable for further analysis. Next, the fluorescence lifetime of mature and immature pCHIV^{ieCFP} and pCHIV^{eCFP} in purified VLPs was determined.

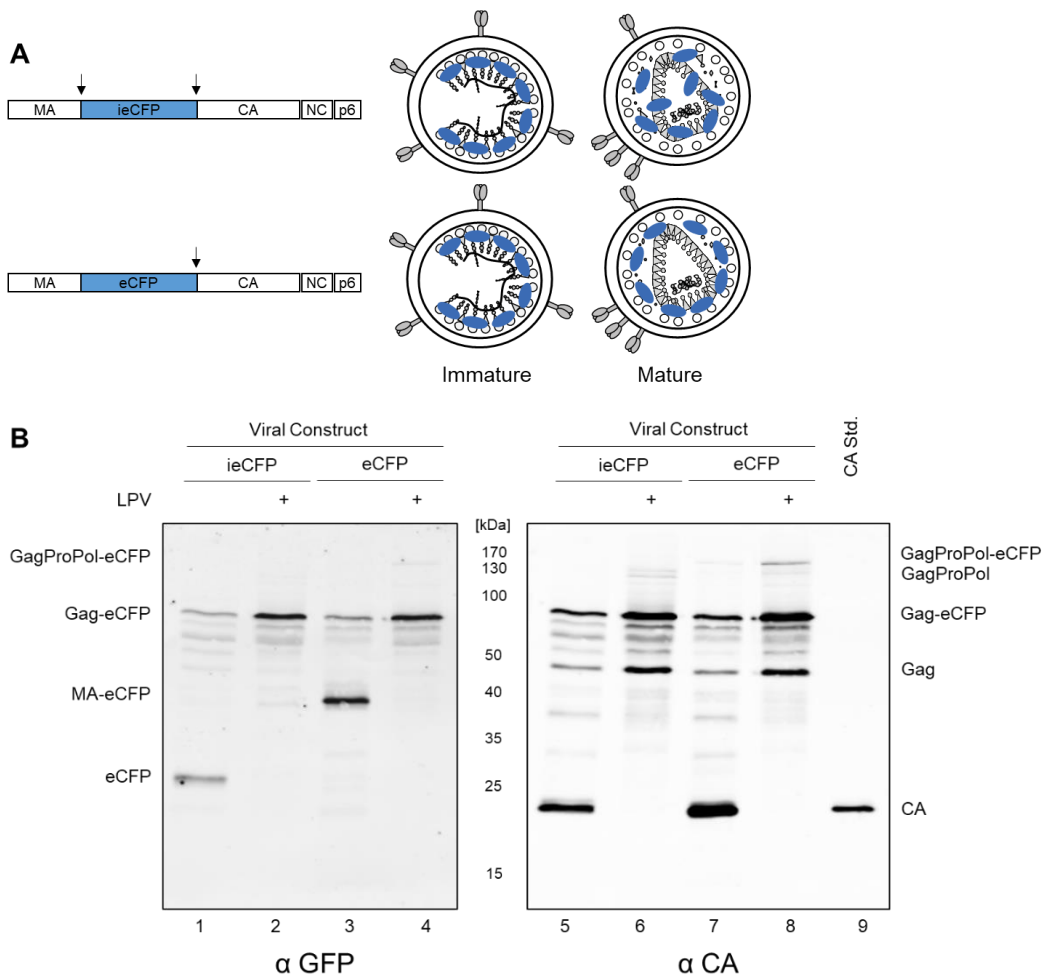


Fig. 30: Analysis of proteolytic processing of Gag.ieCFP and Gag.eCFP by immunoblot. A: Schematic model of eCFP tag inserted between MA and CA in Gag. It is either flanked by PR cleavage sites (ieCFP) or just one cleavage site between the protein and CA (eCFP). **B:** 293T cells were co-transfected with pCHIV^{ieCFP} or pCHIV^{eCFP} and pCHIV wt in a 1:1 molar ratio and either untreated or treated with 2 μm LPV. 48 hpt, supernatants were harvested and concentrated via ultracentrifugation through a 20% sucrose cushion, followed by immunoblot analysis using antiserum raised against GFP and HIV-1 CA.

Purified VLPs were analyzed by Fluorescence Lifetime Imaging Microscopy (FLIM) in collaboration with the AG Don Lamb (Department of Physical Chemistry, LMU Munich) (Fig. 31). Purified HIV^{ieCFP} and HIV^{eCFP} particles produced in presence or absence of LPV were imaged and depicted in false colors in relation to the fluorescence lifetime determined (Fig. 31A). Frequency analysis revealed a gaussian distribution of fluorescence lifetime values for the particles. Immature particles showed comparable lifetime for both virus derivatives of 1.9-2.4 ns, with a peak at 2.23 ns or 2.18 ns (Fig. 31A, B, left panel). In both cases, localization of the fluorescent tag in Gag resulted in interaction of the proteins within the rigid immature lattice, which in turn led to low eCFP FLIM values. Mature HIV^{eCFP} particles displayed increased fluorescence lifetime values of 2.2-2.8 ns (Fig. 31A, B, upper panel), consistent with enhanced mobility of mature MAeCFP at the viral membrane. The mean fluorescence lifetime of all particles shifted from 2.23 ns to 2.41 ns. Strong overlap of the populations depicted by frequency analysis prevented distinction of immature and mature particles with the pCHIV^{eCFP} construct due to the shift of ~ 0.2 ns (Fig. 31B, upper panel).

PR dependent cleavage of Gag in HIV^{ieCFP} led to a shift of mean fluorescence lifetime from 2.18 ns obtained for articles prepared in the presence of LPV to 2.57 ns for particles produced in the absence of LPV. (Fig. 31A, B, lower panel). A broadening of the values detected from 2.4-3.0 ns and a clear separation of particles in two populations was observed in this case. The distribution of one population corresponded to the one obtained for particles generated in the presence of LPV, the other displayed higher fluorescence lifetimes, indicating the co-existence of immature and mature particles in these samples. (Fig. 31B, lower panel). Since these results indicated that FLIM measurements were suitable to discriminate between mature and immature particles, we proceeded to live-cell measurements.

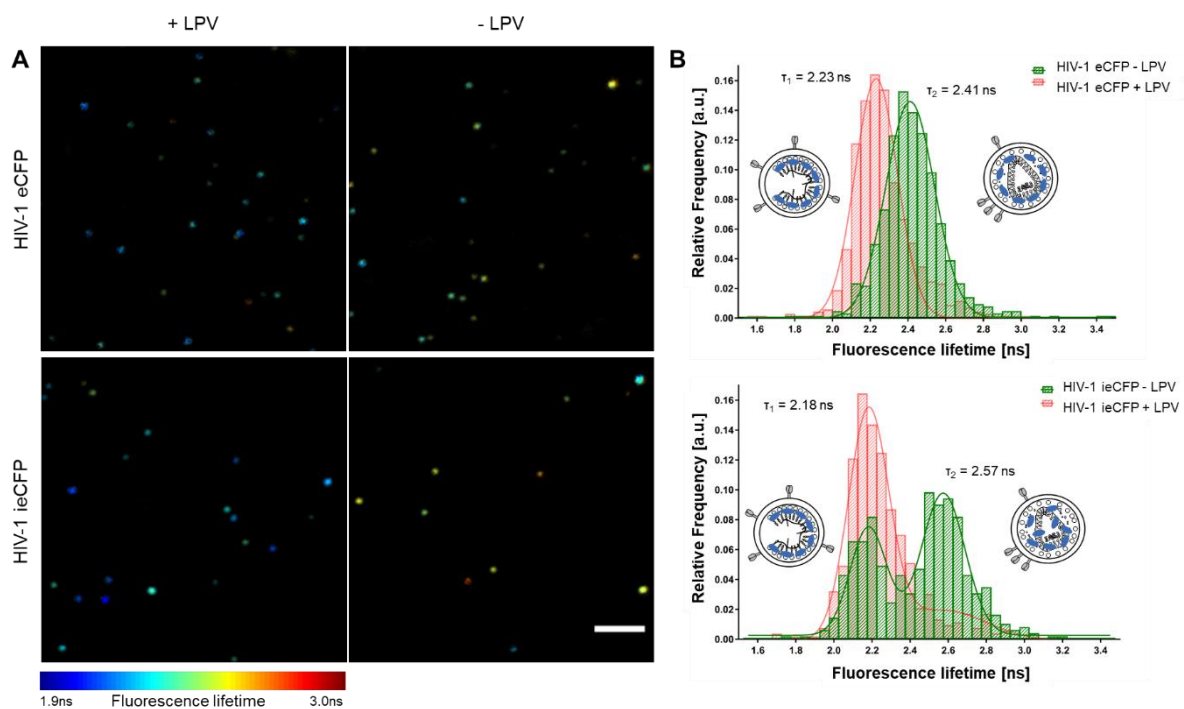


Fig. 31: Measurements of fluorescence lifetime of eCFP in purified VLPs. A: Confocal images of pCHIV containing eCFP and ieCFP in presence (immature) and absence (wild-type) of LPV. 293T cells were co-transfected with pCHIV^{ieCFP} or pCHIV^{eCFP} and pCHIV wt in a 1:1 molar ratio and either untreated or treated with 2 μ m LPV. 48 hpt, supernatants were harvested and concentrated via ultracentrifugation through a 20% sucrose cushion, followed by imaging with LSC microscopy combined with Time-Correlated Single Photon Counting (TCSPC). The lifetime

ranging from 1.9-3.0 ns is depicted by the LUT jet. Scale bar 5 μ m. **B:** Particle lifetimes were extracted using phasor analysis. Frequency distribution analysis of mean lifetime values of indicated viral particles. n=500 particles.

After validation of the system, fluorescence lifetime measurements of eCFP constructs were then conducted in HeLa Kyoto cells expressing the viral constructs to assess the expected differences in fluorescence lifetime due to proteolytic processing (Fig. 32).

First, lysates of transfected cells were analyzed by immunoblot using antisera against GFP and MA (Fig. 32B). The cleaved eCFP moiety detected by the GFP antiserum displayed a slightly higher electrophoretic mobility than free eCFP due to an attached linker in the vector. Lysates from cells expressing MA.eCFP displayed the expected signal at ~40 kDa reactive with both antisera; an additional band at ~25 kDa detected with the α GFP serum likely represented an intracellular degradation product. Gag.eCFP was also detected with both antisera, displaying an apparent molecular mass of ~80 kDa. As expected, untreated cells transfected with the viral constructs displayed mainly free MA (17 kDa) and eCFP (27 kDa), while only precursor proteins were detected upon LPV treatment.

We then proceeded to record FLIM images of eCFP expressed in different contexts in HeLa Kyoto cells 24 hpt. As a baseline, we first measured free eCFP expressed in the cytosol by focusing on the central plane of the cell. This yielded a mean fluorescence lifetime of 2.8-2.9 ns (Fig. 32A, upper left panel), comparable to literature values (3.0 ns; Kremers et al., 2006). In order to determine whether fusion of eCFP to the MA domain of Gag by itself influenced the fluorescence lifetime of the fluorophore, we performed comparative measurements with cells expressing a MA.eCFP fusion protein. Compared to eCFP alone, cytosolic MA.eCFP showed a shorter lifetime of 2.4-2.5 ns (Fig. 32A, upper right panel), comparable to the value obtained for mature HIV^{eCFP} VLPs (Fig. 31A, upper right panel). This might be due to clustering of the proteins in the cytoplasm induced by MA, or the influence of MA on the tag itself. Assembly sites at the plasma membrane of HeLa Kyoto cells expressing pCHIV^{ieCFP} in the presence of LPV exhibited a shorter lifetime of 1.9-2.4 ns (Fig. 32A, lower left panel). These values were in line with measurements of immature VLPs (Fig. 31A, left panel). Viral buds in cells producing pCHIV^{ieCFP} exhibited longer lifetimes (~2.5 ns) for small punctae (area of 4-40 pixels), but bright patches featured a lifetime comparable to the immature sites (1.9-2.4 ns; Fig. 32A, lower right panel).

PR-dependent differences in fluorescence lifetime of eCFP at assembly sites on the plasma membrane were observed for still images. Quantification of fluorescence lifetime at single assembly sites was conducted to determine the exact changes in fluorescent lifetime induced by proteolytic processing of Gag.ieCFP.

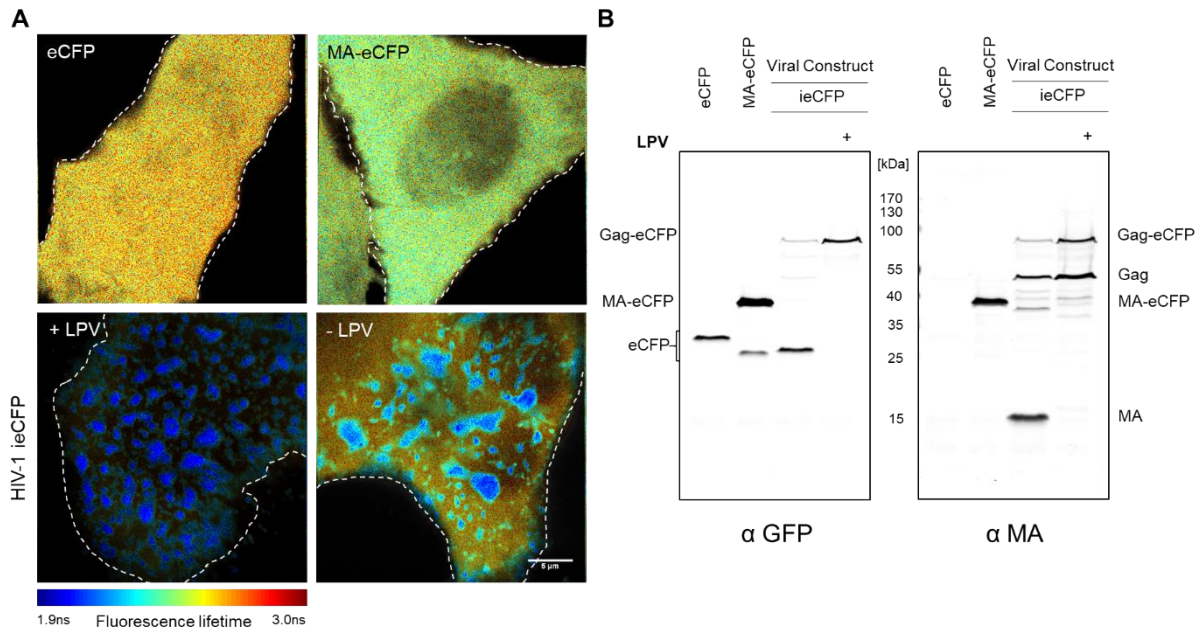


Fig. 32: Measurements of fluorescence lifetime of eCFP in HeLa Kyoto cells. HeLa Kyoto cells were transfected with eCFP and MA-eCFP and co-transfected with pCHIV^{ieCFP} and pCHIV wt in a 1:1 molar ratio, either untreated or treated with 2 μ m LPV. 24 hpt, cells were either imaged by LSC microscopy combined with TCSPC or lysed for immunoblot analysis. **A:** Confocal images of cytoplasmic eCFP and MA-eCFP, as well as assembly sites and trapped particles of pCHIV containing ieCFP in presence (immature) and absence of LPV. Fluorescence lifetimes were extracted using phasor analysis. The lifetime ranging from 1.9-3.0ns is depicted by the LUT “jet”. Scale bar 5 μ m. **B:** Lysates of cells transfected with the indicated constructs were separated by SDS-PAGE and analyzed by detected by quantitative immunoblot (Li-Cor) using the indicated antisera.

Fluorescence lifetime of HIV^{ieCFP} assembly sites expressed in the presence or absence of LPV was quantified for individual punctae (area of 4-40 pixels) and the relative frequency distribution was plotted (Fig. 33). For cells grown in the presence of LPV, a gaussian distribution of lifetimes in the range of 1.8-2.2 ns was observed (Fig. 33, left panel); the distribution of intensities was comparable between different cells. For cells grown in the presence of LPV, the population shifted to higher lifetimes (2.0-2.4 ns, Fig. 33, right panel), but these values were still lower than the lifetimes measured for purified mature VLPs (2.57 ns, Fig. 31). A possible explanation for this discrepancy is that the cellular background influenced the measurement. Alternatively, the time point chosen for recording was not optimal. Therefore, cells were next monitored over a longer time period.

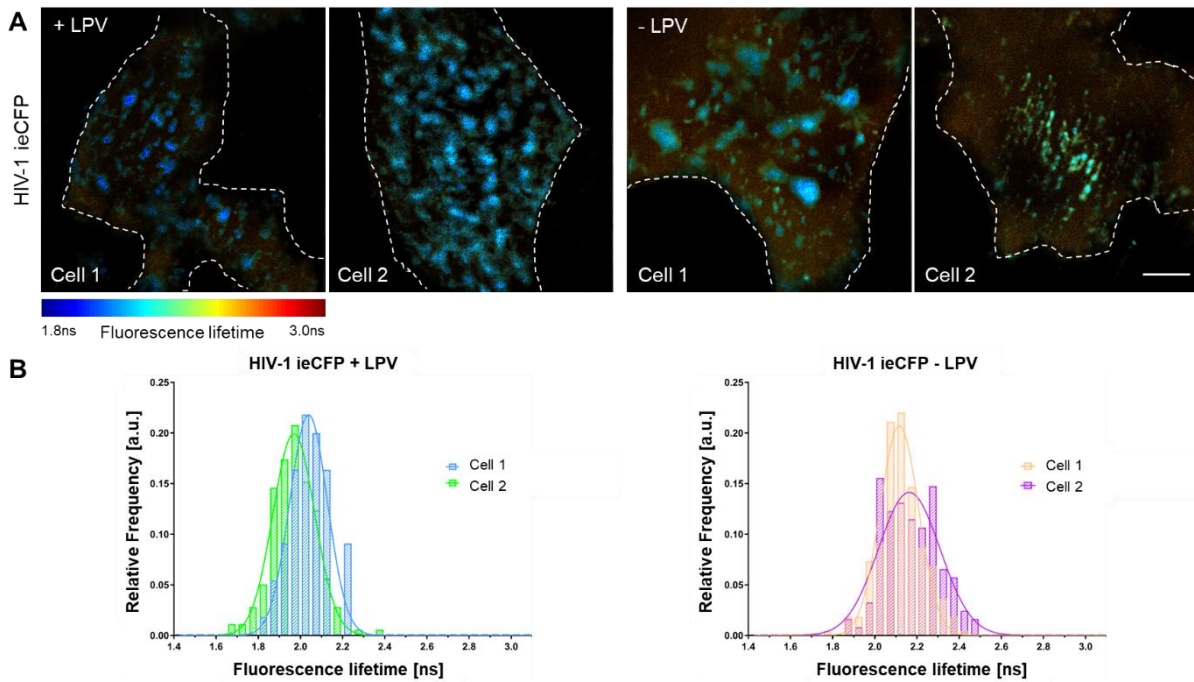


Fig. 33: Lifetime distribution comparing immature (+LPV) and mature (-LPV) assembly sites at the plasma membrane of HeLa Kyoto cells. **A:** HeLa Kyoto cells co-transfected with pCHIV^{ieCFP} and pCHIV wt in a 1:1 molar ratio were either untreated or treated with 2 μ m LPV. At 24 hpt, cells were imaged by LSC microscopy combined with TCSPC. Fluorescence lifetimes of eCFP were extracted by phasor analysis. The lifetimes ranging from 1.8-3.0 ns are depicted using the LUT “jet”. Scale bar 5 μ m. **B:** Frequency distribution analysis of mean lifetime values. The histograms summarize data for 50 individual sites per cell for two cells per condition.

The plasma membrane of a pCHIV^{ieCFP} expressing cell was observed for two hours and images were acquired every 30 min (Fig. 34). 80 frames were obtained for each timepoint to sum up the amount of photons at each spot. Fluorescence lifetimes of all sites at the plasma membrane were analyzed in bulk and the frequency distribution over time was analyzed. At the onset of observation (0 min), about 30 particles were detected, displaying a mean fluorescence lifetime of 2.0-2.4 ns (dark blue line). 30 min later, ~70 particles were observed and the values spread from 1.8-2.4 ns (30 min, light blue line). The shift to lower lifetimes might indicate molecular crowding due to Gag lattice formation at the budding site. After 1 h, the number of detected particles did not change, but the amount of particles with lower lifetime increased (60 min, green line). After 90 min, an increase of particle numbers was observed. The distribution of fluorescence lifetime stayed 1.8-2.4 ns, with a maximum at 2.0 ns (red line). After 2 hours, the peak of the population shifted to 2.2 ns (120 min, purple line). In summary, whereas an increase in particle number was observed over time, a shift of the population to longer fluorescence lifetime was not detected in these bulk analyses.

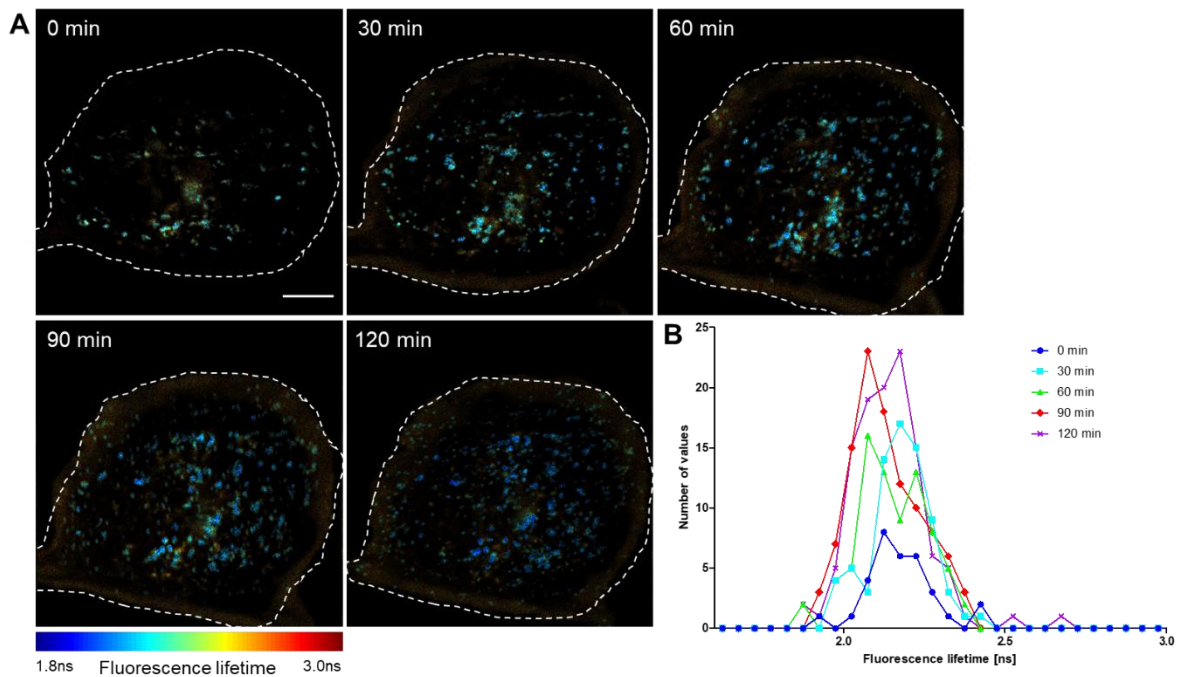


Fig. 34: Lifetime distribution of assembly sites during particle formation over time. **A:** HeLa Kyoto cells were co-transfected with pCHIV^{ieCFP} and pCHIV wt in a 1:1 molar ratio, either untreated or treated with 2 μ m LPV. At 24 hpt, cells were imaged by LSC microscopy combined with TCSPC for 80 frames every 30 min over 2 h. Fluorescence lifetimes of eCFP were extracted using phasor analysis. The lifetime ranging from 1.8-3.0 ns is depicted by the LUT "jet". Scale bar 5 μ m. **B:** Frequency distribution analysis of mean lifetime values of spots over 80 frames obtained at the indicated time points after the start of observation.

Next, imaging was performed at a higher time resolution in order to allow single particle tracking for a more detailed observation of changes in fluorescence lifetime (Fig. 35). The plasma membrane of pCHIV^{ieCFP} transfected HeLa Kyoto cells was imaged every 5s for 2h (Fig. 35A). Assembly sites were tracked by me using Imaris, and the fluorescence lifetime at individual sites was calculated by Chen Quian (AG Lamb). Tracking of individual assembly sites revealed a signal intensity increase of Gag.eCFP with the typical saturation exponential assembly kinetics as described earlier (Fig. 35B, red lines), but only minor changes in fluorescent lifetime over time were observed for a small number of tracks analyzed (4/ 100) (Fig. 35B, blue lines). This may at least in part be due to the fact that Gag clustering during the assembly process should lead to a decrease of fluorescence lifetime; this would obscure an increase due to proteolytic processing, if both processes coincide.

The findings from live-cell imaging were in line with the bulk analysis but did not allow an estimation of proteolytic processing of Gag during the assembly process. Further optimization of the imaging and analysis is needed to improve this approach. Attempts to diminish phototoxicity and reduce cellular background are being discussed. This is currently ongoing in collaboration with the Lamb group.

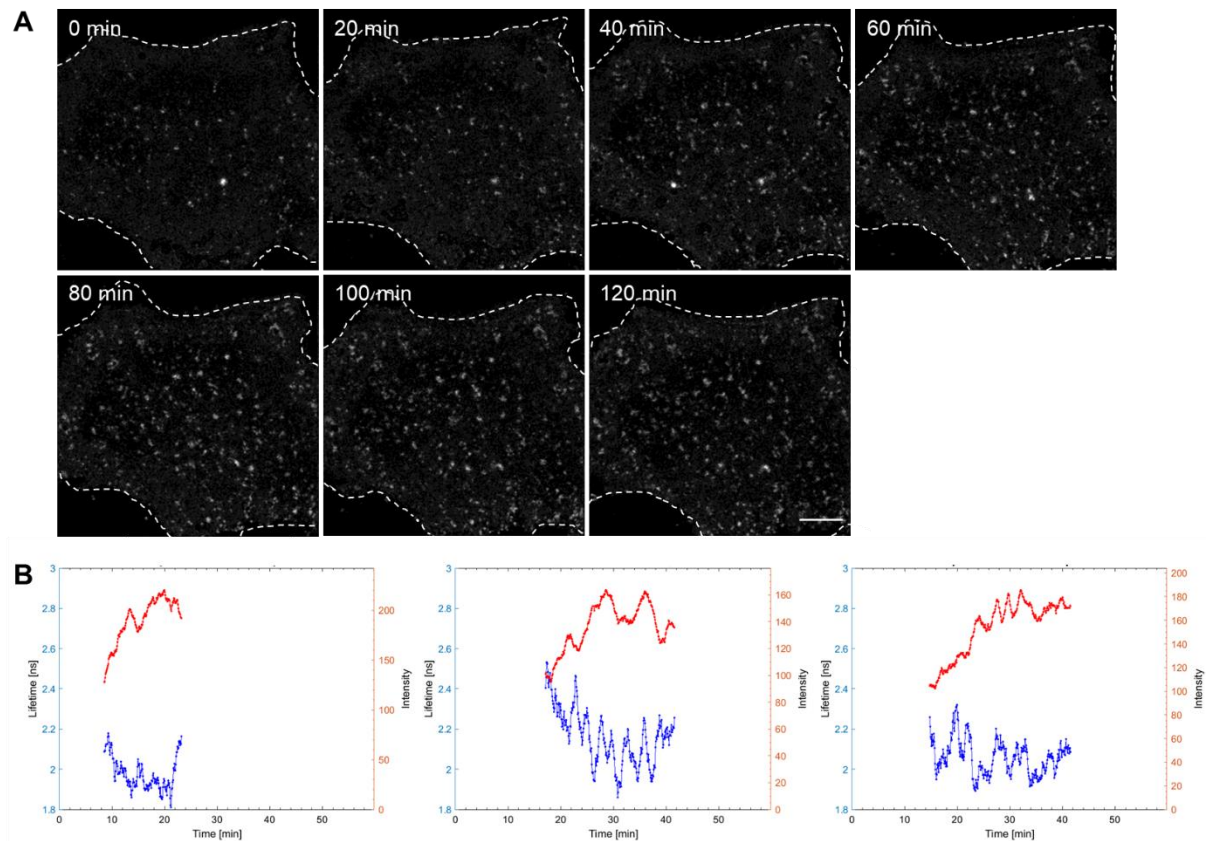


Fig. 35: Changes in eCFP fluorescence lifetime during viral assembly. Time lapse measurement of Gag.ieCFP assembly at the plasma membrane of HeLa Kyoto cells. HeLa Kyoto cells were co-transfected with pCHIV^{ieCFP} and pCHIV wt in a 1:1 molar ratio. 24 hpt, cells were imaged by LSC microscopy combined with TCSPC with a frame rate of 0.2 s⁻¹ over a period of 2 h. The figure shows frames captured at the indicated time points. Scale bar 5 μ m. **B:** Fluorescence lifetimes were extracted using phasor analysis and plotted over time for single tracks (blue lines) in parallel to the respective eCFP fluorescence intensity (red lines). Phasor analysis was performed by Chen Quian, LMU Munich.

6.3.3 Design of fluorogenic HIV-1 PR inhibitors to specifically visualize the active PR

A different, innovative approach tested in this work was the detection of formation of active HIV-1 PR during the viral assembly process via a fluorogenic inhibitor derivative. The PR inhibitor Ritonavir (RTV) that binds to the active site of the PR dimer was coupled to the fluorogenic dye silicone-rhodamine (SiR) (Fig. 36). SiR exists in a spironolactonic form that is non-fluorescent, as well as in a fluorescent zwitterionic conformation (Fig. 36A). The equilibrium between a non-fluorescent lactonic and fluorescent zwitterion structure is sensitive to hydrophobic effects (Lukinavičius et al., 2013). The conformation depends on the environment; therefore, fluorescence efficiency is strongly altered by binding to a target. RTV is a PR inhibitor which binds strongly to mature HIV-1 PR, but with much lower affinity to the PR moiety of the unprocessed GagProPol precursor (Humpolíčková et al. 2018).

Here, I explored whether binding of a RTV-SiR derivative to the active site of HIV-1 PR would allow detection of the formation of active HIV-1 PR by a fluorescence signal (Fig. 36B). Different carbon linkers were tested for optimal fluorogenicity of SiR, carrying either two (SiR-C2-RTV, Fig. 37A), four (SiR-C4-RTV, Fig. 38A) or six (SiR-C6-RTV, Fig. 39A) carbon

molecules. All compounds were synthesized by our collaborators Jiří Schimer and Jan Konvalinka (IOCB Prague).

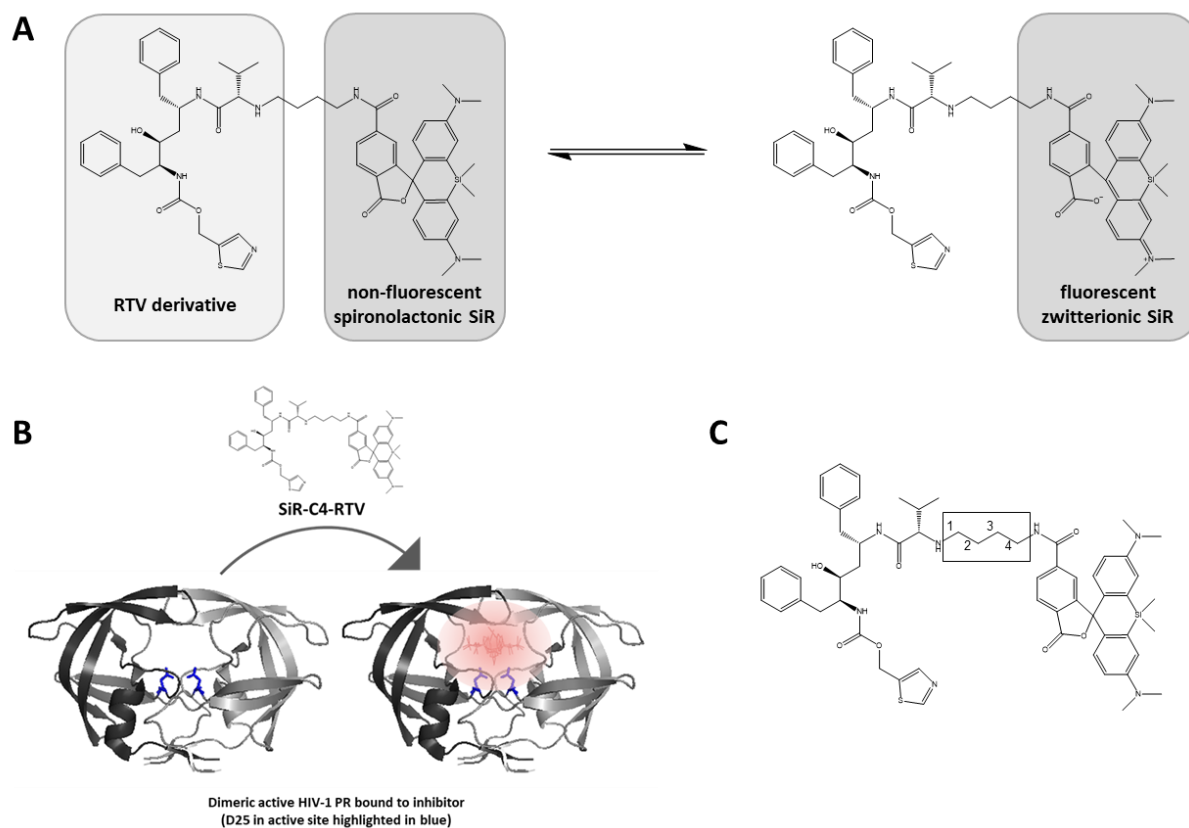


Fig. 36: Design of a fluorogenic probe to detect active PR. **A:** SiR adopts an open or a closed conformation depending on the environment of the molecule. It was coupled to PR inhibitor Ritonavir specifically bind the active site of HIV-1 PR. **B:** Principle of the assay: Binding of SiR-RTV to the mature HIV-1 PR should result in enhanced fluorescence. PR structure adapted from from PDB ID: 3el1. **C:** Structure of SiR-RTV. Different probes with varying linkers were tested. 2-carbon, 4-carbon and 6-carbon linkers were used in this study. The compound with a 4-carbon linker is shown here.

6.3.3.1 Specific fluorogenicity of the probes was validated by spectrophotometry

First, *in vitro* binding experiments were conducted to determine fluorogenicity of the three probes and the effect of specific interaction with HIV-1 PR. 200 nM SiR-C2-RTV (Fig. 37), SiR-C4-RTV (Fig. 38) and SiR-C6-RTV (Fig. 39) were analyzed by spectrophotometry. SiR fluorogenicity depends on the hydrophobic environment of the probe. Ethanol (EtOH) enforces a closed, non-fluorescent conformation, while SDS drives it to the zwitterionic fluorescent form. This was validated by excitation spectra. Relative fluorescence intensity at 675nm was recorded upon excitation in the range of 250-660 nm (Fig. 37B, 38B, 39B). While a small peak at 280 nm was detected for the sample in EtOH, no emission was detected at 650nm, the expected emission maximum of SiR (blue line). When samples were measured in PBS/0.1 % SDS maximum excitation was observed from 630-650 nm (orange line). The turn-on of the probes was measured by recording emission spectra. Emission was detected in the range of 645-749 nm upon excitation with 635 nm (Fig. 37C, 38C, 39C). Measurements of the probe in EtOH or PBS/0.1 % SDS were performed as negative and positive controls, respectively. While only very low fluorescence signal was detected for EtOH (blue line), the highest emission intensity for all probes was measured in 0.1 % SDS in PBS (orange line).

Unspecific fluorescence signal due to unspecific protein binding was tested by adding 0.1 mg/ml BSA in PBS to the probes (pink lines). SiR-C2-RTV (Fig. 37C) and SiR-C4-RTV (Fig. 38C) exhibited high unspecific turn-on in these control measurements, while SiR-C6-RTV (Fig. 39C) showed only a weak signal intensity increase under these conditions.

Next, 600 nM purified HIV-1 PR was added to the probe in 0.1 mg/ml BSA in PBS (dark red lines). The addition of wild-type HIV-1 PR did not increase the fluorescence signal of SiR-C2-RTV compared to the BSA control (Fig. 37C). With SiR-C4-RTV, fluorescence was turned-on almost to the maximum signal obtained for 0.1% SDS in PBS (Fig. 38C). A strong specific fluorescence signal was also detected for SiR-C6-RTV (Fig. 39C). As a control, purified HIV-1 PR with the active site mutation D25N was mixed with the probes (green lines). Purified HIV-1 PR D25N also formed a dimer, but was catalytically inactive, therefore it controlled for specificity of the probes to active HIV-1 PR. This D25N mutation impaired RTV binding to the active site, because the aspartyl carboxy groups are necessary to activate the H₂O molecule obligatory for binding of RTV to PR (Konvalinka et al. 2015). None of the probes displayed an increase in fluorescence above the nonspecific protein background in this case, validating PR active site specificity of the observed signal. Interestingly, the unspecific signal detected in 0.1mg/ml BSA in PBS was decreased by the addition of PR D25N to SiR-C2-RTV and SiR-C4-RTV (Fig. 37C, 38C).

To further validate specificity of probe binding, an excess (1 μ M) of a different PR-inhibitor (Darunavir; DRV) with stronger binding affinity to the HIV-1 PR active site compared to RTV was added for a competition experiment. (Fig. 38C, 39C, grey line) (Dierynck et al., 2007). This resulted in a decrease of fluorescence signal to the background level (Fig. 38C, 39C, pink line), indicating displacement of the SiR-RTV probes from the active site. Additionally, emission signal at 675 nm after excitation with 650 nm was measured over time after 1 μ M DRV was added (Fig. 37D, 38D, 39D). Fitting of the decay curve to a single exponential decay equation yielded rates of 0.08258 s⁻¹ for SiR-C2-RTV, for SiR-C4-RTV 0.05374 s⁻¹ and for SiR-C6-RTV 0.1809 s⁻¹. These apparent rates indicated a much higher off rate for the compounds than the k_{off} of 8.1 x 10⁻⁴ s⁻¹ determined for RTV alone (Dierynck et al., 2007), but detailed kinetic measurements *in vitro* were not yet performed. Modification of RTV by coupling to the dye did

influence its kinetics. While the apparent rates observed were in a similar range, the slowest displacement was observed for SiR-C6-RTV indicating better PR binding.

For visualization, the fold signal increase was normalized to EtOH (Fig. 37E, 38E, 39E). SiR-C2-RTV and SiR-C4-RTV exhibited a strong turn-on of ~50-fold and 60-fold, while SiR-C6-RTV only showed a turn-on of 35-fold in 0.1 % SDS in PBS (Fig. 37E, 38E, 39E). Additionally, the unspecific turn-on of SiR-C2-RTV and SiR-C4-RTV was ~25-fold compared to only 3-fold for SiR-C6-RTV. When the signal intensity increase was normalized to values detected for 0.1 mg/ml BSA in PBS (Fig. 37F, 38F, 39F), the maximum turn-on in 0.1 % SDS in PBS was just 2.3-fold for SiR-C2-RTV and SiR-C4-RTV, while SiR-C6-RTV exhibited a ~9-fold signal increase. While specific turn-on after addition of PR led to a 7-fold increase for SiR-C6-RTV, SiR-C2-RTV only showed 1.2-fold and SiR-C4-RTV 2.2-fold signal increase. Based on these *in vitro* cuvette measurements, SiR-C6-RTV should provide a better signal-to-noise ratio for PR detection than the other two compounds. Since cuvette measurements in the presence of BSA represent a rather artificial control for non-specific binding compared to the environment of virus producing cells on a glass coverslip, side-by-side comparisons were also performed using live-cell imaging.

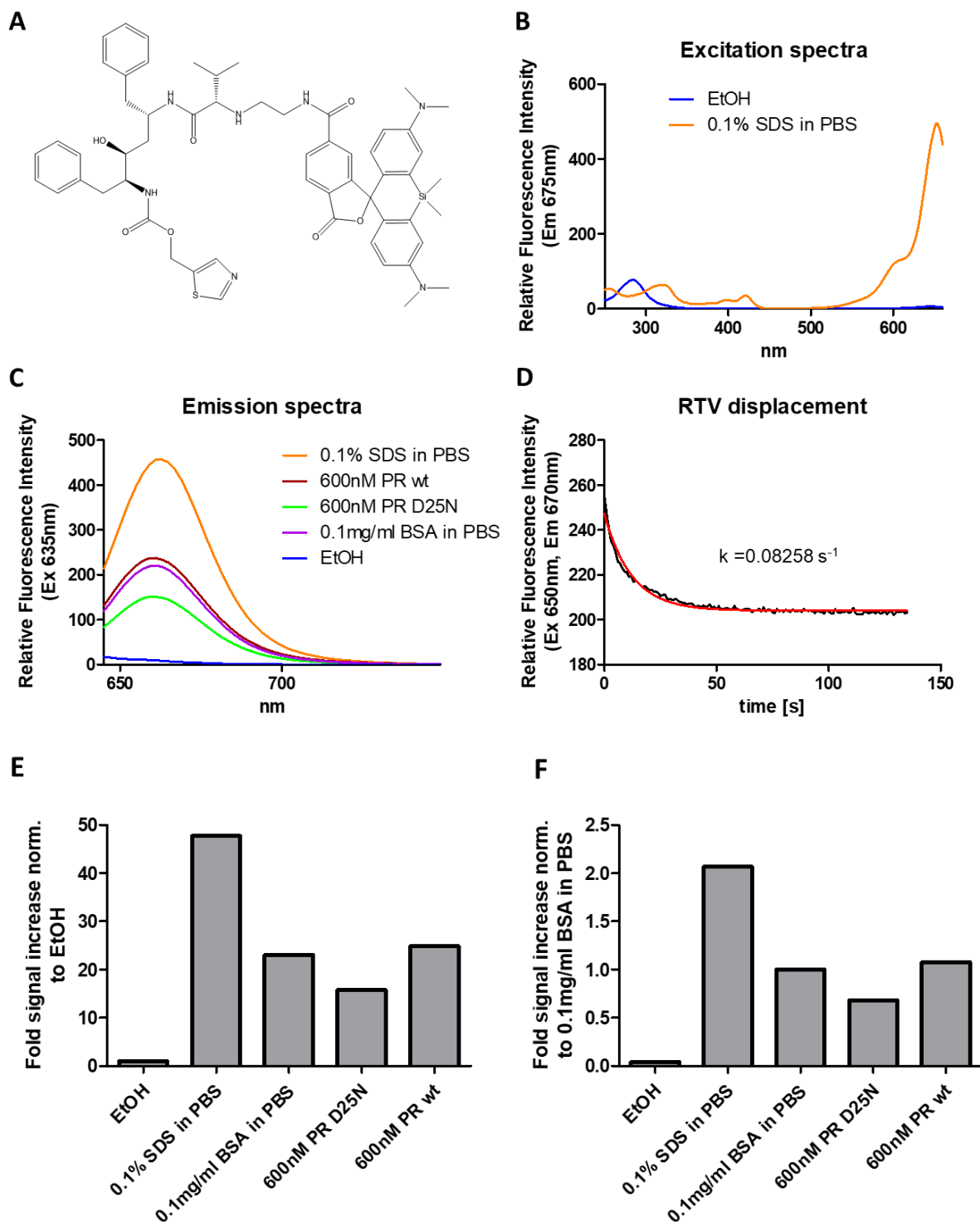


Fig. 37: Spectrophotometric analysis of SiR-C2-RTV. **A:** Structure of SiR-C2-RTV drawn with ChemDraw software. **B:** Excitation spectra of 200 nM SiR-C2-RTV in Ethanol (blue line) and 0.1 % SDS in PBS (orange line). Emission signal at 675 nm was detected for the excitation range of 250-660 nm. **C:** Emission spectra of 200 nM SiR-C2-RTV in presence of Ethanol (blue line), 0.1% SDS in PBS (orange line), 0.1 mg/ml BSA in PBS (purple line), 0.1 mg/ml BSA in PBS and 600 nM PR D25N (green line) and 0.1mg/ml BSA in PBS and 600 nM PR wt (dark red line). Emission signal in the range of 645-749 nm was measured after excitation with 635nm. **D:** Decrease of fluorescence signal detected after addition of 1 μM DRV due to inhibitor displacement. Fluorescence signal was measured every 1 s for emission at 675 nm after excitation with 650 nm. The data were fitted using GraphPad Prism to a single exponential decay equation (red line), yielding the indicated rate constant. **E:** Quantification of fold signal increase normalized to emission maximum in Ethanol. **F:** Quantification of fold signal increase of the emission maximum normalized to emission maximum obtained in 0.1 mg/ml BSA in PBS.

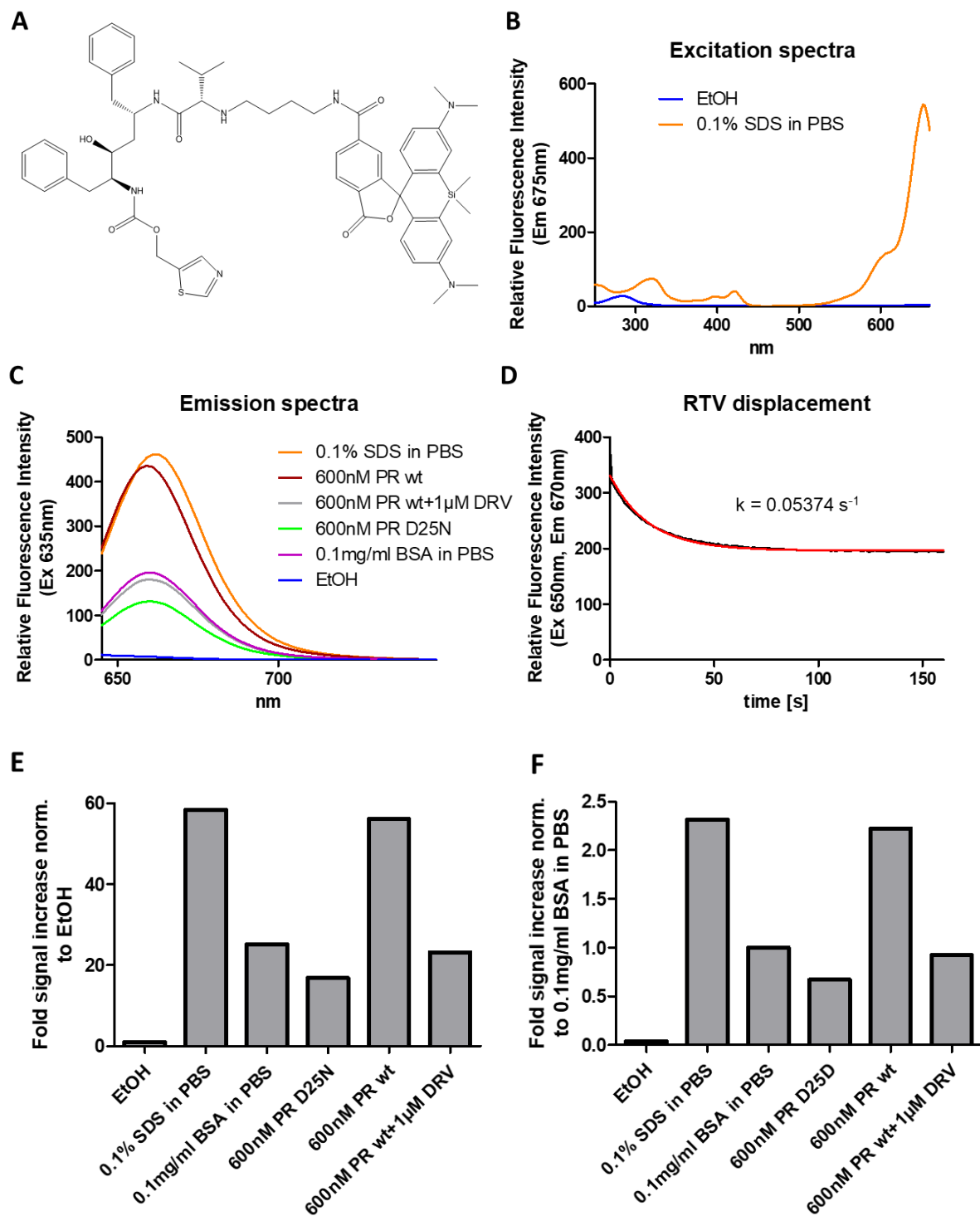


Fig. 38: Spectrophotometric analysis of SiR-C4-RTV. **A:** Structure of SiR-C4-RTV drawn with ChemDraw software. **B:** Excitation spectra of 200 nM SiR-C4-RTV in Ethanol (blue line) and 0.1 % SDS in PBS (orange line). Emission signal at 675 nm was detected for the excitation range of 250-660 nm. **C:** Emission spectra of 200 nM SiR-C4-RTV in presence of Ethanol (blue line), 0.1% SDS in PBS (orange line), 0.1 mg/ml BSA in PBS (purple line), 0.1 mg/ml BSA in PBS and 600 nM PR D25N (green line) and 0.1mg/ml BSA in PBS and 600 nM PR wt (dark red line). Emission signal in the range of 645-749 nm was measured after excitation with 635nm. **D:** Decrease of fluorescence signal detected after addition of 1 μ M DRV due to inhibitor displacement. Fluorescence signal was measured every 1 s for emission at 675 nm after excitation with 650 nm. The data were fitted using GraphPad Prism to a single exponential decay equation (red line), yielding the indicated rate constant. **E:** Quantification of fold signal increase normalized to emission maximum in Ethanol. **F:** Quantification of fold signal increase of the emission maximum normalized to emission maximum obtained in 0.1 mg/ml BSA in PBS.

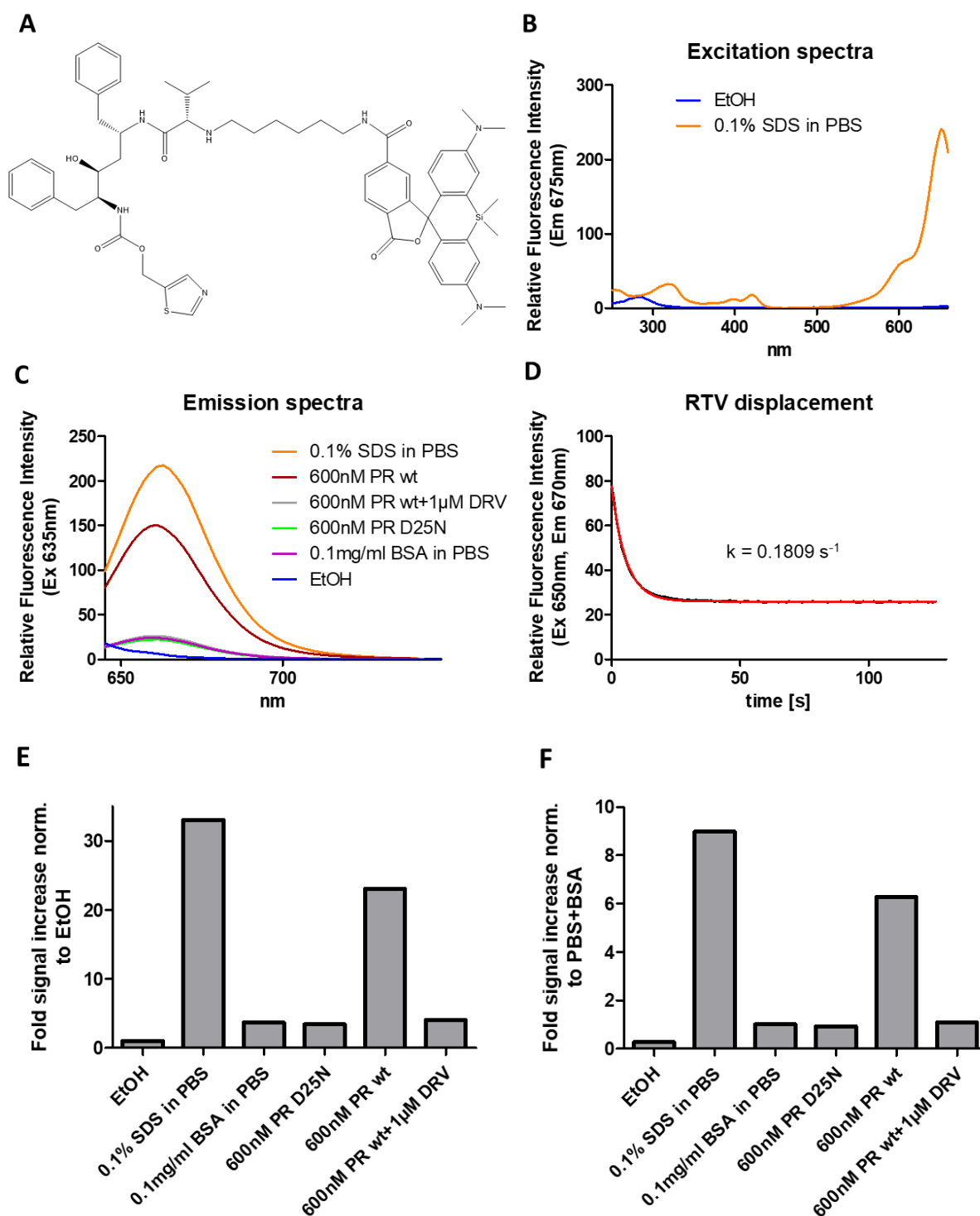


Fig. 39: Spectrophotometric analysis of SiR-C6-RTV. **A:** Structure of SiR-C6-RTV drawn with ChemDraw software. **B:** Excitation spectra of 200 nM SiR-C6-RTV in Ethanol (blue line) and 0.1 % SDS in PBS (orange line). Emission signal at 675 nm was detected for the excitation range of 250-660 nm. **C:** Emission spectra of 200 nM SiR-C6-RTV in presence of Ethanol (blue line), 0.1% SDS in PBS (orange line), 0.1 mg/ml BSA in PBS (purple line), 0.1 mg/ml BSA in PBS and 600 nM PR D25N (green line) and 0.1mg/ml BSA in PBS and 600 nM PR wt (dark red line). Emission signal in the range of 645-749 nm was measured after excitation with 635nm. **D:** Decrease of fluorescence signal detected after addition of 1 μ M DRV due to inhibitor displacement. Fluorescence signal was measured every 1 s for emission at 675 nm after excitation with 650 nm. The data were fitted using GraphPad Prism to a single exponential decay equation (red line), yielding the indicated rate constant. **E:** Quantification of fold signal increase normalized to emission maximum in Ethanol. **F:** Quantification of fold signal increase of the emission maximum normalized to emission maximum obtained in 0.1 mg/ml BSA in PBS.

6.3.3.2 Specific fluorogenicity of the probes detected at HIV-1 assembly sites in HeLa Kyoto cells

HeLa Kyoto cells in late stages of viral assembly were treated with 1 μM of the probes for 20 min and a fluorescent signal specific to the viral buds or released viral particles was detected for all compounds (Fig. 40). In agreement with the *in vitro* measurements (Fig. 37, 38, 39), SiR-C2-RTV and SiR-C4-RTV produced a higher unspecific background signal than SiR-C6-RTV, observed as blurry signal in the area surrounding the transfected cell and the cell surface (Fig. 40, middle column). Rigorous cleaning of the glass surface by 0.1 M HF treatment prior to cell seeding was essential to avoid excessive background from dye adhering to the glass coverslip. Even then, the background signal at the glass surface was higher than in the region covered by the plasma membrane. While the fluorescence signal recorded at assembly sites was threefold higher for SiR-C4-RTV than for SiR-C6-RTV, the higher unspecific background signal obtained with this probe impaired the recognition of specific marks.

Based on these measurements, SiR-C6-RTV was selected for further live-cell imaging experiments.

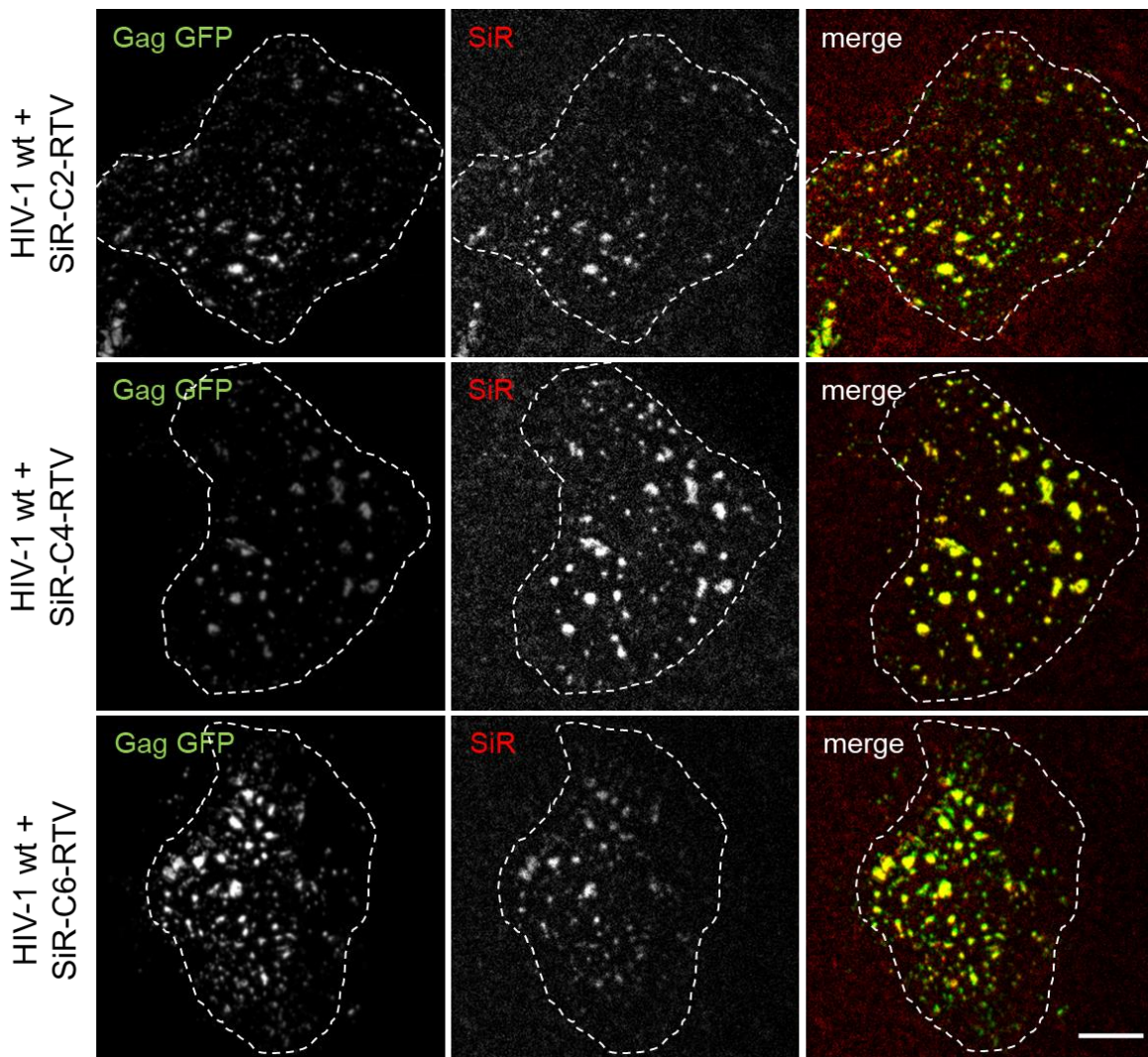


Fig. 40: PR-dependent SiR-RTV signal detected at HIV-1 Gag assembly sites by TIRF microscopy. HeLa Kyoto cells were transfected with pCHIV/pCHIVeGFP expressing wt HIV-1 PR. At 24 hpt cells were treated with 1 μM of the indicated probes for 20 min prior to imaging. Late assemblies at the ventral plasma membrane were imaged by TIRF microscopy. Scale bar: 10 μm .

For SiR-C6-RTV, further validation of signal specificity was conducted. Fluorogenic signals at assembly sites were determined for virus derivatives with an active PR and compared to signals obtained with variants that either lacked GagProPol (Gag only) or carried catalytically inactive PR (PR D25N). Testing whether SiR-RTV based detection is really specific for the mature form of PR also required a virus derivative capable of forming GagProPol dimers comprising a wild-type PR active site but unable to generate mature PR. For this, I constructed a variant of pCHIV in which all PR cleavage sites between NC and RT were mutated to impair autoprocessing (pCHIV^{NC-RT}). Finally, I used a variant with GagProPol and competed for binding of the SiR-RTV probe with 1 μ M of the stronger binding PR inhibitor DRV (Fig. 41).

Pol-SNAP was transfected in a 1:20 molar ratio with pGag.GFP to imitate the Gag to GagProPol ratio found in viral particles and cells were stained with SNAP-Cell 647-SiR as a positive control. Since the signals detected for SNAP-Cell 647-SiR bound to the SNAP-tag in GagProPol exceeded the signals detected for SiR-C6-RTV by 10-20-fold (Fig. 41B), measurements had to be performed using different microscope settings.

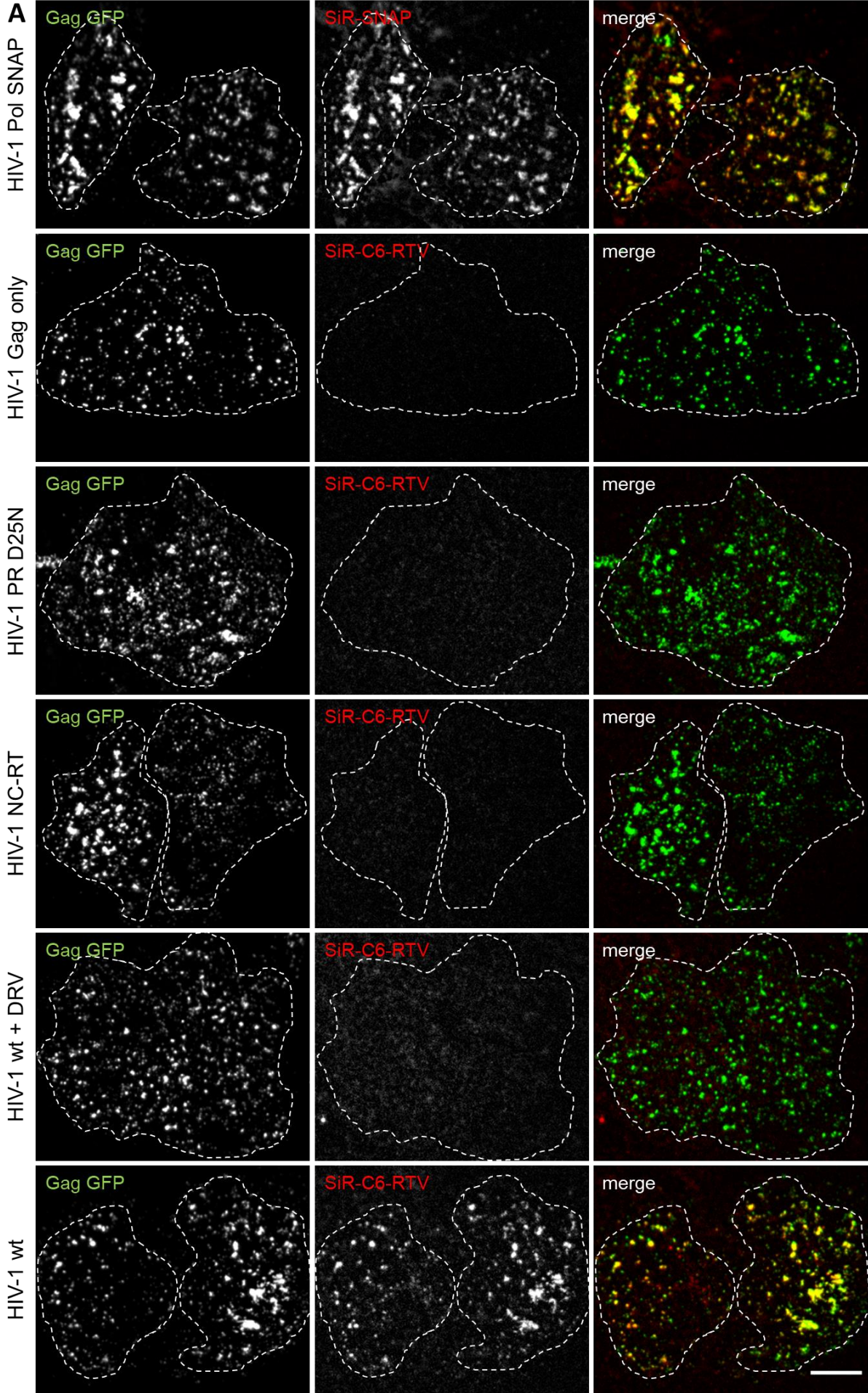
Assembly sites at the ventral plasma membrane were observed for all samples (Fig. 41A, left column). In contrast, clear specific SiR staining was only visually observed for the sample stained for GagProPol.SNAP and for the SiR-C6-RTV stained sample that should comprise mature PR in the absence of a PR inhibitor competitor (Fig. 41A, top and bottom row, respectively). Quantification of the mean SiR signal at the individual budding sites above background was performed and plotted as relative frequency distribution (Fig. 41B). The strong SiR signal obtained for GagProPol.SNAP served as a positive control for SiR fluorescence detection (Fig. 41A, B, 1st row). Assembly sites of HIV^{Gag only} which lack PR did not exhibit any specific signal for SiR-C6-RTV above background (Fig. 41A, 2nd row). Detected mean SiR signal intensities (up to 200) were therefore set as threshold for background signal (Fig. 41B, 2nd graph).

Assembly sites of virus expressing catalytically inactive PR D25N did not show any specific signal for SiR-C6-RTV as well (Fig. 41A, 3rd row). Quantification of signals at individual sites revealed a signal distribution comparable to Gag only (Fig. 41B, 2nd, 3rd graph). The absence of fluorescent signal for this probe supported the hypothesis that SiR-C6-RTV only stained active HIV-1 PR. (Fig. 41A, 4th row). Mean signal intensities were at background level (Fig. 41B, lower left graph).

Expression of wild-type pCHIV in presence of DRV lacked specific SiR signal at the assembly sites (Fig. 41A, 5th row). Quantified values were comparable to the negative controls (Fig. 41B, lower middle graph). This is in line with the competition assay conducted by spectrofluorometry measurements (Fig. 39D).

For assembly sites containing the wild-type HIV-1 PR, a specific signal was observed for SiR-C6-RTV (Fig. 41A, 6th row). Co-localization was illustrated in the merged image (right column). Frequency distribution analysis of quantified SiR signal shows a shift in the population. The specific signal increased 3-fold above background (Fig. 41B, lower right graph).

The specific signal shift rendered SiR-C6-RTV a promising candidate to label active HIV-1 PR during the assembly process and was therefore applied to time-lapse measurements of viral assembly.



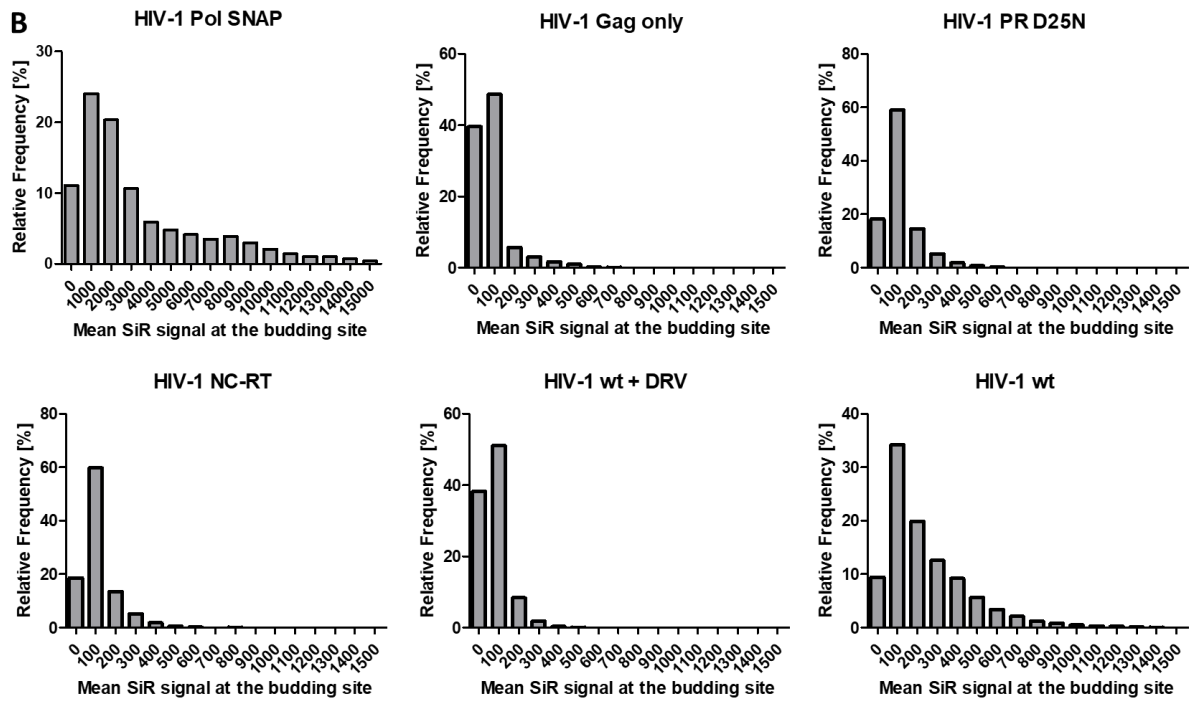


Fig. 41: PR-dependent SiR signal detected at HIV-1 Gag assembly sites by TIRF microscopy. A: HeLa Kyoto cells were transfected with pCHIV expressing pCHIV either lacking HIV-1 PR (Gag only), carrying catalytically inactive PR (PR D25N), autoprocessing defective PR (NC-RT), and wild-type PR, either untreated or treated with 5 μM DRV. GFP-tagged and unlabeled pCHIV was co-transfected in a 1:1 molar ratio. 24 hpt, cells were treated with 600 nM SiR-SNAP or 1 μM of SiR-C6-RTV for 20 min prior to imaging. Late assemblies at the ventral plasma membrane were imaged by TIRF microscopy. Images are representative for 10 cells imaged each in 3 independent experiments. Scale bar: 10 μm . B: Relative frequency distribution [%] of mean SiR signal intensity at the Gag budding site of $n=30$ cells from 3 independent measurements.

Live cell imaging of pCHIV^{eGFP} carrying wild-type PR was conducted in the presence of 1 μM SiR-C6-RTV during the assembly process (16 hpt) over a period of 2-4 hours (Fig. 42). Viral assembly sites were tracked to adjust for slight movements of the cell during live-cell imaging and mobility of viral particles after release. Analysis of pCHIV^{eGFP} assembly kinetics yielded in saturating exponential curves with rate constants as described above (Fig. 17).

A total of 250 sites from 3 cells that displayed an exponential increase in the Gag.eGFP channel was analyzed for fluorescence in the SiR channel. Quantitative analysis of signals in the SiR channel was challenging due to the high sensitivity required for these measurements – only ~60 molecules of mature PR per site can be expected to be present after completion of autoprocessing. Although a specific SiR signal was easily discernible by visual inspection of movies, low signal to noise ratio and fluctuations of the signal hindered quantitation of specific fluorescence in the SiR channel for a large fraction of assembly sites, but 50 sites analyzed to date allowed for such quantitative analysis. Since the pattern of SiR signal appearance differed between individual sites, each site was analyzed separately. The three exemplary assembly sites displayed in Fig. 42 were chosen based on their lack of mobility and the fact that they showed signal intensity increase of Gag.eGFP and SiR-C6-RTV over the period of observation (Fig. 42A). The three different patterns of appearance of the SiR signal were observed at these sites. In the upper panel, specific signal was detected 2500 s after the onset of assembly site formation, while the middle panel already displayed a SiR signal after 1250 s. For the lower panel, only a weak SiR signal was detected after 2500 s.

According to previously published analyses, HIV-1 Gag assembly takes ~ 10 min, while the viral particle is released after ~ 20 min (Ivanchenko et al. 2009). SiR signal increase was observed to be either (i) early, (ii) late or (iii) fluctuating. Early signal increase was detected after 10-20 min, suggesting PR activation during or at late stages of the viral assembly process (Fig. 42A, middle panel, 42C upper and lower panel). Later events were observed after ~ 40 min, indicating formation of active PR after viral release (Fig. 42A, upper and lower panel, 42C middle panel).

In summary, SiR-C6-RTV was successfully established to allow to monitoring formation of active HIV-1 PR during the viral assembly process in a time dependent-manner. The signal was not detected at all sites analyzed and the recruitment patterns with respect to the time course of assembly site formation differed between individual sites. Further analyses to determine the frequency of the different patterns are ongoing.

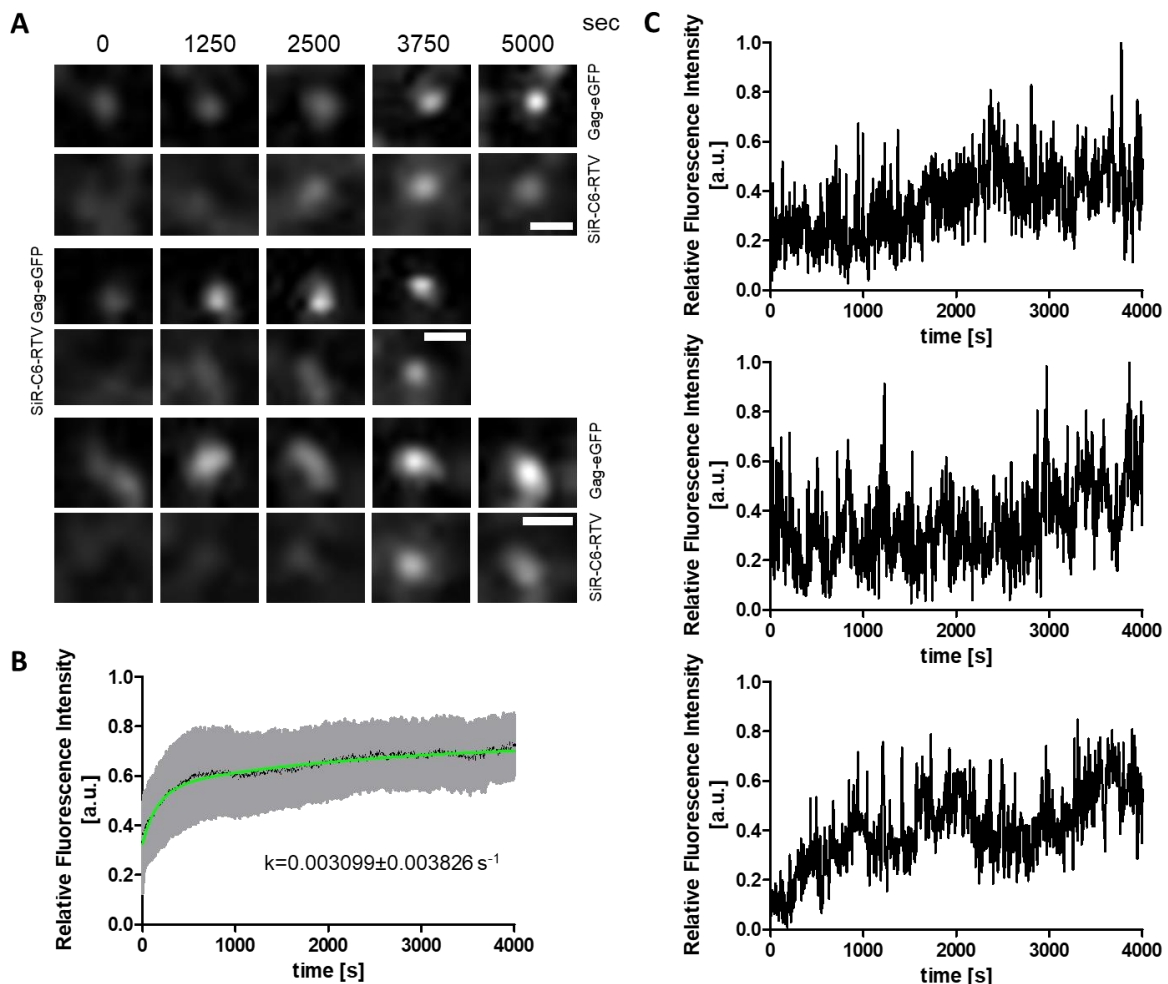


Fig. 42: Live-cell imaging of SiR-C6-RTV fluorescence signal during the viral assembly process. **A:** Time lapse measurement of Gag.eGFP assembly at the plasma membrane of HeLa Kyoto cells. HeLa Kyoto cells were co-transfected with pCHIV^{eGFP} and pCHIV wt in a 1:1 molar ratio. At 16 hpt, cells were treated with $1 \mu\text{M}$ of SiR-C6-RTV for 20 min prior to imaging. Cells were imaged by TIRF microscopy with a resolution of 0.2 frames/s for 2 h. A total of 250 tracks from 3 cells were analyzed. The Figure shows frames from movies recorded at the indicated time points for three individual sites that displayed an increase of fluorescence in both channels. Scale bars: $1 \mu\text{m}$. **B:** Plot of mean signal intensity of assembly sites of pCHIV^{eGFP} transfected HeLa Kyoto cells. Mean value and SD of Gag.eGFP fluorescence intensity over time, exhibiting saturating exponential assembly kinetics. $n=250$ assembly sites from 3 cells with exponential fit and mean rate constant. **C:** Plot of mean signal intensity of SiR-C6-RTV over

time for three representative assembly sites of pCHIV^{eGFP} transfected HeLa Kyoto cells. $t=0$ represents the first time point of assembly site detection (Gag.eGFP signal above background).

7 Discussion

While the importance of HIV-1 PR processing of Gag is known to be crucial for formation of infectious viral particles, the dynamic coordination of viral assembly and PR activity are not well understood. Approaches to disengage viral assembly and proteolytic processing, resulted in impaired viral infectivity and structural integrity (Mattei et al. 2014, Schimer et al. 2015). In this work, novel fluorescence-based probes were designed to detect PR activity and formation of active dimerized PR in real-time during the assembly process by fluorescence microscopy measurements.

7.1 Visualization of the assembly process by fluorescence microscopy

Our aim was to establish a temporal correlation between PR activation of proteolytic processing and the process of particle formation. PR activation and processing might theoretically occur during the assembly process, between completion of assembly and abscission or even after release has occurred. Previous analyses of Gag assembly kinetics had revealed that assembly is completed within an average of 8-9 min, followed by a 'stationary' period of ~ 10 min before particle abscission from the plasma membrane could be detected (Ivanchenko et al. 2009). In order to cover the whole process, it is thus necessary to observe individual assemblies over a minimum of 30 min following initial detection of the assembly with high time resolution. Quantitative analyses require kinetic data from a large number of individual assembly sites (> 100), and the appearance of individual sites at the membrane of a single cell is asynchronous; consequently, total observation periods in the range of 1 h or more are required for meaningful data collection.

Assembly kinetics were shown to differ between the ventral and lateral plasma membrane. A rate constant of $k = 5.9 \pm 0.4 \cdot 10^{-3} \text{ s}^{-1}$ was calculated for saturating exponential curves measured at the lateral plasma membrane, which was found to be faster than for the ventral plasma membrane ($k = 3.49 \pm 0.26 \cdot 10^{-3} \text{ s}^{-1}$; Mücksch et al. 2017). At the lateral plasma membrane, released particles diffused out of the field of view, so the fluorescence signal was lost and later timepoints could not be observed. Additionally, 3D z-stacks needed to be imaged to observe assembly at the lateral plasma membrane. Earlier studies revealed similar mean rate constants but described similar rate constants for ventral and lateral plasma membrane for saturating exponential curves. The complicated 3D imaging and tracking necessary for imaging of the lateral plasma membrane might cause variations in the assembly kinetics between lateral and ventral plasma membrane (Ivanchenko et al. 2009).

In order to reduce background from intracellular Gag and sensor proteins and to allow observation of viral particles after release, measurements were performed by TIRF microscopy at the ventral plasma membrane. In this case, viral particles are trapped between the cell and the glass surface, enabling longer time periods of viral detection, but making it more difficult to distinguish between late assembly sites and released virions (Ivanchenko et al., 2009, Jouvenet et al. 2008, Mücksch et al. 2017). Gag is known to be present as monomers and small oligomers in the cytoplasm (Kutluay und Bieniasz 2016; Hendrix et al. 2015). To detect Gag recruitment and the plasma membrane during early events of assembly would require single molecule sensitivity, that is not reached here. Therefore, no exact timeframes in relation

to the onset of the viral assembly process could be determined. This question is currently under investigation by our collaborators (AG Lamb, Munich).

In this study, the formation of newly produced viral particles at the plasma membrane of HeLa Kyoto cells was detected over 1 - 2 h by TIRF microscopy. Spots with an area of 4-40 pixels were observed to increase in fluorescence intensity over time. The kinetics of fluorescence signal intensity increase were analyzed by tracking the assembly sites and measuring the signal intensity over time. The observed assembly kinetics with saturating exponential curves were found to be comparable to published data (Ivanchenko et al. 2009, Jouvenet et al. 2008, Mücksch et al. 2017). Independent of the fluorescence tag, comparable rate constants of $\sim 3 \cdot 10^{-3} \text{ s}^{-1}$ were measured: SiR-SNAP, eGFP or eCFP inserted in Gag showed equal rate constants. Vpr.Clover revealed faster kinetics, which may be a result of recruitment of Vpr by Gag after the initiation of assembly site formation.

In the beginning of viral assembly, only few spots were detected on the plasma membrane and were therefore easily trackable. Over time, the number increased, and the buds became crowded, which complicated the tracking. These sites were excluded from the analysis. Trapping of released VLPs underneath the cell allowed the observation of viral particles for a longer time period and was utilized to detect later stages of viral particle. However, it complicated the discrimination between the viral budding and the pinching off process. To resolve this issue, other studies included fluorescently labeled components of the ESCRT machinery, which is recruited by Gag to perform the scission off the plasma membrane and induce viral particle release (Ivanchenko et al. 2009; Jouvenet 2012). Due to technical limitations in the detectable amount of fluorescence channels, these factors were not included in this study, but will be considered in future experiments.

7.2 Design of sensors to visualize HIV-1 PR activity during viral assembly by fluorescence microscopy

Different sensors were designed to enable the detection of proteolytic activity or formation of HIV-1 PR during viral assembly by fluorescence microscopy. They were based on physical characteristics of fluorescent proteins that changed depending on HIV-1 PR. Sensors depict PR activity, so it could be measured despite the resolution limit of fluorescence microscopy. Three different processes were detected: (i) proteolytic processing of an external sensor (ii) Gag processing and (iii) formation of active PR.

7.2.1 An external FRET-based sensor was specifically cleaved by HIV-1 PR

Fluorescence-based studies were applied to detect HIV-1 activity since the 1990s. Mostly, the measurements were conducted *in vitro*, e.g. with spectrofluorometry. In those studies, either purified proteins or viral particles were subject to proteolytic cleavage by purified HIV-1 PR (Baum et al. 1990, Gaber et al. 2012, Müller et al. 2014, Richards et al. 1990). However, concentrations of proteins in the cuvette might vary compared to native conditions in viral particles and protein accessibility might differ between soluble protein and protein incorporated in a viral particle. Therefore, these studies cannot fully be transferred to the viral process.

In other studies, different FRET-pairs like mCerulean and mCitrine or GFP and mCherry were applied to observe HIV-1 PR activity in cells (Gaber et al. 2012, Yang et al. 2012). mCerulean is excited with 405 nm, which was found to increase phototoxicity and is therefore not applicable for our approach (Hanne et al. 2016). In this work, fluorescent proteins Clover and mScarlet with high brightness and comparable folding kinetics were utilized as FRET pair to improve detection of fluorescence signal and reduce effect of maturation time of the proteins on FRET signal (Bindels et al. 2017, Lam et al. 2012).

In our FRET-based sensor, Clover and mScarlet were linked by the cleavage site located between MA and CA, defined as an intermediate processing site (Pettit et al. 1994). Sensor incorporation was achieved by linking the proteins to Vpr (Lampe et al. 2007). Proteolytic processing of the FRET-based sensor by wild-type HIV-1 PR reduced the FRET value by two-fold in purified VLPs. The FRET-based sensor was found to be not fully cleaved, as assessed by immunoblot analysis of purified VLPs. Since immunoblot analysis is a bulk approach, it does not allow distinction between a mixture of particles carrying different proportions of cleaved vs. uncleaved sensor, which can be caused e.g. by inactive PR in some virions, or a similar degree of incomplete cleavage in all particles. Incomplete cleavage might have been caused by inactive HIV-1 PR in individual viral particles or by variable amounts of incorporated sensor due to unequal incorporation. Furthermore, higher sensor concentration could result in high FRET values after PR processing due to molecular crowding even in the case of complete processing.

Previous experiments in our lab indicated that high amounts of incorporated Vpr.eGFP impaired Gag processing due to exogenous expression (Lampe et al. 2007). This was in line with the titration experiments in this work, which also showed that high amounts of incorporated sensor impede Gag processing.

Others described a FRET-based sensor utilizing YFP and mCherry coupled to Vpr and linked with two PR cleavage sites. Still, they observed impeded Gag and external FRET-based sensor processing to 55%, probably caused by too high amounts of sensor incorporation (Sood et al. 2017). In contrast, the study presented here, Gag processing rates of 80%, comparable to wild-type viral particles without exogenous Vpr were reached by careful titration of the FRET-based sensor in VLPs.

For the FRET-based sensor, which was incorporated in wild-type viral particles, plotting of the frequency distribution revealed a gaussian distribution of FRET values. These may be caused by the spatial arrangement of the fluorescent molecules, that influence the energy transfer efficiency. Energy transfer is only efficient, when the fluorescent proteins are aligned, so that the donor can induce an acceptor dipole. Protein alignment is subject to stochastic variations due to rotational diffusion (Vogel et al. 2012); this might lead to these observed variations of FRET efficiency.

Within cells, the co-expression of sensor and wild-type HIV-1 PR caused a two-fold decrease of the FRET values upon proteolytic processing of Clover-mScarlet.Vpr, whereas the frequency distribution revealed two populations, a mixture of mature and immature particles on the plasma membrane. While lower FRET values depict mature viral particles, early assembly sites and immature particles contained uncleaved FRET-based sensor and therefore result in higher FRET values, as shown for purified VLPs before. This might be due to asynchronous viral assembly in and between cells.

Due to cell-to-cell variation, cells might present different stages of assembly or the FRET-based sensor was not entirely cleaved by HIV-1 PR due to higher amounts of exogenous Vpr expressed in this cell (Lampe et al. 2007). Nevertheless, this twofold signal change was expected to be sufficient to detect proteolytic cleavage of the FRET-based sensor during viral assembly, since it was in line with literature (~ 30%; Gaber et al. 2012, Sood et al. 2017). In FRET literature, changes in the 5% range are accepted to confirm protein-protein interactions (Kuchenov et al. 2016). A FRET-based sensor containing mCerulean and Citrine was described to show a 25-35% drop of FRET signal due to HIV-1 PR in cells (Gaber et al. 2012). In this work, PR-dependent changes in FRET signal due to proteolytic processing up to 50% were detected in VLPs.

Albeit twofold differences in FRET signal in purified immature and mature particles, time-lapse measurements did not reveal changes in FRET signal as expected from still images of purified VLPs and assembly sites on the plasma membrane of HeLa Kyoto cells. Either, phototoxic effects impaired proteolytic activity, the cleavage did not happen in the observed timeframe or the process was decelerated. Phototoxic effects describe the side effects of laser excitation, that induces reactive oxygen species (ROS), which react with the proteins and can impair their functionality (Wright et al. 2002). Since active HIV-1 PR was detected in this study, formation of PR itself and therefore autoprocessing did not seem to be impaired. Additionally, TIRF microscopy features lower laser power, as well as lower sample penetration. This should decrease phototoxic effects and therefore generation of ROS. To test the impact of phototoxic effects and the timeframe, cells should be imaged with a fewer frames over a longer period of time (2-4 h). To further reduce phototoxicity, ROS could be tackled with scavengers like 4-hydroxy TEMPO (Żamoć et al. 2014).

Additional approaches were applied to accomplish the detection of proteolytic activity during the formation of viral particles.

7.2.2 Internal labeling of Gag for detection of Gag processing as a marker for PR activity

Different tags were inserted in Gag to observe Gag processing during viral assembly: (i) split fluorescent proteins, that should fluoresce upon proteolytic cleavage of Gag, (ii) a fluorogenic dye that can be applied to super-resolution microscopy and resolve changes in spatial distribution, and (iii) eCFP, that features changes in its fluorescence lifetime depending on localization in the Gag lattice or free diffusion in the viral particle.

7.2.2.1 Split fluorescent proteins and insertion in Gag does not enable distinction of mature and immature VLPs

Fluorescent proteins Venus and sfGFP were split into non-fluorescence subdomains (Hu and Kerppola 2003; Cabantous und Waldo 2006), incorporated in Gag between the MA and CA domain and designed to fluoresce upon Gag processing. The assumption was that constraint of the split subunits as internal part of a polyprotein that assembles into a stable and regular lattice (Sundquist und Kräusslich 2012) would prevent or at least hinder their association into

a functional fluorophore. PR-dependent Gag processing at one or both ends of the inserted subdomain should enable the fluorescent apoprotein to form, resulting in the appearance of a fluorescent signal. Upon co-expression of the two subdomains in viral particles, these subunits were able to reconstitute the fluorescent apoprotein. Emission of fluorescence signal was observed independent of proteolytic processing by HIV-1 PR, indicating that reconstitution of the split fluorescent protein subunits could occur within the context of the uncleaved polyprotein.

The immature Gag lattice is believed to be immobile and tight. A variable assembly would not allow to resolve the overall structure at resolutions as high as 8.8 Å (Briggs et al. 2009; Schur et al. 2015). In this case, it seemed that the overall flexibility was higher, or the assembly was disturbed by the insertion, but viral particles were nonetheless produced and released. These findings indicate that the particle assembly process by itself is robust and tolerates alterations of the Gag polyprotein, which are likely to disturb the regular molecular architecture of the lattice. Since the approach was found to be unsuitable for the intended purpose, the architecture of the resulting virions was not further analyzed.

7.2.2.2 Changes in localization of fluorescence tags in Gag can be visualized by STED microscopy

Next, changes in localization of fluorescence tags in Gag were visualized by STED microscopy. The insertion of the Clip tag in Gag between MA and CA and flanked by PR cleavage sites (pCHIV^{iClip}), combined with the increased resolution of STED microscopy enabled a discrimination of mature and immature viral particles. For purified VLPs, this was shown previously (Hanne et al., 2016). Here, pCHIV^{iClip} was applied to visualize immature rings and mature blob-like structures at the plasma membrane of HeLa Kyoto cells.

STED microscopy was applied to resolve late stages of viral assembly, that could not be visualized by confocal microscopy. Patches, as observed during live-cell imaging of the assembly process, were discovered to harbor numerous (~50-100) late budding sites or released viral particles trapped underneath the cells. For pCHIV^{iClip} expressing wild-type HIV-1 PR, conformational changes of the tag upon proteolytic processing were detected. A mixture of ring- and blob-like structures was observed. Ring-like structures depicted late stages of assembly and budding, as well as immature viral particles, while mature particles were detected as “blobs”. The resolution enabled distinguishing of individual viral particles even in this crowded environment. The presence of ring- and blob-like structures validated the onset of proteolytic processing of Gag during this stage of assembly. The mixture also indicated an asynchronous assembly of viral particles on one cell.

Proteolytic activity was reported to be impaired by the phototoxic effects of the STED laser. Hanne et al. (2016) visualized maturation of purified viral particles upon PR activation. This process was locally hindered after imaging of viral particles by STED microscopy in the field of view. Here, 4-Hydroxy-TEMPO was applied to detoxify ROS to reduce phototoxicity and improve proteolytic processing (Żamojć et al. 2014).

Although the mature and immature structures were resolved at assembly sites by STED microscopy, measuring dynamic processes of PR activity during the viral assembly was not performed with this system. Imaging cells for multiple frames was observed to induce cell

death. Time-lapse measurements of assembly sites were discussed to impair Gag processing at the imaged site and therefore not pursued further. Now, a new method was described to allow nm resolution with a minimal amount of photons (MINFLUX) (Balzarotti et al. 2017). With this method, measurements at late stages of assembly might allow the visualization of conformational redistribution of the Clip-tag from the ring- to the blob-like structure.

7.2.2.3 Changes in fluorescence lifetime of eCFP in Gag can be visualized by FLIM microscopy

FLIM measurements are often applied to measure FRET efficiency, mostly of hetero-FRET pairs. The application of hetero-FRET pairs can change the ratio of incorporated fluorescent proteins in Gag (Müller et al. 2014). Here, eCFP was utilized for FLIM measurements, because it employs homo-FRET, which reduces the influence of protein incorporation (Poëa-Guyonet et al. 2013). For FLIM measurements, signal intensity can be taken out of the equation, therefore this method is more robust than FRET measurements (Suhling et al. 2015). This reduced the influence of bleaching on this system. The microscope set-up of our collaborators (AG Lamb, Munich) was specifically designed for improved eCFP signal and fluorescence lifetime detection. Lifetime quantification algorithms were developed by this group, allowing most precise calculations based on phasor analysis (Digman et al. 2008).

To detect Gag processing, eCFP was inserted in Gag in between MA and CA. It was either flanked by PR cleavage sites to freely diffuse in the particle upon proteolytic processing (ieCFP) or featured with one clipping site to stay linked to MA and merely rearrange on the viral membrane after PR dependent cleavage (eCFP). Molecular crowding of Gag induced homo-FRET of eCFP in the Gag lattice, resulting in a decrease of fluorescence lifetime (Kremers et al. 2006).

Proteolytic processing induced an increase of fluorescence lifetime. In VLPs, freely diffusing eCFP of pCHIV^{ieCFP} featured a two-fold higher increase in fluorescence lifetime than MA-eCFP. Molecular crowding of eCFP in the small volume of a VLP did not impact its fluorescence lifetime, because values were comparable to freely diffusion of eCFP in the cytoplasm of HeLa Kyoto cells. Either, MA induced clustering of the molecules in the cytoplasm, leading to a decrease in fluorescence lifetime, or the coupling changed the properties of eCFP. DNA-origami experiments with controlled formation of MA-eCFP multimers or monomers would need to be conducted to shed light on this question.

Live-cell imaging performed with higher time resolution allowed tracking of individual assembly sites. While they revealed signal intensity increase of eCFP with the saturation exponential assembly kinetics as described earlier, only slight changes in fluorescence lifetime were observed for four out of 100 analyzed tracks. This was in line with the bulk analysis but did not allow a detection of proteolytic processing of Gag during the assembly process. Either, cytosolic background precluded observation of changed in fluorescence lifetime, or laser phototoxicity hindered proteolytic processing of Gag by HIV-1 PR.

While TIRF measurements were mostly applied to live-cell imaging of viral assembly, FLIM measurements were conducted by confocal imaging due to technical restrictions. The increased sample penetration of 200 nm to 500 nm, enhanced the influence of cytoplasmic background signal (Balagopalan et al. 2011; Mattheyses et al. 2010). This might affect the

FLIM measurements and decrease the overall changes that could be detected due to the presence of Gag.eCFP in the cytoplasm. Additionally, phototoxic effects might have impaired or reduced HIV-1 PR activity. To reduce phototoxicity, ROS could be tackled with scavengers like 4-hydroxy TEMPO (Žamojć et al. 2014).

For the four detected assembly sites, an increase of fluorescence lifetime was observed after about 15-20 min. Studies that observed Gag processing after inducing PR activity, report a $t_{1/2}$ of 30 min for this process (Mattei et al. 2014; Schimer et al. 2015; Hanne et al. 2016). As discussed before, uncoupling of Gag assembly and proteolytic processing might alter PR cleavage activity. Detection of Gag processing during the assembly process would suggest faster processing in the nascent viral particle compared to the induced measurements.

Further imaging of time-lapse experiments will be conducted for this project. First, measurements will be conducted in presence on 4-hydroxy TEMPO to reduce influence of ROS. Alternatively, a TIRF-FLIM set-up should be considered for imaging to reduce phototoxicity and cytoplasmic background. An improvement of tracking and lifetime quantification is ongoing in collaboration with AG Lamb.

7.2.3 Formation of active HIV-1 PR was detected during the viral assembly process

The last approach tested in this work was the detection of formation of active HIV-1 PR during the viral assembly process. The PR inhibitor RTV, which binds to the active site of the PR dimer, was coupled to the fluorogenic probe SiR.

Detection of intracellularly expressed proteins by fusion of the protein of interest to a SNAP- or Clip-tag, followed by covalent adduction of a fluorogenic dye like silicone-rhodamine (SiR) to the self-labeling tag is well established (Reymond et al. 2011). The equilibrium of SiR between a non-fluorescence lactonic and fluorescence zwitterion structure is sensitive to hydrophobic effects (Lukinavičius et al. 2013). The dye substrate has been optimized to yield high fluorogenicity when bound to SNAP or Clip, and the covalent nature of the resulting complex allows for extensive washing to reduce cellular background in live-cell experiments. This results in a high sensitivity of detection, which easily allowed to follow assembly of Gag.SNAP carrying particles at the cell membrane. Staining of Gag.SNAP and Gag-Clip expressing viral particles with SNAP-Cell 647-SiR and SiR-Clip respectively was previously described (Eckhardt et al. 2011, Hanne et al. 2016). Labeled Gag was successfully observed, because in a viral particle, there are ~2500 Gag molecules. Only ~ 60 PR dimers are incorporated per virion; therefore the detection is more challenging (Sundquist and Kräusslich 2012).

The innovative concept of intracellular protein labeling by transient binding of a SiR-coupled inhibitor derivative has been established for cytoskeletal filaments F-actin and microtubule (Lukinavičius et al. 2014). These structures are characterized by a very high number and density of monomeric subunits and are therefore frequently used as exemplary targets for the validation of novel staining or microscopic approaches. The application of the principal approach to a more challenging target had not been described.

HIV-1 PR is known to be highly affected by mutations and due to its small size (10 kDa), direct labeling of PR was not accomplished without impairing virus infectivity, even with small TC-

tags (Pereira et al. 2011). While tagging PR directly cannot discriminate monomeric PR in GagProPol and dimeric active PR, we specifically designed our probe to detect active HIV-1 PR.

SiR-RTV was shown to fluoresce upon binding to the PR active site due to conformational changes in SiR depending on the environment. Different carbon linkers were tested for optimal fluorogenicity of SiR, carrying either two (SiR-C2-RTV), four (SiR-C4-RTV) or six (SiR-C6-RTV) carbon molecules.

Detection of emission spectra revealed unspecific turn-on upon addition of 0.1 mg/ml BSA in PBS for SiR-C2-RTV and SiR-C4-RTV, while SiR-C6-RTV showed only a weak signal intensity increase in the presence of BSA *in vitro*. A longer linker therefore seemed to increase specificity of the probes, while a shorter linker increased maximum fluorescence intensity. It should be noted, however, that the addition of BSA *in vitro* is a rather simplified correlate of interactions that may occur in the cytosol of a virus producing cell.

Although fluorescence signal at assembly sites was threefold higher for SiR-C4-RTV than for SiR-C6-RTV, which might have improved early detection of fluorescence signal, the high unspecific background signal for SiR-C4-RTV impaired the recognition of specific signals. For assembly sites containing the wild-type HIV-1 PR, a specific signal of threefold above background was observed for SiR-C6-RTV. Covalent binding of SNAP-Cell 647-SiR to the SNAP-tag increased the fluorogenicity by 10-20-fold (Lukinavičius et al. 2013), a 10-fold higher SNAP-Cell 647-SiR signal intensity was detected at assembly sites expressing Pol-SNAP compared to SiR-C6-RTV.

Live cell imaging of pCHIV^{eGFP} carrying wild-type PR revealed specific SiR signal at Gag.GFP assembly sites in the presence of 1 μ M SiR-C6-RTV during the assembly process over 2 – 4 h. Analysis of pCHIV^{eGFP} assembly kinetics resulted in saturating exponential curves with rate constants as described above. According to literature, viral assembly takes ~10 min, while the viral particle is released after ~20 min (Ivanchenko et al. 2009).

To detect formation of active PR during the viral assembly process, SiR-C6-RTV needed to remain in the supernatant. While this led to an unspecific background, a specific signal was nevertheless detected during viral assembly at the plasma membrane. SiR signal increase was observed to be either (i) early, (ii) late or (iii) fluctuating. Early signal increase was detected after 10 - 20 min, suggesting PR activation during late stages of the viral assembly process. Later events were observed after ~40 min, indicating formation of active PR after viral release. Due to high background signal, fluctuations of the SiR signal hindered detection of specific fluorescence signals for a large fraction of assembly sites. Detailed quantification of the early and late SiR signal during the viral assembly process will be pursued. Overall, SiR-C6-RTV was able to detect formation of active HIV-1 PR during the viral assembly process despite the small amount of ~60 molecules of active HIV-1 PR in viral particle. The threefold signal increase suggests a detection limit of ~20 bound SiR-C6-RTV molecules with this experimental set-up.

7.3 Future implications of the project

Detection of proteolytic activity during the viral assembly process was not feasible in this study but labeling of active HIV-1 PR by a fluorogenic probe was successfully established. In this work, I have successfully established time-resolved detection of active HIV-1 PR in relation to the Gag assembly process.

So far, Gag assembly kinetics were used as markers for the stage of viral assembly. The determination of exact timing of formation of active PR in regard to viral release was not shown but would be a crucial clue concerning further studies of PR activation. Regulation of PR activity by its monomeric expression and a likely activation after closing of the viral particle is known, but the exact timing in relation to virus release still remains elusive (Konvalinka et al. 2015). The p6 domain of Gag is known to recruit the cellular ESCRT machinery to facilitate scission of the viral particle from the plasma membrane. It interacts with Tsg101 and ALIX, which then recruit ESCRT-III. ESCRT-III has been observed to assemble into spirals at the neck of the bud. It has been shown to recruit the AAA ATPase vacuolar protein sorting 4 (Vps4), which enables membrane scission and recycles ESCRT components after budding has been completed (Freed 2015). Timing of ESCRT recruitment in relation to Gag assembly was shown previously (Ivanchenko et al. 2009; Jouvenet et al. 2012, Johnson et al. 2018). The ATPase Vps4 was reported to appear at the assembly site shortly before scission of the viral particle off the plasma membrane. Correlation of Vps4 recruitment and detection of active HIV-1 PR would reveal the mystery of timing of PR formation before or after virus release.

A longer linker between the RTV and SiR seemed to improve functionality of both compounds. This suggests that a C8 linker may further increase the specificity of the probe. Testing of additional probes was beyond the scope of this work but should be approached in the future.

8 Abbreviations

λ	wavelength
τ	fluorescence lifetime
$^{\circ}\text{C}$	degrees Celsius
3D	three dimensional
a.u.	arbitrary units
A	adenosine
AA	amino acid
AIDS	acquired immune deficiency syndrome
ALIX	apoptosis-linked gene-2 interacting protein 1/X
APS	ammonium persulfate
BSA	bovine serum albumin
bp	base pair
CA	capsid protein
cART	combined antiretroviral therapy
CCR5	CC chemokine receptor 5 – HIV-1 coreceptor
CD	cluster of differentiation
CD4 ⁺ T cell	T cell positive for CD4
CXCR4	CXC chemokine receptor 5 – HIV-1 coreceptor
DMEM	Dulbecco's Modified Eagle Medium
DMSO	dimethyl sulfoxide
DNA	desoxyribonucleic acid
dNTP	deoxynucleoside triphosphate
eCFP	enhanced cyan fluorescent protein
EDTA	Ethylenediaminetetraacetic acid
eGFP	enhanced green fluorescent protein
em	emission
EM	electron microscopy
Env	envelope protein
ER	endoplasmic reticulum
ESCRT	endosomal sorting complexes required for transport
EtOH	ethanol
ex	excitation
FACS	fluorescence-activated cell sorter
FCS	fetal calf serum
FLIM	fluorescence lifetime imaging microscopy
FRAP	fluorescence recovery after photobleaching
FWHM	full width at half maximum
G	guanine
Gag	group specific antigen
GFP	green fluorescent protein
golgi	golgi apparatus
gp 41	glycoprotein 41(kDa size)
h	hour
H ₂ O	water
HBR	highly basic region

HIV	human immunodeficiency virus
hpt	hours post transfection
kb	kilo bases
KCl	potassium chloride
kDa	kilo dalton
l	liter
LB-media	Luria-Bertani media
LPV	lopinavir
LTR	long terminal repeat
LUT	look-up table
MA	matrix protein
mCherry	monomeric cherry fluorescent protein
MeOH	methanol
mg	milligram
MgCl ₂	magnesium chloride
min	minutes
mM	millimolar
ml	milliliter
mRNA	messenger RNA
myr	myristoyl
NA	numerical aperture
NaCl	sodium chloride
NC	nucleocapsid protein
Nef	negative factor
nm	nanometer
nM	nanomolar
ORF	open reading frame
p6	protein 6 (kDa size)
PBS	phosphate buffered saline
PCR	polymerase chain reaction
PEI	polyethylenimide
PI(4,5)P ₂	phosphatidylinositol-4,5-bisphosphate
PIC	pre-integration complex
PM	plasma membrane
Pol	polymerase
PR	protease
RNA	ribonucleic acid
rpm	rotation per minute
RT	reverse transcriptase
RTC	reverse transcription complex
s	seconds
SD	standard deviation
SDS-PAGE	sodium dodecyl sulfate polyacrylamide gel electrophoresis
SEM	standard error of the mean
sfGFP	superfolder green fluorescent protein
SiR	silicone rhodamine
SP1	spacer peptide 1
SP2	spacer peptide 2
STED	stimulated emission depletion

t	time
Tat	trans-activator of transcription
TC-tag	tetracystein tag
TEMPO	tetramethylpiperidinyloxy
TFR	trans-frame region
TIRF	total internal reflection fluorescence
Tsg101	tumor susceptibility gene 101
U	units
V	volt
Vif	viral infectivity factor
VLP	virus-like particle
Vpr	viral protein r
Vps4	vacuolar protein sorting protein 4
Vpu	viral protein u
w/v	weight/volume
WB	western blot
wt	wild-type
YFP	yellow fluorescent protein
µg	microgram
µl	microliter
µm	micrometer

9 Index

Fig. 1: HIV-1 genome and particle structure.	10
Fig. 2: Gag and GagProPol processing and formation of a mature viral particle	11
Fig. 3: Schematic replication cycle of HIV-1.....	13
Fig. 4: Schematic representation of assembly, budding and maturation of HIV-1	14
Fig. 5: Structure of HIV-1 PR	16
Fig. 6: Substrate interaction with the catalytic residues.....	16
Fig. 7: Schematic representation of the mechanism of proteolytic cleavage.	17
Fig. 8: Autocatalysis of HIV-1 PR from GagProPol	18
Fig. 9: Gag cleavage sites and order of proteolytical processing events.....	19
Fig. 10: Specific PR cleavage sites in GagProPol.....	20
Fig. 11: PR inhibitor bound to the active site of HIV-1 PR.....	21
Fig. 12: Selected PR inhibitor structures and respective kinetic parameters for binding to the active site of HIV-1 PR	21
Fig. 13: Virus-like particles can be visualized via incorporated fluorescent proteins.....	51
Fig. 14: Double labeling of viral particles and assembly sites	52
Fig. 15: LSC and TIRF microscopy of SNAP-Cell 647-SiR labeled particles and assembly sites.....	53
Fig. 16: Live-cell imaging of the assembly process at the plasma membrane of HeLa Kyoto cells by TIRF microscopy	55
Fig. 17: Assembly kinetics of pCHIV ^{SNAP} and pCHIV with pClover.Vpr.....	56
Fig. 18: Sensor incorporation and analysis of PR dependent sensor and Gag cleavage in virus-like particles (VLPs).....	58
Fig. 19: Analysis of PR dependent FRET signal changes in virus-like particles (VLPs)	60
Fig. 20: Effect of sensor plasmid titration on bulk processing efficiency.....	62
Fig. 21: Quantification of intracellular HIV-1 PR activity by FACS FRET.....	63
Fig. 22: Maximum FRET efficiency detected by increase of donor signal intensity upon acceptor photobleaching.	65
Fig. 23: Fluorescence recovery after photobleaching detected by TIRF microscopy.....	66
Fig. 24: PR dependent FRET changes detected at HIV-1 Gag assembly sites by TIRF microscopy	68
Fig. 25: Maturation of viral particles not detectable with split systems of fluorescent proteins.	71
Fig. 26: Discrimination of mature and immature virus-like particles by STED microscopy.....	72
Fig. 27: Virus-like particles ± LPV assemble at the plasma membrane of HeLa Kyoto cells..	73
Fig. 28: Immature viral particles assemble at the plasma membrane of HeLa Kyoto cells	74
Fig. 29: Virus-like particles assemble at the plasma membrane of HeLa Kyoto cells in the absence of LPV	75
Fig. 30: Analysis of proteolytic processing of Gag.ieCFP and Gag.eCFP by immunoblot	76
Fig. 31: Measurements of fluorescence lifetime of eCFP in purified VLPs	77
Fig. 32: Measurements of fluorescence lifetime of eCFP in HeLa Kyoto cells.....	79
Fig. 33: Lifetime distribution comparing immature (+LPV) and mature (-LPV) assembly sites at the plasma membrane of HeLa Kyoto cells	80
Fig. 34: Lifetime distribution of assembly sites during particle formation over time	81
Fig. 35: Changes in eCFP fluorescence lifetime during viral assembly	82
Fig. 36: Design of a fluorogenic probe to detect active PR	83
Fig. 37: Spectrophotometric analysis of SiR-C2-RTV	86

Fig. 38: Spectrophotometric analysis of SiR-C4-RTV	87
Fig. 39: Spectrophotometric analysis of SiR-C6-RTV	88
Fig. 40: PR-dependent SiR-RTV signal detected at HIV-1 Gag assembly sites by TIRF microscopy	89
Fig. 41: PR-dependent SiR signal detected at HIV-1 Gag assembly sites by TIRF microscopy.	92
Fig. 42: Live-cell imaging of SiR-C6-RTV fluorescence signal during the viral assembly process	93

10 Publications and contributions

10.1 Publications

Mattei, Simone; **Flemming, Annica**; Anders-Össwein, Maria; Kräusslich, Hans-Georg; Briggs, John A. G.; Müller, Barbara (2015): RNA and Nucleocapsid Are Dispensable for Mature HIV-1 Capsid Assembly. In: *Journal of virology* 89 (19), S. 9739–9747. DOI: 10.1128/JVI.00750-15.

10.2 Conference contributions

Annica Flemming, Vibor Laketa, Ulrike Engel and Barbara Müller

Poster presentation: Design and Characterization of a Bright and Fast-Maturing FRET-based Sensor to Monitor HIV-1 Protease Activity using Live-Cell Imaging

Retroviruses, Cold Spring Harbor Laboratory, NY, USA, 2018

Annica Flemming, Vibor Laketa, Hans-Georg Kräusslich, Karl Rohr and Barbara Müller

Poster presentation: Investigating Dynamics of HIV-1 Protease Activity During Viral Assembly

Retreat SFB 1129, July 2016

Annica Flemming, Barbara Müller

Oral presentation: Investigating Dynamics of HIV-1 Protease Activity

HBIGS Retreat, June 2016

10.3 Contributions to this project

All data shown in this thesis was acquired and analyzed by me, if not stated otherwise. Contributions to this thesis are described as follows:

Vibor Laketa gave substantial input on imaging and data analysis.

Ulrike Engel (Nikon Imaging Center, Heidelberg) gave advice regarding imaging and analysis of TIRF data.

Janina Hanne provided SiR-Clip dye used in STED experiments and helped with STED image acquisition.

Susann Kummer helped with STED image acquisition and image analysis.

Maria Anders-Össwein helped with cloning of pCHIV^{NC-RT} and provided the western blot shown in Fig. 21.

Don Lamb (LMU Munich) provided substantial input on all aspects of this thesis especially experiments involving FLIM measurements of eCFP and analyses and supervised the project.

Chen Quian (AG Lamb, LMU Munich) provided substantial input on the FLIM project, performed the FLIM measurements with me and analyzed the lifetime values by phasor analysis.

Jan Konvalinka (Prague, Czech Republic) provided substantial input in the project to detect active PR during viral assembly.

Jiri Schimer (Prague, Czech Republic) synthesized all tested fluorogenic PR inhibitors, SiR-C2-RTV, SiR-C4-RTV and SiR-C6-RTV and provided the purified HIV-1 PR.

Hans-Georg Kräusslich supervised the project and provided substantial input on all aspects of this thesis.

Barbara Müller conceptualized and supervised the project and provided substantial input on all aspects of this thesis.

11 Acknowledgements

An intense and versatile project such as this requires many people in order to be successful, whom I would like to thank very dearly.

First of all, I want to thank Barbara Müller to give me the opportunity to pursue this imaging-based project in her group despite my lack of experience with microscopes and the continuous support and discussions throughout the work. Thank you for detailed corrections of project plans, as well as this work in order to help me find the key.

Thanks to Hans-Georg Kräusslich for his help to bring the projects back on track when I got lost in details. Thank you for examining my thesis and support as member of my TAC and defense committee.

I would like to thank Jacomine Krijnse Locker for supporting me as a TAC member, as well as my referee for this thesis. Thank you for your commitment beyond state lines.

Thank you to Marina Lusic and Freddy Frischknecht for being part of my defense committee.

Thanks to Mike Heilemann and Dirk-Peter Herten for their input concerning fluorescence microscopy as members of my TAC.

Thanks to my collaborators Don Lamb, Viola Baumgärtel, Chen Quian and Philipp Messer in Munich and Jan Konvalinka and Jiri Schimer in Prague, for your valuable work and input in this work to bring the projects forward. Special thanks goes to Jiri, for synthesizing new compounds all over the world. Thank you to Ulrike Engel from NIC for making sure that I never throw the microscope against the wall.

Thank you to the whole AG Müller: Maria, Volkan, Renè, Sandra and Mama Anke (yes, in my heart we still share the same group 😊). Thank you for teaching me and taking time to help me, even for crazy trips to the airport. Thank you all for being such a great team.

Thanks to my practical students Franzi, Isabel and Jonas for sharing my enthusiasm for the project and their help to drive it forward.

I would like to thank Vibor Laketa to opening the door to the amazing world of microscopy for me. Your immense experience and awesome excitement for imaging and image analysis was invaluable for me and this work.

Thank you to everyone in the Virology department of being amazing colleagues and helping out with any issue. Special thanks to Frauke, Janina, Walter, Vojtech, Andrea and Bärbel for help with cells, dyes, microscopes and protocols.

Amazingly, there are many colleagues who became friends over time. Thank you, Susann for our therapeutic running sessions. I am looking forward to start them again. Thanks to Anja and Thorsten who push me to become a Viech and believe in me. Janina, thank you for being my coach in the beginning of the thesis and for work-outs. Juliane, thank you for teaching me how to eat wraps. Sarah, thank you for your help on such short notice.

Special thanks goes to Robin for being a friend from the start and making me feel welcome. Your detailed corrections throughout my work helped me improve and were appreciated tremendously. Meanwhile, various cooking and drinking sessions will not be forgotten.

Thank you to the AIDS-Hilfe Heidelberg for showing me the value and meaning of my work in HIV research and for giving me the opportunity to have an impact.

My deepest gratitude goes to my family and friends, who supported me along the whole way and believed in me. Mostly to my parents, who put up with anything to help me succeed and building me up when it was needed. Thanks to my brother and his little family, all my grandparents, aunts and uncles and cousins for your support.

Anni and Andi, thank you for giving me a home during my stays in Munich for the collaborations, and also for the care package to help me survive the writing process.

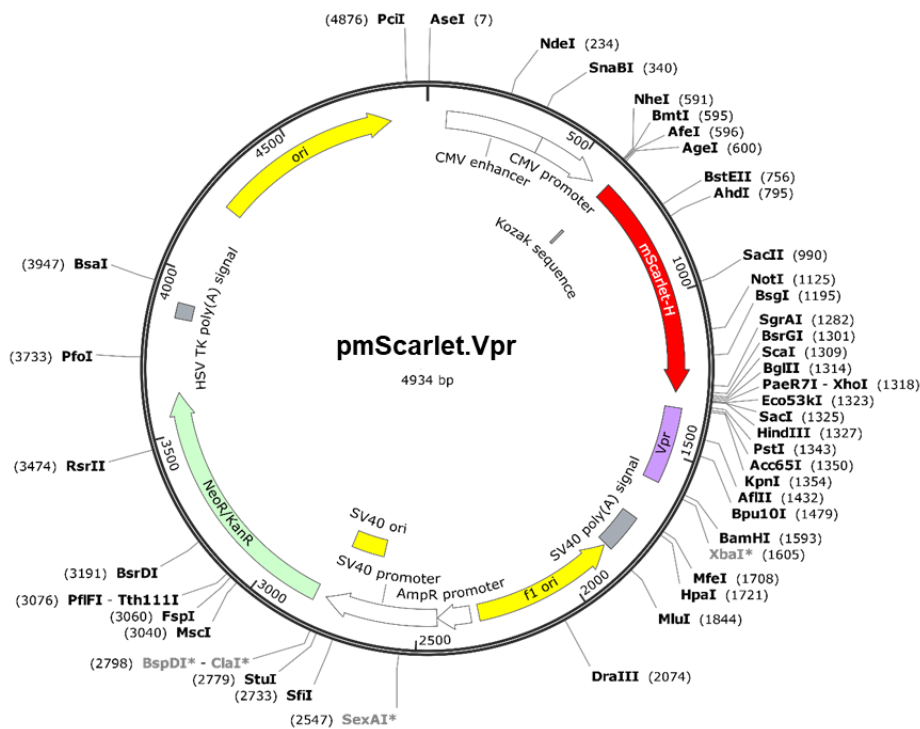
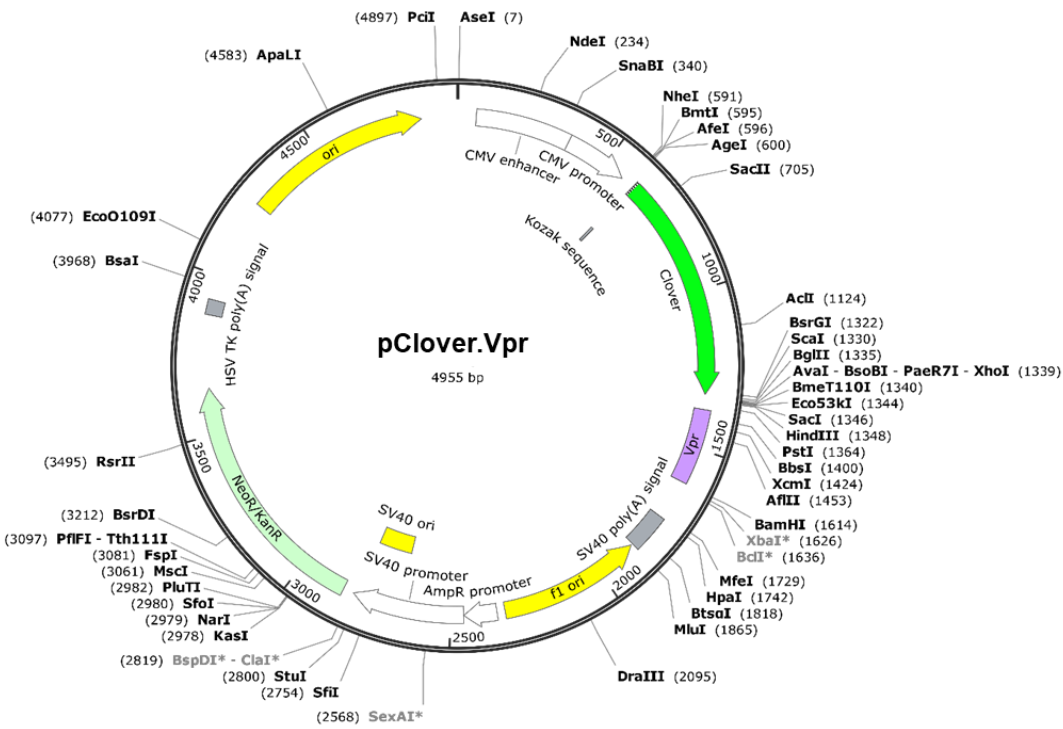
Juliane for being my roommate for so long and spoiling me with amazing treats over the time. Thank you for taking the discussion of this thesis apart.

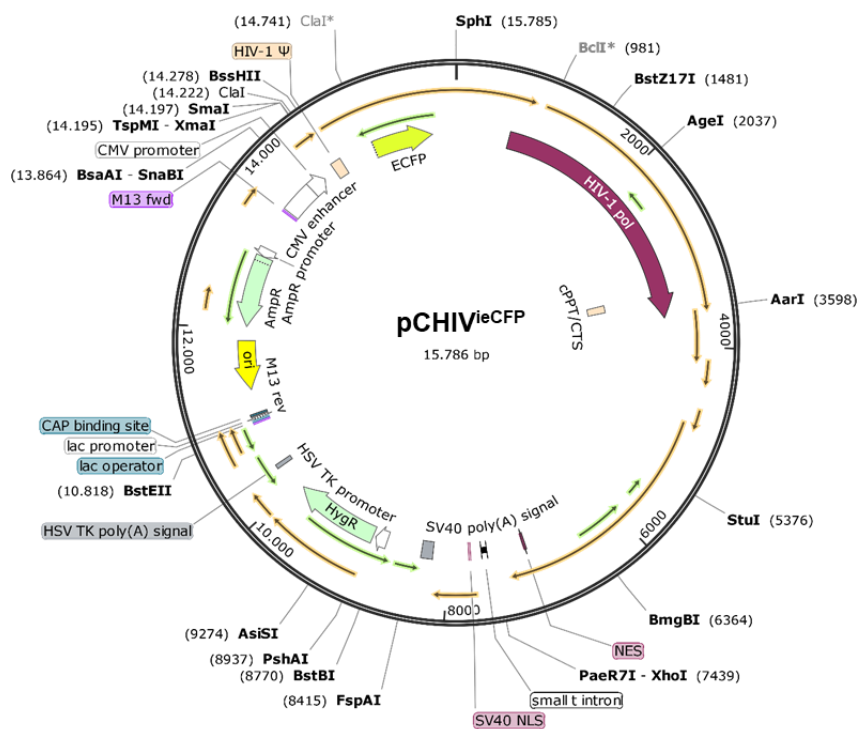
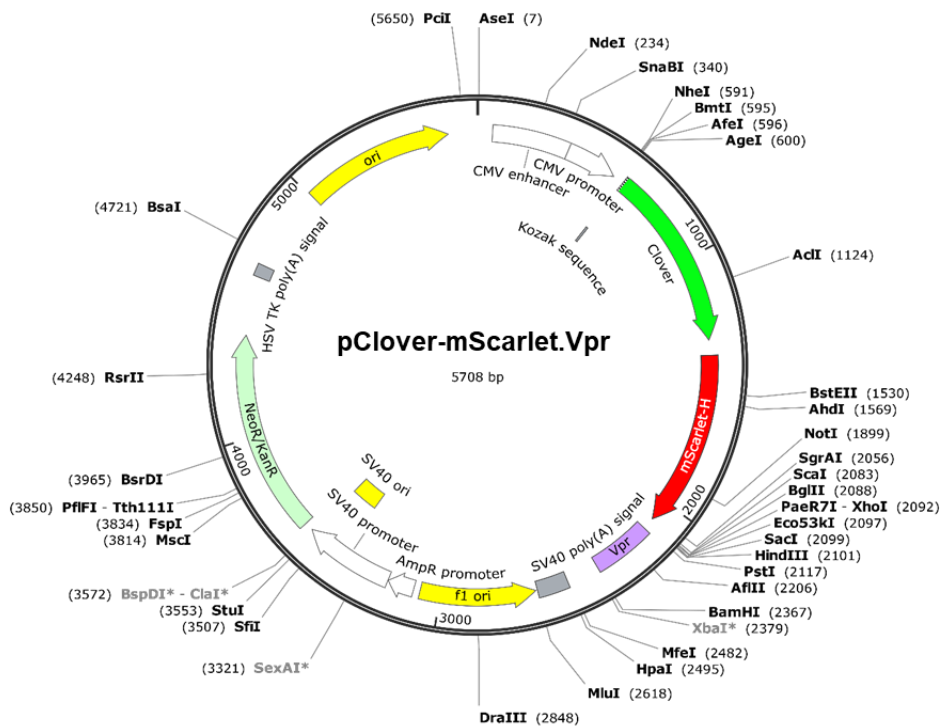
Elli, now I don't know where to start to thank you. You helped to keep me sane over the last years by being an amazing friend. Thank you for taking all this time to proof-read my thesis and setting my head right.

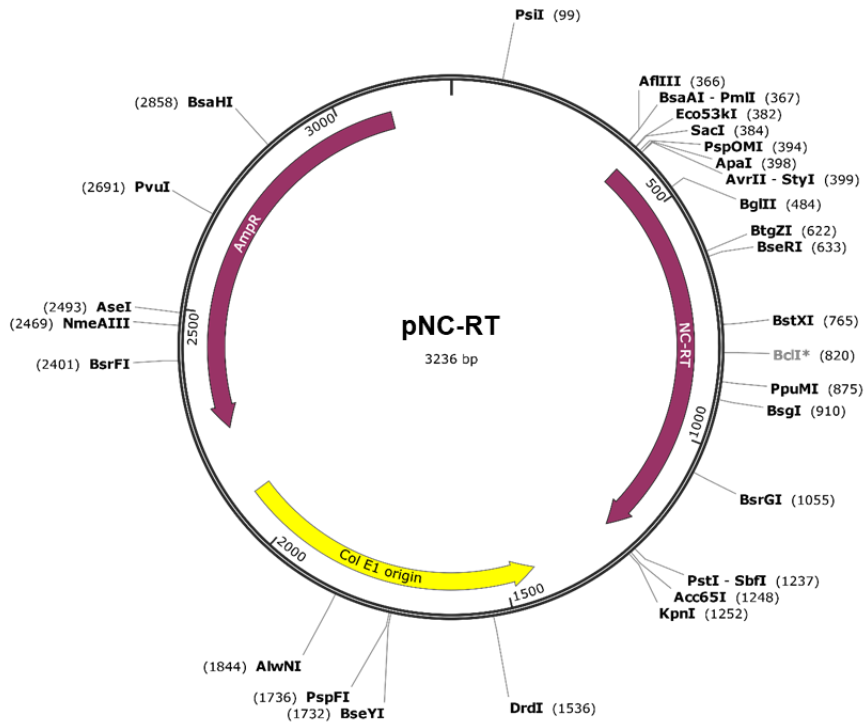
Thank you to Katrin, Mara and Conny for listening and reminding me of the world besides this work.

I could not have done it without all of you.

12 Plasmid Maps







13 References

- Accola, Molly A.; Strack, Bettina; Göttlinger, Heinrich G. (2000): Efficient Particle Production by Minimal Gag Constructs Which Retain the Carboxy-Terminal Domain of Human Immunodeficiency Virus Type 1 Capsid-p2 and a Late Assembly Domain. In: *Journal of virology* 74 (12), S. 5395–5402.
- Balagopalan, Lakshmi; Ashwell, Benjamin A.; Bernot, Kelsie M.; Akpan, Ito O.; Quasba, Naeha; Barr, Valarie A.; Samelson, Lawrence E. (2011): Enhanced T-cell signaling in cells bearing linker for activation of T-cell (LAT) molecules resistant to ubiquitylation. In: *Proceedings of the National Academy of Sciences of the United States of America* 108 (7), S. 2885–2890. DOI: 10.1073/pnas.1007098108.
- Banning, Carina; Votteler, Jörg; Hoffmann, Dirk; Koppensteiner, Herwig; Warmer, Martin; Reimer, Rudolph et al. (2010): A flow cytometry-based FRET assay to identify and analyse protein-protein interactions in living cells. In: *PloS one* 5 (2), e9344. DOI: 10.1371/journal.pone.0009344.
- Barré-Sinoussi, F.; Chermann, J. C.; Rey, F.; Nugeyre, M. T.; Chamaret, S.; Gruest, J. et al. (1983): Isolation of a T-lymphotropic retrovirus from a patient at risk for acquired immune deficiency syndrome (AIDS). In: *Science (New York, N.Y.)* 220 (4599), S. 868–871.
- Baum, E. Z.; Beberitz, G. A.; Gluzman, Y. (1990): beta-Galactosidase containing a human immunodeficiency virus protease cleavage site is cleaved and inactivated by human immunodeficiency virus protease. In: *Proceedings of the National Academy of Sciences of the United States of America* 87 (24), S. 10023–10027.
- Baumgärtel, Viola; Ivanchenko, Sergey; Dupont, Aurélie; Sergeev, Mikhail; Wiseman, Paul W.; Kräusslich, Hans-Georg et al. (2011): Live-cell visualization of dynamics of HIV budding site interactions with an ESCRT component. In: *Nature cell biology* 13 (4), S. 469–474. DOI: 10.1038/ncb2215.
- Baumgärtel, Viola; Müller, Barbara; Lamb, Don C. (2012): Quantitative live-cell imaging of human immunodeficiency virus (HIV-1) assembly. In: *Viruses* 4 (5), S. 777–799. DOI: 10.3390/v4050777.
- Bendjennat, Mourad; Saffarian, Saveez (2016): The Race against Protease Activation Defines the Role of ESCRTs in HIV Budding. In: *PLoS pathogens* 12 (6), e1005657. DOI: 10.1371/journal.ppat.1005657.
- Berg, Jeremy M.; Tymoczko, John L.; Stryer, Lubert; Gatto, Gregory J. (2014): Biochemie. 7. Auflage, korrigierter Nachdruck. Berlin, Heidelberg: Springer Spektrum (Lehrbuch).
- Bieniasz, Paul D. (2009): The cell biology of HIV-1 virion genesis. In: *Cell host & microbe* 5 (6), S. 550–558. DOI: 10.1016/j.chom.2009.05.015.
- Bindels, Daphne S.; Haarbosch, Lindsay; van Weeren, Laura; Postma, Marten; Wiese, Katrin E.; Mastop, Marieke et al. (2017): mScarlet: a bright monomeric red fluorescent protein for cellular imaging. In: *Nature methods* 14 (1), S. 53. DOI: 10.1038/nmeth.4074.
- Bleck, Marina; Itano, Michelle S.; Johnson, Daniel S.; Thomas, V. Kaye; North, Alison J.; Bieniasz, Paul D.; Simon, Sanford M. (2014): Temporal and spatial organization of ESCRT protein recruitment during HIV-1 budding. In: *Proceedings of the National Academy of*

- Sciences of the United States of America* 111 (33), S. 12211–12216. DOI: 10.1073/pnas.1321655111.
- Briggs, John A. G.; Riches, James D.; Glass, Bärbel; Bartonova, V.; Zanetti, G.; Kräusslich, Hans-Georg (2009): Structure and assembly of immature HIV. In: *Proceedings of the National Academy of Sciences of the United States of America* 106 (27), S. 11090–11095.
- Briggs, John A.G.; Wilk, Thomas; Welker, Reinhold; Kräusslich, Hans-Georg; Fuller, Stephen D. (2003): Structural organization of authentic, mature HIV-1 virions and cores. In: *The EMBO journal* 22 (7), S. 1707–1715. DOI: 10.1093/emboj/cdg143.
- Bushman, F. D.; Fujiwara, T.; Craigie, R. (1990): Retroviral DNA integration directed by HIV integration protein in vitro. In: *Science (New York, N.Y.)* 249 (4976), S. 1555–1558.
- Cabantous, Stéphanie; Terwilliger, Thomas C.; Waldo, Geoffrey S. (2005): Protein tagging and detection with engineered self-assembling fragments of green fluorescent protein. In: *Nature biotechnology* 23 (1), S. 102–107. DOI: 10.1038/nbt1044.
- Cabantous, Stéphanie; Waldo, Geoffrey S. (2006): In vivo and in vitro protein solubility assays using split GFP. In: *Nature methods* 3 (10), S. 845–854. DOI: 10.1038/nmeth932.
- Campbell, Edward M.; Hope, Thomas J. (2008): Live cell imaging of the HIV-1 life cycle. In: *Trends in microbiology* 16 (12), S. 580–587. DOI: 10.1016/j.tim.2008.09.006.
- Carlson, Lars-Anders; Briggs, John A. G.; Glass, Bärbel; Riches, James D.; Simon, Martha N.; Johnson, Marc C. et al. (2008): Three-dimensional analysis of budding sites and released virus suggests a revised model for HIV-1 morphogenesis. In: *Cell host & microbe* 4 (6), S. 592–599. DOI: 10.1016/j.chom.2008.10.013.
- Center, R. J.; Leapman, R. D.; Lebowitz, J.; Arthur, L. O.; Earl, P. L.; Moss, B. (2002): Oligomeric Structure of the Human Immunodeficiency Virus Type 1 Envelope Protein on the Virion Surface. In: *Journal of virology* 76 (15), S. 7863–7867. DOI: 10.1128/JVI.76.15.7863-7867.2002.
- Chatterjee, Amarnath; Mridula, P.; Mishra, Ram Kumar; Mittal, Rohit; Hosur, Ramakrishna V. (2005): Folding regulates autoprocessing of HIV-1 protease precursor. In: *The Journal of biological chemistry* 280 (12), S. 11369–11378. DOI: 10.1074/jbc.M412603200.
- Chertova, Elena; Bess, Jr. Julian W.; Crise, Bruce J.; Sowder II, Raymond C.; Schaden, Terra M.; Hilburn, Joanne M. et al. (2002): Envelope Glycoprotein Incorporation, Not Shedding of Surface Envelope Glycoprotein (gp120/SU), Is the Primary Determinant of SU Content of Purified Human Immunodeficiency Virus Type 1 and Simian Immunodeficiency Virus. In: *Journal of virology* 76 (11), S. 5315–5325. DOI: 10.1128/JVI.76.11.5315-5325.2002.
- Chiu, Hsu-Chen; Wang, Fu-Der; Chen, Yi-Ming Arthur; Wang, Chin-Tien (2006): Effects of human immunodeficiency virus type 1 transframe protein p6* mutations on viral protease-mediated Gag processing. In: *The Journal of general virology* 87 (Pt 7), S. 2041–2046. DOI: 10.1099/vir.0.81601-0.
- Chung, Suhman; Miller, Jennifer T.; Lapkouski, Mikalai; Tian, Lan; Yang, Wei; Le Grice, Stuart F. J. (2013): Examining the role of the HIV-1 reverse transcriptase p51 subunit in positioning and hydrolysis of RNA/DNA hybrids. In: *The Journal of biological chemistry* 288 (22), S. 16177–16184. DOI: 10.1074/jbc.M113.465641.
- Clegg, Robert M.; Holub, Oliver; Gohlke, Christopher (2003): Fluorescence lifetime-resolved imaging: measuring lifetimes in an image. In: *Methods in enzymology* 360, S. 509–542.

Coffin, John M. (Hg.) (1997): *Retroviruses*. Plainview NY: Cold Spring Harbor Laboratory Press.

Coren, Lori V.; Thomas, James A.; Chertova, Elena; Sowder, Raymond C.; Gagliardi, Tracy D.; Gorelick, Robert J.; Ott, David E. (2007): Mutational analysis of the C-terminal gag cleavage sites in human immunodeficiency virus type 1. In: *Journal of virology* 81 (18), S. 10047–10054. DOI: 10.1128/JVI.02496-06.

Correa, Ivan; Baker, Brenda; Zhang, Aihua; Sun, Luo; Provost, Christopher; Lukinavic.ius, Gra.zvydas et al. (2013): Substrates for Improved Live-Cell Fluorescence Labeling of SNAP-tag. In: *CPD* 19 (30), S. 5414–5420. DOI: 10.2174/1381612811319300011.

Côté, H. C.; Brumme, Z. L.; Harrigan, P. R. (2001): Human immunodeficiency virus type 1 protease cleavage site mutations associated with protease inhibitor cross-resistance selected by indinavir, ritonavir, and/or saquinavir. In: *Journal of virology* 75 (2), S. 589–594. DOI: 10.1128/JVI.75.2.589-594.2001.

Craven, R. C.; Bennett, R. P.; Wills, J. W. (1991): Role of the avian retroviral protease in the activation of reverse transcriptase during virion assembly. In: *Journal of virology* 65 (11), S. 6205–6217.

Dam, Elisabeth; Quercia, Romina; Glass, Bärbel; Descamps, Diane; Launay, Odile; Duval, Xavier et al. (2009): Gag mutations strongly contribute to HIV-1 resistance to protease inhibitors in highly drug-experienced patients besides compensating for fitness loss. In: *PLoS pathogens* 5 (3), e1000345. DOI: 10.1371/journal.ppat.1000345.

Dierynck, Inge; Wit, Mieke De; Gustin, Emmanuel; Keuleers, Inge; Vandersmissen, Johan; Hallenberger, Sabine; Hertogs, Kurt (2007): Binding Kinetics of Darunavir to Human Immunodeficiency Virus Type 1 Protease Explain the Potent Antiviral Activity and High Genetic Barrier. In: *Journal of virology* 81 (24), S. 13845–13851. DOI: 10.1128/JVI.01184-07.

Digman, Michelle A.; Caiolfa, Valeria R.; Zamai, Moreno; Gratton, Enrico (2008): The phasor approach to fluorescence lifetime imaging analysis. In: *Biophysical journal* 94 (2), L14-6. DOI: 10.1529/biophysj.107.120154.

Dorfman, T.; Mammano, F.; Haseltine, W. A.; Göttlinger, H. G. (1994): Role of the matrix protein in the virion association of the human immunodeficiency virus type 1 envelope glycoprotein. In: *Journal of virology* 68 (3), S. 1689–1696.

Eckhardt, Manon; Anders, Maria; Muranyi, Walter; Heilemann, Mike; Krijnse-Locker, Jacomine; Müller, Barbara (2011): A SNAP-tagged derivative of HIV-1--a versatile tool to study virus-cell interactions. In: *PloS one* 6 (7), e22007. DOI: 10.1371/journal.pone.0022007.

Erickson-Viitanen, S.; Manfredi, J.; Viitanen, P.; Tribe, D. E.; Tritch, R.; Hutchison, C. A. et al. (1989): Cleavage of HIV-1 gag polyprotein synthesized in vitro: sequential cleavage by the viral protease. In: *AIDS research and human retroviruses* 5 (6), S. 577–591. DOI: 10.1089/aid.1989.5.577.

Farnet, C. M.; Wang, B.; Lipford, J. R.; Bushman, F. D. (1996): Differential inhibition of HIV-1 preintegration complexes and purified integrase protein by small molecules. In: *Proceedings of the National Academy of Sciences* 93 (18), S. 9742–9747. DOI: 10.1073/pnas.93.18.9742.

Figueiredo, Anna; Moore, Katie L.; Mak, Johnson; Sluis-Cremer, Nicolas; Bethune, Marie-Pierre de; Tachedjian, Gilda (2006): Potent nonnucleoside reverse transcriptase inhibitors target HIV-1 Gag-Pol. In: *PLoS pathogens* 2 (11), e119. DOI: 10.1371/journal.ppat.0020119.

- Flint, S. Jane (2015): Principles of virology. 4. ed. Washington, DC: ASM Press.
- Förster, Th. (1948): Zwischenmolekulare Energiewanderung und Fluoreszenz. In: *Annalen der Physik* 437 (1-2), S. 55–75. DOI: 10.1002/andp.19484370105.
- Freed, Eric O. (2015): HIV-1 assembly, release and maturation. In: *Nature Reviews Microbiology* 13 (8), S. 484. DOI: 10.1038/nrmicro3490.
- Fun, Axel; Wensing, Annemarie M. J.; Verheyen, Jens; Nijhuis, Monique (2012): Human Immunodeficiency Virus gag and protease: partners in resistance. In: *Retrovirology* 63 (9), S. 1–14.
- Gaber, Rok; Majerle, Andreja; Jerala, Roman; Benčina, Mojca (2013): Noninvasive high-throughput single-cell analysis of HIV protease activity using ratiometric flow cytometry. In: *Sensors (Basel, Switzerland)* 13 (12), S. 16330–16346. DOI: 10.3390/s131216330.
- Ganser-Pornillos, Barbie K.; Yeager, Mark; Sundquist, Wesley I. (2008): The structural biology of HIV assembly. In: *Current opinion in structural biology* 18 (2), S. 203–217. DOI: 10.1016/j.sbi.2008.02.001.
- Gao, Min; Karin, Michael (2005): Regulating the Regulators: Control of Protein Ubiquitination and Ubiquitin-like Modifications by Extracellular Stimuli. In: *Molecular Cell* 19 (5), S. 581–593. DOI: 10.1016/j.molcel.2005.08.017.
- Garcia-Miranda, Pablo; Becker, Jordan T.; Benner, Bayleigh E.; Blume, Alexander; Sherer, Nathan M.; Butcher, Samuel E. (2016): Stability of HIV Frameshift Site RNA Correlates with Frameshift Efficiency and Decreased Virus Infectivity. In: *Journal of virology* 90 (15), S. 6906–6917. DOI: 10.1128/JVI.00149-16.
- Gautier, Arnaud; Juillerat, Alexandre; Heinis, Christian; Corrêa, Ivan Reis; Kindermann, Maik; Beaufils, Florent; Johnsson, Kai (2008): An engineered protein tag for multiprotein labeling in living cells. In: *Chemistry & biology* 15 (2), S. 128–136. DOI: 10.1016/j.chembiol.2008.01.007.
- Ghanam, Ruba H.; Samal, Alexandra B.; Fernandez, Timothy F.; Saad, Jamil S. (2012): Role of the HIV-1 Matrix Protein in Gag Intracellular Trafficking and Targeting to the Plasma Membrane for Virus Assembly. In: *Frontiers in microbiology* 3, S. 55. DOI: 10.3389/fmicb.2012.00055.
- Gheysen, D.; Jacobs, E.; Foresta, F. de; Thiriart, C.; Francotte, M.; Thines, D.; Wilde, M. de (1989): Assembly and release of HIV-1 precursor Pr55gag virus-like particles from recombinant baculovirus-infected insect cells. In: *Cell* 59 (1), S. 103–112.
- Gorelick, R. J.; Nigida, S. M.; Bess, J. W.; Arthur, L. O.; Henderson, L. E.; Rein, A. (1990): Noninfectious human immunodeficiency virus type 1 mutants deficient in genomic RNA. In: *Journal of virology* 64 (7), S. 3207–3211.
- Gottlieb, M. S.; Schroff, R.; Schanker, H. M.; Weisman, J. D.; Fan, P. T.; Wolf, R. A.; Saxon, A. (1981): Pneumocystis carinii pneumonia and mucosal candidiasis in previously healthy homosexual men: evidence of a new acquired cellular immunodeficiency. In: *The New England journal of medicine* 305 (24), S. 1425–1431. DOI: 10.1056/NEJM198112103052401.
- Göttlinger, H. G.; Dorfman, T.; Sodroski, J. G.; Haseltine, W. A. (1991): Effect of mutations affecting the p6 gag protein on human immunodeficiency virus particle release. In: *Proceedings of the National Academy of Sciences* 88 (8), S. 3195–3199.

Göttlinger, H. G.; Sodroski, J. G.; Haseltine, W. A. (1989): Role of capsid precursor processing and myristoylation in morphogenesis and infectivity of human immunodeficiency virus type 1. In: *Proceedings of the National Academy of Sciences* 86 (15), S. 5781–5785.

Göttlinger, Heinrich G. (2002): HIV-1 Gag : a Molecular Machine Driving Viral Particle Assembly and Release. Online verfügbar unter <https://pdfs.semanticscholar.org/c8a3/e393cc33fdc336c3a1f14c05464c32a24903.pdf>.

Gulnik, S. V.; Suvorov, L. I.; Liu, B.; Yu, B.; Anderson, B.; Mitsuya, H.; Erickson, J. W. (1995): Kinetic characterization and cross-resistance patterns of HIV-1 protease mutants selected under drug pressure. In: *Biochemistry* 34 (29), S. 9282–9287.

Guo, Xiaofeng; Roldan, Ariel; Hu, Jing; Wainberg, Mark A.; Liang, Chen (2005): Mutation of the SP1 sequence impairs both multimerization and membrane-binding activities of human immunodeficiency virus type 1 Gag. In: *Journal of virology* 79 (3), S. 1803–1812. DOI: 10.1128/JVI.79.3.1803-1812.2005.

Haffar, O. K.; Popov, S.; Dubrovsky, L.; Agostini, I.; Tang, H.; Pushkarsky, T. et al. (2000): Two nuclear localization signals in the HIV-1 matrix protein regulate nuclear import of the HIV-1 pre-integration complex. In: *Journal of molecular biology* 299 (2), S. 359–368. DOI: 10.1006/jmbi.2000.3768.

Hanne, Janina; Göttfert, Fabian; Schimer, Jiří; Anders-Össwein, Maria; Konvalinka, Jan; Engelhardt, Johann et al. (2016): Stimulated Emission Depletion Nanoscopy Reveals Time-Course of Human Immunodeficiency Virus Proteolytic Maturation. In: *ACS nano* 10 (9), S. 8215–8222. DOI: 10.1021/acsnano.6b03850.

Hayashi, Hironori; Takamune, Nobutoki; Nirasawa, Takashi; Aoki, Manabu; Morishita, Yoshihiko; Das, Debananda et al. (2014): Dimerization of HIV-1 protease occurs through two steps relating to the mechanism of protease dimerization inhibition by darunavir. In: *Proceedings of the National Academy of Sciences of the United States of America* 111 (33), S. 12234–12239. DOI: 10.1073/pnas.1400027111.

Hell, Stefan W.; Wichmann, Jan (1994): Breaking the diffraction resolution limit by stimulated emission: stimulated-emission-depletion fluorescence microscopy. In: *Opt. Lett.* 19 (11), S. 780. DOI: 10.1364/OL.19.000780.

Henderson, Gavin J.; Lee, Sook-Kyung; Irlbeck, David M.; Harris, Janera; Kline, Melissa; Pollom, Elizabeth et al. (2012): Interplay between single resistance-associated mutations in the HIV-1 protease and viral infectivity, protease activity, and inhibitor sensitivity. In: *Antimicrobial agents and chemotherapy* 56 (2), S. 623–633. DOI: 10.1128/AAC.05549-11.

Hermida-Matsumoto, Luz; Resh, Marilyn D. (1999): Human Immunodeficiency Virus Type 1 Protease Triggers a Myristoyl Switch That Modulates Membrane Binding of Pr55gag and p17MA. In: *Journal of virology* 73 (3), S. 1902–1908.

Hernandez, Felicia P.; Sandri-Goldin, Rozanne M. (2011): Bimolecular Fluorescence Complementation analysis to reveal protein interactions in herpes virus infected cells. In: *Methods (San Diego, Calif.)* 55 (2), S. 182–187. DOI: 10.1016/j.ymeth.2011.07.003.

Huang, Liangqun; Chen, Chaoping (2010): Autoprocessing of human immunodeficiency virus type 1 protease miniprecursor fusions in mammalian cells. In: *AIDS research and therapy* 7, S. 27. DOI: 10.1186/1742-6405-7-27.

Huang, M.; Orenstein, J. M.; Martin, M. A.; Freed, E. O. (1995): p6Gag is required for particle production from full-length human immunodeficiency virus type 1 molecular clones expressing protease. In: *Journal of virology* 69 (11), S. 6810–6818.

Humpolíčková, Jana; Weber, Jan; Starková, Jana; Mašínová, Eva; Günterová, Jana; Flaisigová, Iva et al. (2018): Inhibition of the precursor and mature forms of HIV-1 protease as a tool for drug evaluation. In: *Scientific reports* 8 (1), S. 10438. DOI: 10.1038/s41598-018-28638-w.

Ivanchenko, Sergey; Godinez, William J.; Lampe, Marko; Kräusslich, Hans-Georg; Eils, Roland; Rohr, Karl et al. (2009): Dynamics of HIV-1 assembly and release. In: *PLoS pathogens* 5 (11), e1000652. DOI: 10.1371/journal.ppat.1000652.

Jacks, T.; Power, M. D.; Masiarz, F. R.; Luciw, P. A.; Barr, P. J.; Varmus, H. E. (1988): Characterization of ribosomal frameshifting in HIV-1 gag-pol expression. In: *Nature* 331 (6153), S. 280–283. DOI: 10.1038/331280a0.

James, J. S. (1995): Saquinavir (Invirase): first protease inhibitor approved--reimbursement, information hotline numbers. In: *AIDS treatment news* (no 237), S. 1–2.

James, Michael N. G.; Sielecki, Anita R. (1985): Stereochemical analysis of peptide bond hydrolysis catalyzed by the aspartic proteinase penicillopepsin. In: *Biochemistry* 24 (14), S. 3701–3713. DOI: 10.1021/bi00335a045.

Johnson, Daniel S.; Bleck, Marina; Simon, Sanford M. (2018): Timing of ESCRT-III protein recruitment and membrane scission during HIV-1 assembly. In: *eLife Sciences* 7. DOI: 10.7554/eLife.36221.

Jouvenet, Nolwenn; Bieniasz, Paul D.; Simon, Sanford M. (2008): Imaging the biogenesis of individual HIV-1 virions in live cells. In: *Nature* 454 (7201), S. 236–240. DOI: 10.1038/nature06998.

Jouvenet, Nolwenn; Simon, Sanford M.; Bieniasz, Paul D. (2009): Imaging the interaction of HIV-1 genomes and Gag during assembly of individual viral particles. In: *Proceedings of the National Academy of Sciences of the United States of America* 106 (45), S. 19114–19119. DOI: 10.1073/pnas.0907364106.

Jouvenet, Nolwenn; Simon, Sanford M.; Bieniasz, Paul D. (2011a): Visualizing HIV-1 assembly. In: *Journal of molecular biology* 410 (4), S. 501–511. DOI: 10.1016/j.jmb.2011.04.062.

Jouvenet, Nolwenn; Zhadina, Maria; Bieniasz, Paul D.; Simon, Sanford M. (2011b): Dynamics of ESCRT protein recruitment during retroviral assembly. In: *Nature cell biology* 13 (4), S. 394–401. DOI: 10.1038/ncb2207.

Kao, S. Y.; Calman, A. F.; Luciw, P. A.; Peterlin, B. M. (1987): Anti-termination of transcription within the long terminal repeat of HIV-1 by tat gene product. In: *Nature* 330 (6147), S. 489–493. DOI: 10.1038/330489a0.

Kaplan, A. H.; Manchester, M.; Swanstrom, R. (1994): The activity of the protease of human immunodeficiency virus type 1 is initiated at the membrane of infected cells before the release of viral proteins and is required for release to occur with maximum efficiency. In: *Journal of virology* 68 (10), S. 6782–6786.

- Karn, Jonathan; Stoltzfus, C. Martin (2012): Transcriptional and posttranscriptional regulation of HIV-1 gene expression. In: *Cold Spring Harbor perspectives in medicine* 2 (2), a006916. DOI: 10.1101/cshperspect.a006916.
- Kerppola, Tom K. (2006): Design and implementation of bimolecular fluorescence complementation (BiFC) assays for the visualization of protein interactions in living cells. In: *Nature protocols* 1 (3), S. 1278–1286. DOI: 10.1038/nprot.2006.201.
- Kerppola, Tom K. (2008): Bimolecular fluorescence complementation (BiFC) analysis as a probe of protein interactions in living cells. In: *Annual review of biophysics* 37, S. 465–487. DOI: 10.1146/annurev.biophys.37.032807.125842.
- Kirchhoff, Frank (2009): Is the high virulence of HIV-1 an unfortunate coincidence of primate lentiviral evolution? In: *Nature reviews. Microbiology* 7 (6), S. 467–476. DOI: 10.1038/nrmicro2111.
- Kohl, N. E.; Emini, E. A.; Schleif, W. A.; Davis, L. J.; Heimbach, J. C.; Dixon, R. A. et al. (1988): Active human immunodeficiency virus protease is required for viral infectivity. In: *Proceedings of the National Academy of Sciences* 85 (13), S. 4686–4690.
- Könnyű, Balázs; Sadiq, S. Kashif; Turányi, Tamás; Hírmondó, Rita; Müller, Barbara; Kräusslich, Hans-Georg et al. (2013): Gag-Pol processing during HIV-1 virion maturation. A systems biology approach. In: *PLoS computational biology* 9 (6), e1003103. DOI: 10.1371/journal.pcbi.1003103.
- Konvalinka, Jan; Heuser, Anke-Mareil; Hruskova-Heidingsfeldova, Olga; Vogt, Volker M.; Sedlacek, Juraj; Strop, Petr; Krausslich, Hans-Georg (1995): Proteolytic Processing of Particle-Associated Retroviral Polyproteins by Homologous and Heterologous Viral Proteinases. In: *Eur J Biochem* 228 (1), S. 191–198. DOI: 10.1111/j.1432-1033.1995.tb20249.x.
- Konvalinka, Jan; Kräusslich, Hans-Georg; Müller, Barbara (2015): Retroviral proteases and their roles in virion maturation. In: *Virology* 479-480, S. 403–417. DOI: 10.1016/j.virol.2015.03.021.
- Kräusslich, Hans-Georg (1991): Human immunodeficiency virus proteinase dimer as component of the viral polyprotein prevents particle assembly and viral infectivity. In: *Proceedings of the National Academy of Sciences of the United States of America* 88, S. 3213–3217.
- Kräusslich, Hans-Georg; Ingraham, Richard H.; Skoog, Mark T.; Wimmer, Eckard; Pallai, Peter V.; Carter, Carol A. (1989): Activity of purified biosynthetic proteinase of human immunodeficiency virus on natural substrates and synthetic peptides. In: *Proceedings of the National Academy of Sciences of the United States of America* 86, S. 807–811.
- Kräusslich, Hans-Georg; Schneider, Henriette; Zybarth, Gabriele; Carter, Carol A.; Wimmer, Eckard (1998): Processing on In Vitro-Synthesized gag Precursor Proteins of Human Immunodeficiency Virus (HIV) Type 1 by HIV Proteinase Generated in Escherichia coli. In: *Journal of virology* 62 (11), S. 4393–4397.
- Kremers, Gert-Jan; Goedhart, Joachim; van Munster, Erik B.; Gadella, Theodorus W. J. (2006): Cyan and yellow super fluorescent proteins with improved brightness, protein folding, and FRET Förster radius. In: *Biochemistry* 45 (21), S. 6570–6580. DOI: 10.1021/bi0516273.

- La Porte, Charles J. L. (2009): Saquinavir, the pioneer antiretroviral protease inhibitor. In: *Expert opinion on drug metabolism & toxicology* 5 (10), S. 1313–1322. DOI: 10.1517/17425250903273160.
- Lam, Amy J.; St-Pierre, François; Gong, Yiyang; Marshall, Jesse D.; Cranfill, Paula J.; Baird, Michelle A. et al. (2012): Improving FRET dynamic range with bright green and red fluorescent proteins. In: *Nature methods* 9 (10), S. 1005–1012. DOI: 10.1038/nmeth.2171.
- Lampe, Marko; Briggs, John A. G.; Endress, Thomas; Glass, Bärbel; Riegelsberger, Stefan; Kräusslich, Hans-Georg et al. (2007): Double-labelled HIV-1 particles for study of virus-cell interaction. In: *Virology* 360 (1), S. 92–104. DOI: 10.1016/j.virol.2006.10.005.
- Lee, Sook-Kyung; Potempa, Marc; Swanstrom, Ronald (2012): The choreography of HIV-1 proteolytic processing and virion assembly. In: *The Journal of biological chemistry* 287 (49), S. 40867–40874. DOI: 10.1074/jbc.R112.399444.
- Loeb, Daniel D.; Swanstrom, Ronald; Everitt, Lorraine E.; Manchester, Marianne; Stamper, Susan E.; Hutchison, Clyde A. (1989): Complete Mutagenesis of the HIV-1 Protease. In: *Nature* 340, S. 397–400.
- Louis, J. M.; Clore, G. Marius; Gronenborn, Angela M. (1999): Autoprocessing of HIV-1 protease is tightly coupled to protein folding. In: *Nature structural & molecular biology* 6 (9), S. 868. DOI: 10.1038/12327.
- Louis, J. M.; McDONALD, Richard A.; NASHED, Nashaat T.; WONDRACK, Ewald M.; JERINA, Donald M.; OROSZLAN, Stephen; MORA, Peter T. (1991): Autoprocessing of the HIV-1 protease using purified wild-type and mutated fusion proteins expressed at high levels in *Escherichia coli*. In: *Eur J Biochem* 199 (2), S. 361–369. DOI: 10.1111/j.1432-1033.1991.tb16132.x.
- Louis, J. M.; Nashed, N. T.; Parris, Kevin D.; Kimmel, Alan R.; JERINA, Donald M. (1994): Kinetics and mechanism of autoprocessing of human immunodeficiency virus type 1 protease from an analog of the Gag-Pol polyprotein. In: *Proceedings of the National Academy of Sciences of the United States of America* 91, S. 7970–7974.
- Lukinavičius, Gražvydas; Mitronova, Gyuzel Y.; Schnorrenberg, Sebastian; Butkevich, Alexey N.; Barthel, Hannah; Belov, Vladimir N.; Hell, Stefan W. (2018): Fluorescent dyes and probes for super-resolution microscopy of microtubules and tracheoles in living cells and tissues. In: *Chem. Sci.* 9 (13), S. 3324–3334. DOI: 10.1039/C7SC05334G.
- Lukinavičius, Gražvydas; Reymond, Luc; D'Este, Elisa; Masharina, Anastasiya; Göttfert, Fabian; Ta, Haisen et al. (2014): Fluorogenic probes for live-cell imaging of the cytoskeleton. In: *Nature methods* 11 (7), S. 731–733. DOI: 10.1038/nmeth.2972.
- Lukinavičius, Gražvydas; Umezawa, Keitaro; Olivier, Nicolas; Honigmann, Alf; Yang, Guoying; Plass, Tilman et al. (2013): A near-infrared fluorophore for live-cell super-resolution microscopy of cellular proteins. In: *Nature chemistry* 5 (2), S. 132–139. DOI: 10.1038/nchem.1546.
- Malim, Michael H.; Emerman, Michael (2008): HIV-1 accessory proteins--ensuring viral survival in a hostile environment. In: *Cell host & microbe* 3 (6), S. 388–398. DOI: 10.1016/j.chom.2008.04.008.
- Marco, Alex de; Müller, Barbara; Glass, Bärbel; Riches, James D.; Kräusslich, Hans-Georg; Briggs, John A. G. (2010): Structural analysis of HIV-1 maturation using cryo-electron tomography. In: *PLoS pathogens* 6 (11), e1001215. DOI: 10.1371/journal.ppat.1001215.

- Martin-Serrano, Juan; Bieniasz, Paul D. (2003): A bipartite late-budding domain in human immunodeficiency virus type 1. In: *Journal of virology* 77 (22), S. 12373–12377.
- Mattei, Simone; Anders, Maria; Konvalinka, Jan; Kräusslich, Hans-Georg; Briggs, John A. G.; Müller, Barbara (2014): Induced maturation of human immunodeficiency virus. In: *Journal of virology* 88 (23), S. 13722–13731. DOI: 10.1128/JVI.02271-14.
- Mattei, Simone; Schur, Florian Km; Briggs, John Ag (2016): Retrovirus maturation-an extraordinary structural transformation. In: *Current opinion in virology* 18, S. 27–35. DOI: 10.1016/j.coviro.2016.02.008.
- Mattheyses, Alexa L.; Simon, Sanford M.; Rappoport, Joshua Z. (2010): Imaging with total internal reflection fluorescence microscopy for the cell biologist. In: *Journal of cell science* 123 (Pt 21), S. 3621–3628. DOI: 10.1242/jcs.056218.
- McDonald, David; Vodicka, Marie A.; Lucero, Ginger; Svitkina, Tatyana M.; Borisy, Gary G.; Emerman, Michael; Hope, Thomas J. (2002): Visualization of the intracellular behavior of HIV in living cells. In: *The Journal of cell biology* 159 (3), S. 441–452. DOI: 10.1083/jcb.200203150.
- Mücksch, Frauke; Laketa, Vibor; Müller, Barbara; Schultz, Carsten; Kräusslich, Hans-Georg (2017): Synchronized HIV assembly by tunable PIP2 changes reveals PIP2 requirement for stable Gag anchoring. In: *eLife Sciences* 6. DOI: 10.7554/eLife.25287.
- Müller, Barbara; Anders, Maria; Akiyama, Hisashi; Welsch, Sonja; Glass, Bärbel; Nikovics, Krisztina et al. (2009): HIV-1 Gag processing intermediates trans-dominantly interfere with HIV-1 infectivity. In: *The Journal of biological chemistry* 284 (43), S. 29692–29703. DOI: 10.1074/jbc.M109.027144.
- Müller, Barbara; Anders, Maria; Reinstein, Jochen (2014): In vitro analysis of human immunodeficiency virus particle dissociation. Gag proteolytic processing influences dissociation kinetics. In: *PloS one* 9 (6), e99504. DOI: 10.1371/journal.pone.0099504.
- Müller, Barbara; Daecke, Jessica; Fackler, Oliver T.; Dittmar, Matthias T.; Zentgraf, Hanswalter; Kräusslich, Hans-Georg (2004): Construction and characterization of a fluorescently labeled infectious human immunodeficiency virus type 1 derivative. In: *Journal of virology* 78 (19), S. 10803–10813. DOI: 10.1128/JVI.78.19.10803-10813.2004.
- Müller, Barbara; Tessmer, U.; Schubert, U.; Krausslich, H.-G. (2000): Human Immunodeficiency Virus Type 1 Vpr Protein Is Incorporated into the Virion in Significantly Smaller Amounts than Gag and Is Phosphorylated in Infected Cells. In: *Journal of virology* 74 (20), S. 9727–9731. DOI: 10.1128/JVI.74.20.9727-9731.2000.
- Nakashima, H.; Matsui, T.; Harada, S.; Kobayashi, N.; Matsuda, A.; Ueda, T.; Yamamoto, N. (1986): Inhibition of replication and cytopathic effect of human T cell lymphotropic virus type III/lymphadenopathy-associated virus by 3'-azido-3'-deoxythymidine in vitro. In: *Antimicrobial agents and chemotherapy* 30 (6), S. 933–937.
- Nijhuis, M.; Schuurman, R.; Jong, D. de; Erickson, J.; Gustchina, E.; Albert, J. et al. (1999): Increased fitness of drug resistant HIV-1 protease as a result of acquisition of compensatory mutations during suboptimal therapy. In: *AIDS (London, England)* 13 (17), S. 2349–2359.
- Oliveira, T. de; Engelbrecht, S.; van Janse Rensburg, E.; Gordon, M.; Bishop, K.; Zur Megede, J. et al. (2003): Variability at Human Immunodeficiency Virus Type 1 Subtype C Protease Cleavage Sites: an Indication of Viral Fitness? In: *Journal of virology* 77 (17), S. 9422–9430. DOI: 10.1128/JVI.77.17.9422-9430.2003.

- Ono, Akira; Ablan, Sherimay D.; Lockett, Stephen J.; Nagashima, Kunio; Freed, Eric O. (2004): Phosphatidylinositol (4,5) bisphosphate regulates HIV-1 Gag targeting to the plasma membrane. In: *Proceedings of the National Academy of Sciences* 101 (41), S. 14889–14894. DOI: 10.1073/pnas.0405596101.
- Oroszlan, S.; Luftig, R. B. (1990): Retroviral proteinases. In: *Current topics in microbiology and immunology* 157, S. 153–185.
- Pak, Alexander J.; Grime, John M. A.; Sengupta, Prabuddha; Chen, Antony K.; Durumeric, Aleksander E. P.; Srivastava, Anand et al. (2017): Immature HIV-1 lattice assembly dynamics are regulated by scaffolding from nucleic acid and the plasma membrane. In: *Proceedings of the National Academy of Sciences of the United States of America* 114 (47), E10056-E10065. DOI: 10.1073/pnas.1706600114.
- Pantaleo, G.; Fauci, A. S. (1995): New concepts in the immunopathogenesis of HIV infection. In: *Annual review of immunology* 13, S. 487–512. DOI: 10.1146/annurev.iy.13.040195.002415.
- Pantaleo, G.; Graziosi, C.; Fauci, A. S. (1993): The immunopathogenesis of human immunodeficiency virus infection. In: *The New England journal of medicine* 328 (5), S. 327–335. DOI: 10.1056/NEJM199302043280508.
- Partin, Kathryn; Kräusslich, Hans-Georg; Ehrlich, Lorna S.; Wimmer, Eckard; Carter, Carol A. (1990a): Mutational Analysis of a Native Substrate of the Human Immunodeficiency Virus Type 1 Proteinase. In: *Journal of virology* 64 (8), S. 3938–3947.
- Partin, Kathryn; Zybarth, Gabriele; Ehrlich, Lorna S.; DeCrombrugge, Marie; Wimmer, Eckard; Carter, Carol A. (1990b): Deletion of sequences upstream of the proteinase improves the proteolytic processing of human immunodeficiency virus type 1. In: *Proceedings of the National Academy of Sciences of the United States of America* 88, S. 4776–4780.
- Patock, A. K.; Potts, K. E. (1998): Protease Inhibitors as Antiviral Agents. In: *Clinical Microbiology Reviews* 11 (4), S. 614–627.
- Peng, C.; Ho, B. K.; Chang, T. W.; Chang, N. T. (1989): Role of human immunodeficiency virus type 1-specific protease in core protein maturation and viral infectivity. In: *Journal of virology* 63 (6), S. 2550–2556.
- Peterlin, B. Matija; Trono, Didier (2003): Hide, shield and strike back: how HIV-infected cells avoid immune eradication. In: *Nature reviews. Immunology* 3 (2), S. 97–107. DOI: 10.1038/nri998.
- Pettit, S. C.; Gulnik, S.; Everitt, L.; Kaplan, A. H. (2003): The Dimer Interfaces of Protease and Extra-Protease Domains Influence the Activation of Protease and the Specificity of GagPol Cleavage. In: *Journal of virology* 77 (1), S. 366–374. DOI: 10.1128/JVI.77.1.366-374.2003.
- Pettit, S. C.; Henderson, G. J.; Schiffer, C. A.; Swanstrom, R. (2002): Replacement of the P1 Amino Acid of Human Immunodeficiency Virus Type 1 Gag Processing Sites Can Inhibit or Enhance the Rate of Cleavage by the Viral Protease. In: *Journal of virology* 76 (20), S. 10226–10233. DOI: 10.1128/JVI.76.20.10226-10233.2002.
- Pettit, S. C.; Moody, M. D.; Wehbie, R. S.; Kaplan, A. H.; Nantermet, P. V.; Klein, C. A.; Swanstrom, R. (1994): The p2 domain of human immunodeficiency virus type 1 Gag regulates sequential proteolytic processing and is required to produce fully infectious virions. In: *Journal of virology* 68 (12), S. 8017–8027.

Pettit, Steve C.; Simsic, Janet; Loeb, Daniel D.; Everitt, Lorraine E.; Hutchison, Clyde A.; Swanstrom, Ronald (1991): Analysis of Retroviral Protease Cleavage Sites Reveals Two Types of Cleavage Sites and the Structural Requirements of the P1 Amino Acid*. In: *Journal of Biological Chemistry* 266 (22), S. 14539–14547.

Pettit, Steven C.; Clemente, Jose C.; Jeung, Jennifer A.; Dunn, Ben M.; Kaplan, Andrew H. (2005): Ordered processing of the human immunodeficiency virus type 1 GagPol precursor is influenced by the context of the embedded viral protease. In: *Journal of virology* 79 (16), S. 10601–10607. DOI: 10.1128/JVI.79.16.10601-10607.2005.

Phylip, L. H.; Mills, J. S.; Parten, B. F.; Dunn, B. M.; Kay, J. (1992): Intrinsic activity of precursor forms of HIV-1 proteinase. In: *FEBS letters* 314 (3), S. 449–454.

Plantier, Jean-Christophe; Leoz, Marie; Dickerson, Jonathan E.; Oliveira, Fabienne de; Cordonnier, François; Lemée, Véronique et al. (2009): A new human immunodeficiency virus derived from gorillas. In: *Nature medicine* 15 (8), S. 871–872. DOI: 10.1038/nm.2016.

Poëa-Guyon, Sandrine; Pasquier, Hélène; Mérola, Fabienne; Morel, Nicolas; Erard, Marie (2013): The enhanced cyan fluorescent protein: a sensitive pH sensor for fluorescence lifetime imaging. In: *Analytical and Bioanalytical Chemistry* 405 (12), S. 3983–3987. DOI: 10.1007/s00216-013-6860-y.

Popovic, M.; Sarngadharan, M. G.; Read, E.; Gallo, R. C. (1984): Detection, isolation, and continuous production of cytopathic retroviruses (HTLV-III) from patients with AIDS and pre-AIDS. In: *Science (New York, N.Y.)* 224 (4648), S. 497–500.

Rahman, Sheikh Abdul; Koch, Peter; Weichsel, Julian; Godinez, William J.; Schwarz, Ulrich; Rohr, Karl et al. (2014): Investigating the role of F-actin in human immunodeficiency virus assembly by live-cell microscopy. In: *Journal of virology* 88 (14), S. 7904–7914. DOI: 10.1128/JVI.00431-14.

Reymond, Luc; Lukinavičius, Gražvydas; Umezawa, Keitaro; Maurel, Damien; Brun, Matthias A.; Masharina, Anastasiya et al. (2011): Visualizing biochemical activities in living cells through chemistry. In: *Chimia* 65 (11), S. 868–871. DOI: 10.2533/chimia.2011.868.

Richards, A. D.; Phylip, L. H.; Farmerie, W. G.; Scarborough, P. E.; Alvarez, A.; Dunn, B. M. et al. (1990): Sensitive, soluble chromogenic substrates for HIV-1 proteinase. In: *The Journal of biological chemistry* 265 (14), S. 7733–7736.

Rivière, Lise; Darlix, Jean-Luc; Cimarelli, Andrea (2010): Analysis of the viral elements required in the nuclear import of HIV-1 DNA. In: *Journal of virology* 84 (2), S. 729–739. DOI: 10.1128/JVI.01952-09.

Sattentau, Q. J.; Moore, John P. (1991): Conformational changes induced in the human immunodeficiency virus envelope glycoprotein by soluble CD4 binding. In: *The Journal of Experimental Medicine* 174 (2), S. 407–415.

Schimer, Jiří; Pávová, Marcela; Anders, Maria; Pacht, Petr; Šácha, Pavel; Cígler, Petr et al. (2015): Triggering HIV polyprotein processing by light using rapid photodegradation of a tight-binding protease inhibitor. In: *Nature communications* 6, S. 6461. DOI: 10.1038/ncomms7461.

Sharp, P. M.; Bailes, E.; Robertson, D. L.; Gao, F.; Hahn, B. H. (1999): Origins and evolution of AIDS viruses. In: *The Biological bulletin* 196 (3), S. 338–342. DOI: 10.2307/1542965.

- Sharp, Paul M.; Hahn, Beatrice H. (2010): The evolution of HIV-1 and the origin of AIDS. In: *Philosophical transactions of the Royal Society of London. Series B, Biological sciences* 365 (1552), S. 2487–2494. DOI: 10.1098/rstb.2010.0031.
- Sharp, Paul M.; Hahn, Beatrice H. (2011): Origins of HIV and the AIDS pandemic. In: *Cold Spring Harbor perspectives in medicine* 1 (1), a006841. DOI: 10.1101/cshperspect.a006841.
- Sood, Chetan; Francis, Ashwanth C.; Desai, Tanay M.; Melikyan, Gregory B. (2017): An improved labeling strategy enables automated detection of single-virus fusion and assessment of HIV-1 protease activity in single virions. In: *The Journal of biological chemistry* 292 (49), S. 20196–20207. DOI: 10.1074/jbc.M117.818088.
- Suguna, K.; Padlan, E. A.; Smith, C. W.; Carlson, W. D.; Davies, D. R. (1987): Binding of a reduced peptide inhibitor to the aspartic proteinase from *Rhizopus chinensis*: implications for a mechanism of action. In: *Proceedings of the National Academy of Sciences* 84 (20), S. 7009–7013.
- Suhling, Klaus; Hirvonen, Liisa M.; Levitt, James A.; Chung, Pei-Hua; Tregidgo, Carolyn; Le Marois, Alix et al. (2015): Fluorescence lifetime imaging (FLIM): Basic concepts and some recent developments. In: *Medical Photonics* 27, S. 3–40. DOI: 10.1016/j.medpho.2014.12.001.
- Sundquist, Wesley I.; Kräusslich, Hans-Georg (2012): HIV-1 assembly, budding, and maturation. In: *Cold Spring Harbor perspectives in medicine* 2 (7), a006924. DOI: 10.1101/cshperspect.a006924.
- Swanstrom, R.; Wills, J. W. (1997): Retroviruses. Synthesis, Assembly, and Processing of Viral Proteins. Hg. v. John M. Coffin, Stephen H. Hughes und Harold E. Varmus. Cold Spring Harbor (NY).
- Tessmer, Uwe; Kräusslich, Hans-Georg (1998): Cleavage of Human Immunodeficiency Virus Type 1 Proteinase from the N-Terminally Adjacent p6* Protein Is Essential for Efficient Gag Polyprotein Processing and Viral Infectivity. In: *Journal of virology* 72 (4), S. 3459–3463.
- Tözsér, J.; Gustchina, A.; Weber, I. T.; Blaha, I.; Wondrak, E. M.; Oroszlan, S. (1991): Studies on the role of the S4 substrate binding site of HIV proteinases. In: *FEBS letters* 279 (2), S. 356–360.
- Tözsér, József (2010): Comparative studies on retroviral proteases. Substrate specificity. In: *Viruses* 2 (1), S. 147–165. DOI: 10.3390/v2010147.
- Tözsér, József; Bagossi, Péter; Weber, Irene T.; LOUIS, John M.; Copeland, Terry D.; OROSZLAN, Stephen (1997): Studies on the Symmetry and Sequence Context Dependence of the HIV-1 Proteinase Specificity. In: *Journal of Biological Chemistry* 272 (27), S. 16807–16814. DOI: 10.1074/jbc.272.27.16807.
- UNAIDS Global Report 2018. <http://www.unaids.org/en/resources/documents/2018/global-aids-update>
- Vogt, V. M. (1997): Retroviruses. Retroviral Virions and Genomes. Hg. v. John M. Coffin, Stephen H. Hughes und Harold E. Varmus. Cold Spring Harbor (NY).
- Wan, Min; Takagi, Masahiro; Loh, Boon-Nee; Xu, Xing-Zhi; Imanaka, Tadayuki (1996): Autoprocessing: an essential step for the activation of HIV-1 protease. In: *Biochemistry Journal* 316, S. 569–573.
- Wieggers, Klaus; Rutter, Gabriel; Kottler, Hubert; Tessmer, Uwe; Hohenberg, Heinz; Kräusslich, Hans-Georg (1998): Sequential Steps in Human Immunodeficiency Virus Particle Maturation

Revealed by Alterations of Individual Gag Polyprotein Cleavage Sites. In: *Journal of virology* 72 (4), S. 2846–2854.

Wlodawer, A.; Erickson, J. W. (1993): Structure-based inhibitors of HIV-1 protease. In: *Annual review of biochemistry* 62, S. 543–585. DOI: 10.1146/annurev.bi.62.070193.002551.

Wondrak, E. M.; Nashed, N. T.; Haber, M. T.; Jerina, D. M.; Louis, J. M. (1996): A transient precursor of the HIV-1 protease. Isolation, characterization, and kinetics of maturation. In: *The Journal of biological chemistry* 271 (8), S. 4477–4481.

Wu, L.; Gerard, N. P.; Wyatt, R.; Choe, H.; Parolin, C.; Ruffing, N. et al. (1996): CD4-induced interaction of primary HIV-1 gp120 glycoproteins with the chemokine receptor CCR-5. In: *Nature* 384 (6605), S. 179–183. DOI: 10.1038/384179a0.

Wyatt, R.; Sodroski, J. (1998): The HIV-1 envelope glycoproteins: fusogens, antigens, and immunogens. In: *Science (New York, N.Y.)* 280 (5371), S. 1884–1888.

Yang, Hailiu; Nkeze, Joseph; Zhao, Richard Y. (2012): Effects of HIV-1 protease on cellular functions and their potential applications in antiretroviral therapy. In: *Cell & bioscience* 2 (1), S. 32. DOI: 10.1186/2045-3701-2-32.

Zhou, W.; Parent, L. J.; Wills, J. W.; Resh, M. D. (1994): Identification of a membrane-binding domain within the amino-terminal region of human immunodeficiency virus type 1 Gag protein which interacts with acidic phospholipids. In: *Journal of virology* 68 (4), S. 2556–2569.

Zhu, Ping; Chertova, Elena; Bess, Julian; Lifson, Jeffrey D.; Arthur, Larry O.; Liu, Jun et al. (2003): Electron tomography analysis of envelope glycoprotein trimers on HIV and simian immunodeficiency virus virions. In: *Proceedings of the National Academy of Sciences* 100 (26), S. 15812–15817. DOI: 10.1073/pnas.2634931100.